
The University Of Sheffield.

# Photodynamics of Artificial Porphyrins and Metal Oxides Thin Films

Arthur Graf

University of Sheffield

Faculty of Science

Department of Chemistry

A dissertation submitted for the degree of

*Doctor of Philosophy*

June 2021

# Declaration

*The research described in this thesis is original work carried out by me at the University of Sheffield from October 2017 and May 2021. This thesis includes nothing which is the outcome of work done in collaboration except where specifically indicated in the text. The use of the first-person plural is strictly a matter of style in keeping with standard scientific convention. This dissertation has not been submitted in whole or in part for the award of a degree at this, or any other university.*

– Arthur Graf

*“There’s an important lesson here:*

*The more of a fool people take you for*

*The more you’ll learn of their true nature.”*

- NieR: Automata

# Abstract

Porphyrin is an essential compound used in nature: processes like photosynthesis and oxygen fixation on blood are assisted by porphyrins. Scientists (chemists, physicists, engineers, and others) are also exploiting porphyrins for artificial photosynthesis and energy generation, pigments and catalysts, given their success in nature. Among the most studied porphyrins is the octaethylporphyrin class (commonly used as a benchmark compound for study), containing eight ethyl radicals attached to the main ring. Those molecules are reported to have a fast internal conversion from the first excited singlet state to the second singlet and subsequentially a cascade decay passing through the triplet state and eventual return to the ground state. Artificial porphyrins sent by Prof Bruecker, University of Connecticut, could share vital information about tuning the photophysical properties of porphyrins. We studied these molecules using ultrafast time-resolved spectroscopy and mapped the energy decay within the set, finding a significant decrease in lifetime (146 microseconds for $H_2$OEP to 22 microseconds for 2,13-dioxoisobacteriochlorin) for internal conversion and intersystem crossing going from $H_2$OEP to Isobacteriochlorins. Dr Cardozo from UFRJ supported the finding with computational calculations, establishing a relationship between carbonyl deformations and spin-orbit coupling.

The world worries about disease spread are in the spotlight once again. This body of work investigates a practical and low-cost way to sterilize medical tools is thus investigated in this body of work. Metal oxides are well known and explored by their antibacterial properties by triggering a chain reaction upon light exposition. We investigated these films' photophysical and chemical properties alongside their antibacterial efficiency. The samples were provided by Dr Sami Rtimi (EPFL), who synthesised metal oxide films and double metal oxide films. We use several methods of characterisation to map electronic and structural properties. XPS results elucidate the atomic composition and bonding between the atoms in the films, quantifying the composition, whereas AFM shows the samples' surface area and thickness. In both sets of samples, it became clear that the mix of oxides (Copper-Iron and Copper-Titanium) is more effective in killing bacteria, as shown by experiments provided by Dr Rtimi. Transient absorption data show a decrease in overall lifetime when comparing the pure oxides with the mixed ones. We also show that the metal in the mixed oxides is relevant and interferes with how the decaying pathway occurs. The titanium-copper sample has different TA spectra depending on the film composition: the signal is mostly copper in the 20% Titanium and 80%

copper. When the amount of titanium increases, 60% titanium and 40% copper, the spectra show both copper and titanium features, suggesting some interplay between these atoms. Finally, a comprehensive understanding of reactive oxygen species generation and photophysical properties are achieved.

# Acknowledgements

My Oscar moment, hm? I will be as informal as I can because this is my space, right? If you don't like it, please send a formal complaint.

Firstly I cannot thank enough my supervisor: he has been a true mentor, from a science talk to life teachings and perseverance. From my first year and now my final year, I grew a lot as a person and researcher, and I have a lot to thank you for this. My colleagues at the Chauvet group throughout these years, especially Sayantan, have an uncomparable sharp mind (I still think it is impressive the amount of stuff and details you can remember at once, hahaha). I also want to thank you for your attempts at killing me with spicy food, hahaha! Alex, James and David for saving me several times at the laser lab! Julia, I could not get here without you for the constant feedback and for being so supportive. The friends Sheffield gave me and I will cherish forever. Anthony, who can produce the best laugh ever, Beth, the kindest soul I ever met. Jennifer is one of the best people I ever met: food partner, laugh friend, complaint duo. I cannot emphasise how much I will miss scaring you and hiding your stuff. Samantha, the craziest scientist ever. I have so many stories with you, and they are so precious! I had a fantastic time in the lab, and I can say it's thanks to you. I do worry about the safety of the other people in the lab after I'm gone. Who will prevent you from opening the cylinder valve and almost exploding the lab?! Martin,thank you for everything, gonna miss you! Who will I talk about, Carly Rae Jepsen, now? Good thing I can still watch your streams. Estela, Leticia and Tche, I have to say: it's becoming an annoyance now. And here you are in ANOTHER acknowledgement. But you all know you make me go forward every time and get the best of me every single time. So, see you in the next acknowledgement? (P.S. your Oscar moment is decreasing exponentially, and I have more people to thank and only a page to do it). My dear FC – Enchanted Forest- for being here all the time and giving me the breath I needed to go on. Celie for being such a good friend and my favourite maid ever <3. Leo and Yas you are FOREVER with me, and I miss you so so much. I think I cannot put in words how much you meant to me, Bolacha, please. Can I thank Kylie Minogue? HAHAHAHA Who made me dance in the lab countless times? The soundtrack of my endless nights writing reports and papers? If is not allowed, let's pretend it is not here.And of course, I had to save my family for last: my father, who is my superhero, and my inspiration; I know you have so many fans by now, by I am one of the only ones who can be proud enough to call you dad. Mum is a fantastic friend, who always makes me laugh, and always have kind words, always setting the example of perseverance and surpassing even the hardest of the challenges, yes mom, you are strong. My grandma, whom I know, is my biggest supporter ever. I would give you the world to see you smile. My two annoying brothers, who don't lose a single opportunity to bully me hahaha I am so proud of being here to see you both becoming the most amazing person ever, and I can't highlight enough how much you are special to me. My aunt Rita who is a friend, a mom, a sister altogether. If I'm a better person is because of you, you taught me values I will never forget. I cannot wait to give you a big hug. And finally to you, Jay. Partner in crime. Another step accomplished, and you're here. My eyes cannot have more sparks for you, and in fact, it

never decreased a single bit. Every single day I am reminded why you're so incredible, and it gives me the strength to move on. Love you 😊

P.S.: Special thanks to Heavenly Desserts and Johns Vans! (And the SU chicken&chips)

# Contents

# Table of Figures

## Tables

# Chapter 1: Introduction

Energy production and disease control are amongst the most challenging concerns that humanity faces. Doing it in a cheap, effective, and environmentally friendly way is not an easy task. Researchers try to replicate what nature already does well through artificial photosynthesis. The United Kingdom alone has plans to increase renewable energy deployment for the years to come and invest in research and technology[1,2]. As a direct impact of covid, the economic loss is tremendous, and we face a cut in expenses [3,4]. As such, it is imperative to develop cheaper ways of generating energy. Porphyrins are already very well established as energy harvesters by nature and scientists[5–7]. These molecules have good absorption in the visible region and can be modified to absorb specific solar spectra regions. Synthetic routes to produce different porphyrins can widely be found in the literature, and tons are already commercially available. These molecules are simulacrums of the structure located inside the chlorophyll, thus leans towards non-toxic molecules. As part of this project, the photophysics of rare and laboratory-made porphyrins is investigated.

The second half of this thesis will deal with metal-oxide thin films to understand how they can be used for medical purposes. We explore metal oxides properties and photochemical reactions for a fast and efficient sterilization method. Auto-clave is the most used method at the moment. It requires robust equipment, higher temperature, and depending on the medical tool, and it takes hours to complete the process[8,9]. The widespread of covid-19 adds extra stress to the matter, as the increased number of people in need of assistance exploded, thus the need for readily available sterilized tools. Using metal oxide films would provide a cheap, fast and environmentally friendly sterilisation method. Dr Sami Rtimi provided earth-abundant metals like copper, iron and titanium samples. He also sent mixed samples to evaluate the metals' role in producing species that could attack bacteria.

This thesis is thus divided into the following:

Chapter 2 gives the theoretical background of any principle and technique used throughout this work. It starts from the basics of frontier orbitals, developing how electronic transitions occur. Mechanisms and essential rules are discussed, and some of the maths behind it. It goes through how electron dynamics happen in solid and liquid systems and describes which factors affect

each system. the chapter then progresses with an overview of charge transfer, focusing on the expected features from the samples analysed in this thesis. Basic principles of singlet oxygen generation are also discussed in both liquid and solid means. Chapter 3 focuses on all the methodology used in the body of work, from sample preparation to the degassing procedure. The chapter also gives the theoretical background of the equipment and spectroscopical techniques. A description of how the present data were acquired and analysed is also contained within this chapter.

Chapter 4 details the research done in the porphyrins samples. It discloses the samples structures and properties. The chapter details the internal conversion and intersystem crossing in the modified porphyrins and how the photodynamics changes upon excitation. Theoretical calculations explore the macrocycle expansion through C-C and C-O stretching and the role of spin-orbit coupling. Finally, singlet oxygen data is shown and briefly discussed. A conclusion summary is written at the end of the chapter, summarising the main findings and future outlook.

Chapter 5 focuses on metal oxide films. It starts by detailing the films and their structure. Two distinguished sets of samples are discussed. This chapter is built to correlate the structural composition of the sample acquired by XPS and AFM with the photophysical dynamics of electrons and holes. Steady-state spectra will give initial information about d-d transitions within the conduction and valence bands of the films. This chapter contains details about the holes, electrons, trapped state dynamics, and how it is related to reactive oxygen species formation. The chapter also tries to establish the role of the interplay between metal atoms when different metals are present in a sample. Finally, the findings are correlated to bacterial inactivation experiments, pointing to the more efficient samples. This is all summarised in the chapter closing conclusion.

# Chapter 2: Background Theory

## Frontier orbitals

When light interacts with matter, it causes a series of phenomena in the internal electronic structure of the material. The absorption of light (a photon) provokes the transfer of electrons within the so-called frontier orbitals: the electrons are transferred from the higher occupied orbitals (HOMO) to the lowest unoccupied molecular orbitals (LUMO). The electrons do not stay in the excited state, and several outcomes can dictate where the electron goes: return to the ground state, reacting with neighbour orbitals, the formation of a new species, and so on. Organic compounds can absorb in the light spectra's ultraviolet-visible region if HOMO-LUMO is formed by antibonding p-orbitals, characteristic of the conjugated systems. The energy difference between HOMO-LUMO is the energy gap between the frontier orbitals. Any difference in energy between two orbitals or states is an energy gap.

The s orbitals are the closest to the nuclei; they experience an extra attractive force (Effective Nuclear Charge, $Z_{eff}$); thus, the electron density is also more affected. The p-orbitals are less affected by $Z_{eff}$; the bonding and antibonding molecular orbitals have smaller gaps if compared to s orbitals[10,11]

## Excited States

Before excitation, the electrons fill the lowest energy state, and upon excitation, the system behaves differently, and the electrons now populate new excited states, which are more energetic and less stable. Quantum mechanics describe electronic states using total molecular wavefunctions that consider electron spatial coordinates and nuclei interaction. Although still not a perfect model, some comfortable assumptions can be made to explain the process and classify the energy levels.

Applying Hund's rule gives information about the multiplicity of states.

The multiplicity, M, is given by equation 1.

$$M = 2S + 1 \qquad \text{(eq1)}$$

S is the sum of the spins in the electronic states. A 2-electron system can unfold in paired or unpaired electrons configuration, forming singlets and triplets.

The Born-Oppenheimer approximation states that electrons are too fast to be perceived by the nuclei (femtosecond timescale, whereas molecular vibration happens within a few nano-picosecond time windows). Thus, separating the total wave function into three different components is possible, as described by equation 2.

$$\psi_{total} = \psi_{elect.}\psi_{vib} \qquad \text{(eq.2)}$$

Electronic transitions can be studied and interpreted as a process separated from the vibrational one. Although they can be dealt with separately, the interpretation of the phenomena needs both analyses (electronic and vibrational) to be understood as part of a single rovibronic (rotational, vibronic and electronic) motion.

The energy gap between the triplet-singlet pair (closest singlet and triplet pair, in energy) depends on the nature of the electronic transition from where it arises (i.e. π- π * singlet-triplet separation is higher than n- π * pairs). This is particularly important when studying organic molecules -figure 1- as the substituents composition will significantly interfere with electron transfer dynamics[10,12].

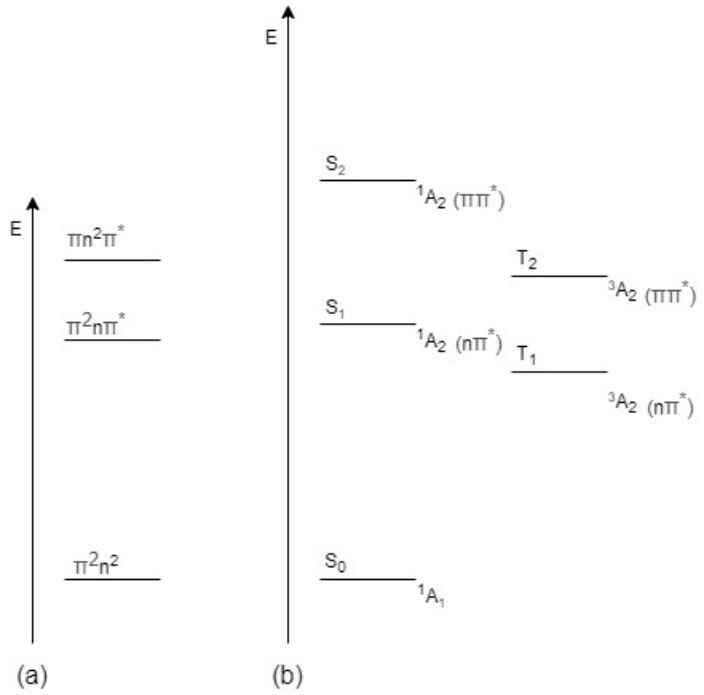


Figure 1- Singlet-Triplet splitting from π → π * and n → π *. (a) configuration, (b) states

With the wavefunctions separated, the probability of a transition occurring from the ground state $\psi_i$ to the excited state $\psi_f$ is proportional to the square of the transition moment (equation 3). It is worth noting the appearance of the dipole moment operator, μ. The dipole moment alludes to the electronic cloud dispersing alongside a molecule. Φ refers to the orbital part of the wavefunction, S to the spin and X the nuclear coordinates.

$$M_{if} = \langle \psi_i | \mu | \psi_f \rangle \qquad \text{(eq.3)}$$

When applied to the complete wavefunction derived from the Born-Oppenheimer approximation, equation 13 can be written as:

$$M_{if} = \langle \phi_i | \mu | \phi_f \rangle \langle S_i | S_f \rangle \sum_n \langle X_{i,0} | X_{f,n} \rangle \qquad \text{(eq.4)}$$

The equation shows the presence of the dipole moment operator, and it is worth noting that the operator is dependent on nuclear coordinates. Equation 4 is the basis of the following selection rules for light absorption. Several rules can be discussed from equation 4 (including Vibrational Selection rules), but only the most relevant ones will be approached for this thesis's scope.

- **Spin Selection Rule**

The term $\langle \phi_i | \mu | \phi_f \rangle$ respective to spin in equation 4 strictly depends on the multiplicity of the initial and final states of spins, and it also represents the orthogonality of wavefunctions. The term will disappear when the initial and final states have different multiplicities, becoming a spin-forbidden transition. This rule involves the mixing of states/spin-orbit coupling, which is expected to happen in multi-electron systems.

$\langle \alpha | \alpha \rangle$ = 1 and $\langle \beta | \beta \rangle$ =1

$\langle \alpha | \beta \rangle$ = 0

Where $\alpha$ and $\beta$ are spin representations for +1/2 and -1/2, respectively.

- **Orbital Selection Rule (Laporte)**

Also referred to as the Symmetry selection rule, it represents the first term at equation 4 and is susceptible to the dipole moment operator. The dipole operator can be scribed as a three-dimensional (x,y,z) and well-defined symmetry (defined point-group for the state). The term vanishes if the initial and final states are not in the same symmetry (point group). When integrating the equation, the resulting integral must be non-zero if a transition is allowed, and it is only possible when analysing the direct product of terms of irreducible representations, Γ. This rule is especially important when heavy atoms are involved or/, and molecules have an inversion centre (symbol (i)). This fact explains octahedral coordination compounds behaviour and weak d-d transitions, where the transitions are classified as symmetric (gerade, g) while the dipole operator is asymmetric (ungerade, u); hence, it is Laporte forbidden.

- **Vibrational Selection Rule**

The third and last term in equation 4 is the Frank-Condon term, discussed further in this session. In short, the term represents the integral vibrational overlap, evaluates the intensity of 0( n transitions, and serves as a basis for constructing potential energy surfaces. It is then considered that the overall square of the transition moment, M, is proportional to the oscillator strength. Experimentally, the transition moment indicates the overall vibrational

overlap expressed in the absorption spectra. The area under the curve corresponds to the oscillator strength ($f_{EG}$) from a given transition from the ground state (G) to an excited level (E) between two wavenumbers ($\bar{\upsilon}_1, \bar{\upsilon}_2$), according to equation 5.

$$f_{EG} = 4.3x10^{-9} \int_{\bar{\upsilon}_1}^{\bar{\upsilon}_2} \varepsilon\,(\bar{\upsilon}) d\bar{\upsilon} \qquad \text{(Eq.5)}$$

In the equation, $\varepsilon$ is the molar absorptivity coefficient. The definition states that oscillator strength is the unity of an electron oscillating harmonically in three dimensions. [10,13,14]. Is it required by the conservation of energy that upon excitation, the total oscillator strength should not change. Figure 2 depicts the conservation of the oscillator strength, figure (a) shows the ground state transition and the respective absorption spectra on the left-hand side, meanwhile (b) represents the hot ground state. As the value of the oscillator strength must remain the same, the missing items on the right diagram are attributed to vibrationally excited state transitions to the transitions involving vibrationally hot states.

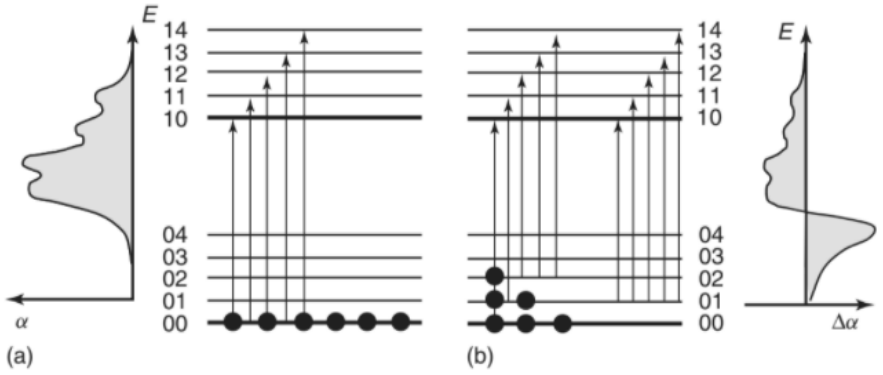


Figure 2- Energy conservation of the oscillator strength. Dots represent the molecular population. A) Ground State and absorption spectra. B) Hot ground state. (Taken from 14 – note: the author uses α and Δα for absorbance/difference in absorbance )

## Characteristics of electronic transitions

Light absorption often generates excited states in higher vibrational levels available, i.e. hot states. When applying the Born-Oppenheimer approximation to electronic transitions, as the nucleus cannot move on an ultrafast timescale, the principle of Franck-Condon is evoked. The principle states that during an electronic transition, the nucleus is static, and all electronic transitions are perpendicular (to the atomic nuclei, vertical in the energy vs nuclear coordinates graph), originating from the ground state. The ground-state has a Boltzmann equilibrium energy distribution mostly centred on the zero vibrational levels [10,12]. Excited states are not necessarily in the same nuclear position as the ground state, and the amount of how they differ is called distortion. Changing the symmetry point-group (which could be caused by structural effects, bond elongation or shrinking, etc.) is considered distortion. It implies that the emission band maximum happens in a different spectral position, generating a difference in band position for absorption and emission spectra, called Stokes-shift. Stokes-shift is thus a direct and simple measurement of the distortion between the ground and excited state. The vibrational energy of excited species is dissipated by interacting with neighbouring molecules and atoms (i.e. collisions, rearranging) through a thermalisation process called vibrational relaxation[15].

The relaxation process can either happen via radiative or non-radiative pathways (emission or not of a photon). The nomenclature of these processes is related to the multiplicity of states:

Radiative Deactivation: Is named fluorescence if emission to the ground state comes from a state of the same multiplicity (i.e. Singlet (S) → Singlet (S)). And it is phosphorescence if emission comes from a state of different multiplicity (i.e. Triplet (T) →S).

Radiationless Deactivation: It is given the name Internal Conversion when the states transitions are of the same multiplicity (i.e. S→S). Intersystem Crossing occurs when the non-radiative transition is from different multiplicity states (i.e. S→T).

Applying the selection rules makes it easy to understand that Fluorescence and Internal Conversion are allowed processes, whereas Phosphorescence and Intersystem Crossing are forbidden. This reflects on the velocity of the overall pathway and individual transitions.

Radiationless deactivation is a two-step mechanism: isoenergetic conversion of electronic of an upper state into vibrational energy of the ground state; and vibrational relaxation to the ground state. As the second is fast, the first step is the rate-determining process.

The rate, *k*, that a non-radiative transition is given by Dirac's approach to the perturbation theory, known as Fermi's Golden Rule, equation 6.

$$k = \left(\frac{2\pi}{h}\right) \langle \phi_i S_i | H' | \phi_f S_f \rangle^2 \langle X_{i,0} | X_{f,n} \rangle^2 \qquad \text{(eq.6)}$$

*H'* is a perturbation (Spin-Orbit coupling – Singlet→Triplet), and h is Planck's constant. The Franck-Codon term is a single overlap integral for each vibrational mode, thus an isoenergetic transition. Fermi's Golden Rule can be applied to all systems with weak perturbations, such as electronic and vibrational ones[15]. Non-radiative transitions are considered non-reversible as they are associated with increased entropy in the system. In the case of Internal Conversion, *H'* represents the kinetic energy operator and belongs to a totally symmetric irreducible representation (meaning that the calculated matrix of elements is symmetric); therefore, the initial and final state must be in the same irreducible representation, so the matrix element is non-zero [16].

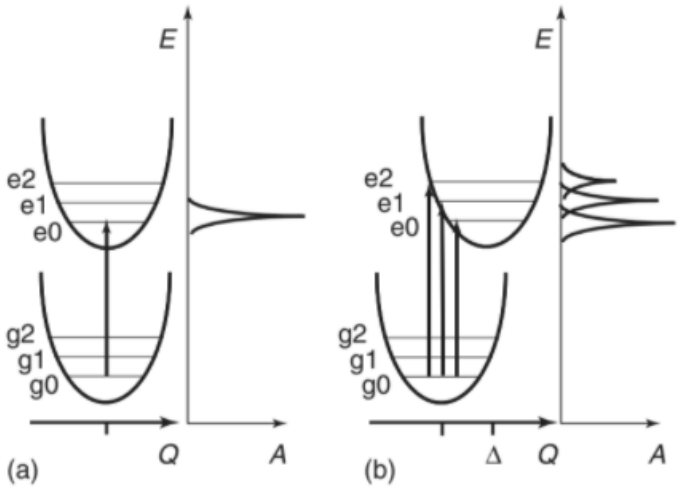


Figure 3- Representation of Franck-Condon principle (a) no displacement between Ground and Excited State, (b) Distorted excited state. (Taken from [5] )

Another important rule is the energy gap law: the probability of a transition decreases exponentially as the energy between states increases. As useful approximations, both Internal Conversion (IC) and Intersystem Crossing (ISC) rates can be roughly estimated using the energy gap law[10].

$$\log\left(\frac{k_{IC}}{s^{-1}}\right) \approx 12 - \left(\frac{2\Delta\bar{\nu}}{\mu m^{-1}}\right) \qquad \text{(eq. 7)}$$

Equation 7 exemplifies the energy gap rule applied to the internal conversion. However, the same approximation becomes more complicated regarding intersystem crossing. Many organic molecules' photoreactions involve the formation of triplet states, especially when the system is highly conjugated. ISC requires the flip of electron spin, a magnetic interaction; hence the Spin-Orbit coupling (SOC) must be considered. A triplet state's lifetime determines the overall decay rates (i.e., how many photoproducts are being generated and if there is any state quenching).

As another approximation, equation 7 can be rearranged to estimate ISC rates.

$$\log\left(\frac{k_{ISC}}{s^{-1}}\right) \approx 7 - \left(\frac{2\Delta\bar{\nu}}{\mu m^{-1}}\right) \qquad \text{(eq.8)}$$

The equation is valid for organic molecules not carrying a heavy atom. ISC dynamics can be qualitatively estimated by El Sayed's rule[8,9]. The H' operator (eq.6) for ISC is related to Spin-Orbit coupling. The spin-orbit coupling matrix element (SOCME) is determined by symmetry and the interacting molecular orbital's electronic structure. The spin flip needs to be addressed so the process respects momentum conservation; hence, the change in the spin angular moment must be accompanied by a change in orbital angular momentum. In short, the SOCME will be more significant when the transition involves an orbital with different symmetry (concerning molecular plane reflection) and changes in orbital type.

For example,

$^1$n, π* → $^3$n, π* (SLOW)

$^1$n, π* → $^3$π, π* (FAST)

## The moving electron: electron transfer and chemical kinetics

Electron transfer is only possible when two or more sites interact with each other (neighbouring atoms and molecules). It is not the scope of this thesis to develop the process' entire quantum mechanics, as it is already detailed in[11,13,17,18]. It is worthwhile mentioning that the overlap integrals and the *H'* operator need to address electric field interaction between sites, thus adopting the concept of *H'* effective. This concept implied that all electron transfers between sites must be accompanied by structural changes to accommodate the new electronic structure. This thesis will focus on two systems: first solvated organic molecules, and second, metal oxide thin films. Interpretation of data and phenomena in each system is complex and different; thus, some basic ideas are helpful and must be addressed. At first, an outlook on liquid systems, photochemical/physical properties, and later an introduction to those processes in solids.

Deactivation of excited states is often represented by the Jablonski Diagrams, where an overall pathway is drawn with their respective kinetic rates, including radiative and non-radiative processes. The kinetic model [12,16] describes competition for the preferred path for deactivation (Radiative ($k_r$), Radiationless ($k_{nr}$) and chemical reaction ($k_p$)). A given excited state *$A$ will decay with a respective lifetime $\tau_{*A}$ (eq. 9),

$$\tau_{*A} = \frac{1}{k_r + k_{nr} + k_p} = 1/(\sum_j k_j) \qquad \text{(eq. 9)}$$

Thus, the efficiency of the transition, $\eta_i(^*A)$, for each process (eq. 10):

$$\eta_i(^*A) = \frac{k_i}{\sum_j k_j} = k_i \tau(^*A) \qquad \text{(eq. 10)}$$

When equations 9 and 10 are combined, information about the Quantum Yield (Φ) is obtained—defined as the ratio between the number of molecules undergoing the process per unit of time and the number of photons absorbed per unit of time (eq 11). For a mechanism with n steps, Quantum Yield is represented by equation 12. $\eta_n$ is the efficiency of each process.

$$k_i = \Phi_i/\tau(^*A) \qquad \text{(eq. 11)}$$

$$k_i = \Phi_i(^*A)/\tau(^*A)\Pi_n\eta_n \qquad \text{(eq. 12)}$$

A) Electron transfer in solution

A few assumptions can extend from the Franck-Condom principle (i) as the electron movement is much faster than the nuclear motion, during a transition, the symmetry of states remains the same and (ii) as the transfer is very fast (few femtoseconds), the thermal energy has no time to be exchanged with the surroundings, acting as an isolated system. Implications from (i) are unavoidable, as a system cannot conserve energy if symmetry is maintained; thus, a more complex system must occur.

The multistep approach is thus suggested:

(i) Structural rearrangement leads to unstable geometry, where symmetry is the same for both exchange sites.

(ii) Electron transfer at constant geometry and energy

(iii) Relaxation of the new states to adapt to the new oxidation states.

An example of Fe-complexes is shown in figure 4. This multistep mechanism explains the solvent's role during charge transfer: a more polarised solvent will solvate and accommodate a charged species better. Experimentally, the interaction solvents will be displaced by absorption bands, called a solvatochromic shift. Solvent interaction will also affect the

deactivating pathway and either enhance or decrease the deactivation efficiency. Applying the FC Principle, the solvent has not had enough time to rearrange the new electronic configuration, and the solvation shell is now inappropriate for the system, increasing the transition energy. This effect is stronger as more polar the solvent is[16].

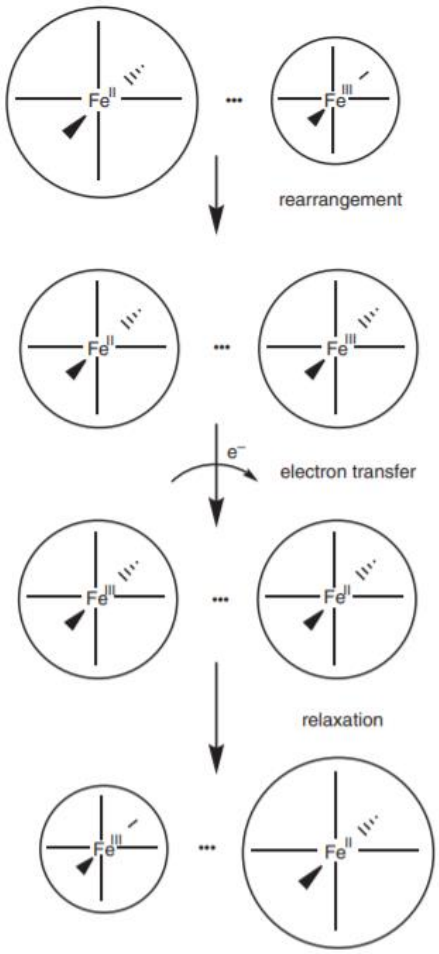


Figure 4- Multistep schematic. Adopt from [4]

The Marcus Theory's (or Marcus-Hush) interpretation of solvent/outer sphere context is extremely important to the photochemical process and relevant to what has been presented. The theory is applied for photochemical reactions with donor and acceptor sites without involving breaking bonds. Later in this thesis, the interference of the solvent and solvation processes towards the relaxation pathway of organic rings will be reviewed in the particular case of porphyrins.

The overall reorganisational energy contributes to the inner (bond lengths and angles) and outer (solvent reorganisation), with the last being the more predominant during electron transfer.

$$\Delta G^{\neq} = \frac{1}{4\lambda}(\Delta G^0 + \lambda)^2 \qquad \text{(eq. 13)}$$

Equation 13 is the basis of Marcus-Hush theory, where $\Delta G^0$ is the standard free energy change of a reaction. $\Delta G^{\neq}$ is the free energy of the transition state. Depending on the relation between the reorganisation factor and free energy, three regions can be considered: normal regime ($-\lambda < \Delta G^0$), activationless regime ($-\lambda = \Delta G^0$) and inverted regions ($-\lambda > \Delta G^0$). Fast electron transfer requires small $\lambda$ in moderate exergonic reactions (normal regions/regime, less polar solvents and large molecules). On the contrary, a slow transfer is observed in highly exergonic processes (inverted regions). The free energy should match the reorganisational energy to have a very fast electron transfer. The Marcus Inverted region is vital to understanding and improving chemical reactions with Back Electron Transfer (BET), such as photovoltaics and photosynthesis[11,13,16].

Lastly, one last mechanism should be discussed. When considering the energy transfer between the donor-acceptor pair, a charge mechanism should occur (a mechanism involving the charged species in the system). This is particularly important for studying photosynthesis (and artificial photosynthesis) and energy capture devices (i.e. solar panels).

For non-radiative processes, using a Marcus-theory approach, the transfer happens between two localised electronic excited states:

$$^*A \cdot B \rightarrow A \cdot {}^*B \qquad \text{(eq. 14)}$$

Adjusting Fermi's Golden Rule, the rate equation can be described as:

$$k_{et} = \frac{2\pi}{h}\langle \psi_{^*A \cdot B} | \widehat{H}^{en} | \psi_{A \cdot {}^*B} \rangle^2 FC^{en} \qquad \text{(eq. 15)}$$

Where $\widehat{H}^{en}$ is the electronic coupling operator and $FC^{en}$ is the Frank-Condon factor. The operator involves the frontier orbitals of the acceptor-donor pair and can be split into two terms, coulombic and exchange. The coulombic mechanism is called Forster type, while the exchange mechanism is called Dexter (Figure 5). Both mechanisms will be described subsequently.

A.1) Coulombic Mechanism

Coulombic Mechanism is also known as Förster Resonance Energy Transfer (FRET). It is a long-range interaction between sites where the Acceptor-Donor pair does not necessarily contact. Electric charges are needed for energy transfer, thus the interaction between dipoles. The transfer must obey the dipole selection rules, and no spin change is allowed. Two important equations are derived from Förster studies, equations 16 and 17. [12,19,20]

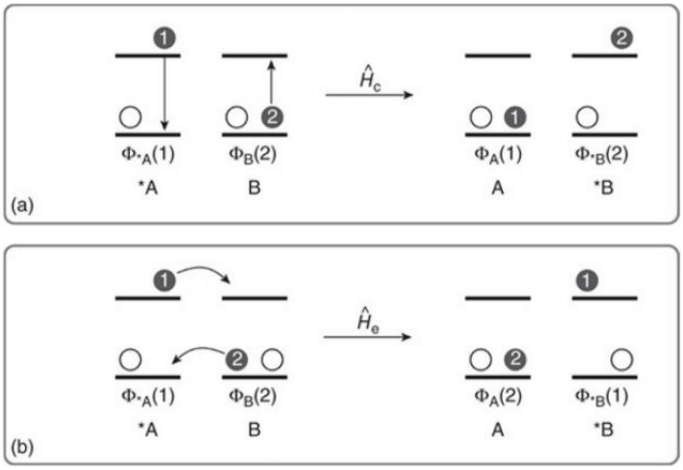


Figure 5- a) Coulombic Charge Transfer b) Exchange charge transfer. Taken from [7]

Dipole interactions depend on the distance between sites; moreover, the energy transfer rate decreases with increasing distance. Equation 16 demonstrates the relationship between the FRET rate associated with the orientation of the dipoles ($K$), the quantum yield ($\phi$) and the lifetime of the donor without the presence of the acceptor ($\tau$). The solvent (n) and distance (r) are also represented by the refractive index. $J_f$ is the overlap integral between luminescence spectra from the donor and absorption of the acceptor. Including an overlap between

experimental data turns the mechanism tied to the oscillator strength, as the more intense the oscillator strength, the faster the transfer.

$$k_{en}^{F} = 8.8x10^{-25}(\frac{K^2\phi}{n^4 r_{AB}^6 \tau})J_f \qquad \text{(eq. 16)}$$

$$k_{en}^{F} = \frac{R_0^6}{r_{AB}^6 \tau} \qquad \text{(eq. 17)}$$

Meanwhile, equation 17 is a more direct approach between the distance and FRET rate. $R_0$ represents the so-called critical distance, meaning that the energy transfer has an efficiency of 50%. The equation is valid when the intermolecular distance is larger than the size of the chromophore.

An example of a coulombic mechanism is harvesting light by the chloroplast antenna during photosynthesis; the large aromatic rings facilitate the FRET transfer from singlet-singlet states. Another common use of FRET is to track the motion of polymers/biopolymers, as the distance can be measured for different conformations of the carbon chain[13,16].

### A.2) Exchange Mechanism

In contrast to the Förster type of transfer, Dexter proposes a short-range between donor-acceptor, relying on the overlap between frontier orbitals, causing a back-transfer, as shown in figure 5b.

An advantage of this mechanism is that description can often be extended to include intervening mediums (i.e. bridge between acceptor and donor).

The rate equation for Dexter type charge transfer is, where $J_D$ is the overlap Dexter integral:

$$k_{en}^{D} = \frac{2\pi}{\hbar}\langle\psi_{*A\cdot B}|\widehat{H}^{en}|\psi_{A\cdot *B}\rangle^2 J_D \qquad \text{(eq. 18)}$$

This time the term $\widehat{H}^{en}$ depends on the overlap between donor and acceptor and can be further described as:

$$\langle \psi_{*A \cdot B} | \widehat{H}^{en} | \psi_{A \cdot *B} \rangle^2 = \widehat{H}^{en}(0) exp\left[ -\frac{\beta^{en}}{2} (r_{AB} - r_0) \right] \qquad \text{(eq.19)}$$

In this case, $\beta^{en}$ is the attenuation factor, and the whole process factor should equal the sum of the factors from the LUMO-LUMO (electron transfer) and HOMO-HOMO (hole transfer)[21]. The Exchange mechanism is essential for forming singlet oxygen and photoreactions, which shall be discussed in later chapters of this thesis.

Ceroni et al. [16] summarise well both mechanisms in the following table 1.

Table 1- Differences between Förster and Dexter mechanisms

| Coulombic Mechanism | Exchange Mechanism |
|---|---|
| Dipole-dipole long-range mechanism (in favourable conditions, efficient over 5nm) | Short-range (collisional) mechanism (less than 1nm), exponential dependence on distance as the orbital overlap is required |
| Efficient in rigid media (sphere-of-action kinetics) | Blocked in rigid media when A and B are two species dissolved in diluted solutions |
| Fast when both donor and acceptor have large oscillator strengths | Rate independent from oscillator strengths |
| In fluid solution, non-Stern-Volmer kinetics | In fluid solution, Stern-Volmer behaviour, upper diffusion-controlled limit |
| Förster formula for calculation energy-transfer rate constants from experimental data A and B | Marcus-type treatment |

B) Electron transfer in solids – Metals.

It is useful to highlight that both, the Dexter and Förster, mechanisms recently discussed also play a role when applied to solid-state dynamics. Unlike liquids, the packaging of atoms and the layering of atomic orbitals creates a situation where it is not described with discrete molecular orbitals but with intense and broad bands. The definition of bands and their subcategories will not be discussed in the present work; however, the terminology and theory will be widely used. Analogue as for molecules, the bands formed by HOMO orbitals are called Valence Band (VB), and those formed by LUMO orbitals are called Conduction Band (CB). The energy separation between the two bands is called the bandgap.

The Fermi level, or the last occupied level (where the probability of occupancy of an electron is 50%), is described with the Fermi-Dirac distribution (eq. 20). As increasing temperature causes electrons to move, the Fermi level is defined at 0K; when there is no electron motion. In the equation, f(E ) is the occupancy probability of a state, *k* is the Boltzmann constant, *T* is the temperature, *E* is the energy level and $E_f$ is the energy of the Fermi Level.

$$f(E) = 1/(1 + e^{(E-E_f)/kT}) \qquad \text{(eq.20)}$$

The Fermi level position depends on the semiconductor's nature and can change by adding dopants.

The density of states (DOS) is defined as the number of energy levels, $\delta n$, per energy $\delta E$.

$$\left(\frac{\delta n}{\delta E}\right)_E \qquad \text{(eq.21)}$$

Figure 6 shows a schematic of DOS and the Fermi level.

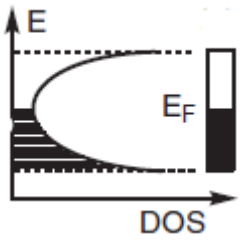


Figure 6- DOS and Fermi Level, $E_F$. Taken from [13]

When an electron (negative charge) leaves the valence band, a hole (positive charge) is formed in the electrons' place; this electron-hole pair is called an exciton. After excitation, the relaxation decay consists of the electron's return to the bulk or electron trapping in the solid defects. Figure 7 shows the electron-hole pair dynamic taken from [14]. $\bar{k}_e$ and $\bar{k}_h$ are the wavevectors, and for a filled band, the total wavevector should be equals to zero, as noted on figure 7. Selection rules also apply for these types of system, as it is stated that no change in momentum is allowed. The crystal momentum is more significant than the photon, and excess energy becomes the electron's kinetic energy (equation 21).

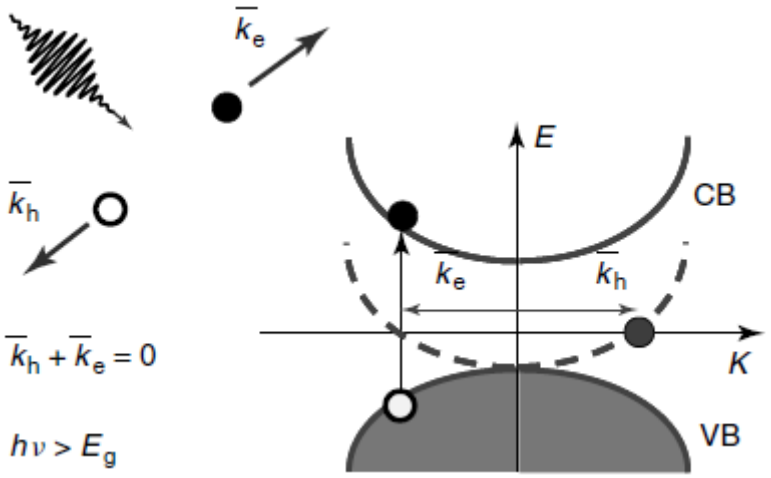


Figure 7- Electron-hole formation

In solid materials, the absorption is tied to the carrier dynamics (electron-hole pair) and the particles' mass. In equation 21, the mass of the hole is considered to be much larger than the mass of the electron ($m_e^*$). $\varepsilon$ being the excess of photon energy.

$$\varepsilon = h\upsilon - E_{gap} \approx \frac{\hbar k^2}{2m_e^*} = E_e k_e \qquad \text{(eq. 21)}$$

Similarly, the oscillator strength (equation 22) is also dependent on the mass of carriers and thus described as the oscillator sum rule for solids. The main conclusion from this rule is that DOS is a limiting parameter (limits the number of available electronic transitions), and whenever transitions occur, others should be reduced (photoinduced absorption and bleaching), affecting the population redistribution[14].

$$\Sigma_j f_{jh}(k) = 1 - \frac{m_e}{m_h^*(k)} \qquad \text{(eq. 22)}$$

$f_{jh}(k)$ is the oscillator strength from the state at *k* in filled band *h*, to state *k* in band *j*. A distinction must be made, as for flat and narrow bands, the hole's mass is large; thus, the sum rule tends to the molecular form of the expression. For parabolic bands (free electrons), the mass of hole and electron is almost equivalent, the term is close to 1, and the oscillator strength will be small.

In opposition to the molecular processes described previously, the deactivation pathway corresponds to diffusion through a solid and can be explained in terms of defects, excitons and phonons. Excess energy is dissipated in the form of heat; in fact, all electron-hole movement within a solid mean will cause some thermalisation. This all will impact how fast a charge transfer happens in a semiconductor.

The deactivation process, in this case, can be roughly reduced to four steps:

i) Carrier excitation (electron-hole generation)

ii) Thermalisation

iii) Electron-hole recombination

iv) Thermal and structural effects

In the first instance, polarised light generates the carriers almost immediately. This implies that the wavevector, *k*, is in a polarised distribution. As the momentum relaxes, this polarisation is lost, and the wavevectors redistribute. It happens as an inelastic electron-electron scattering, with no energy change and phonons. As electrons scatter and collide with the lattice, thermal energy is released until it reaches equilibrium. Electrons and holes are still separate; however, they still attract each other, and electrons are now concentrated at the bottom of the conduction band and holes on the top levels of the valence band. From this point, the outcomes could vary, either further recombination and eventual returns of electrons to the valence band or electrons being trapped in levels created by the solid defects. The thermal energy released by the whole dynamics can affect the lattice structure and assist in propagating acoustic phonons. A simplified scheme is shown in figure 8.

The metallic oxide samples explored by this research have the primary goal of producing singlet oxygen species to attack bacteria; thus, understanding the trapped states' formation is essential. Reactive Oxygen Species (ROS) readily react with an electron in the trapped states as a facilitated deactivation mechanism for metallic oxide films[22,23].

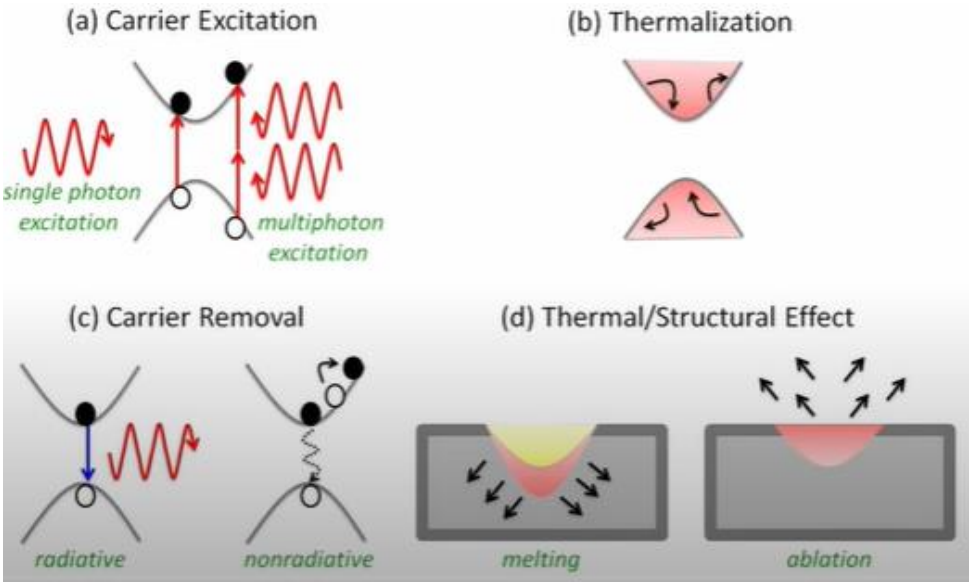


Figure 8- The deactivation dynamics on solids. Taken from [24]

Depending on the nature and size of the material, the bandgap can increase, and some upper levels can be split into other discrete levels. The wavevector is no longer a good quantum

number when such processes happen. In the case of excitons, the electron-hole pair add an extra coulombic contribution. The energy gap for these cases of exciton-exciton interaction can be described by:

$$E = E_g + \frac{\hbar^2 \pi^2}{2\mu R^2} + E_c \qquad \text{(eq. 23)}$$

Where $R$ is the crystal size, $\mu$ is the reduced mass of the electron-hole pair, $E_g$ is the energy gap, and $E_c$ is the coulombic interaction. The quantum confinement will significantly impact these materials' lifetimes and deactivation decay, and it will be further discussed later. The defects can be classified as structural defects (dislocations, atomic packaging) or point defects (impurities, orientation and chemical composition). The localised trapped levels thus form in the bandgap region of the semiconductor. Trapped carriers affect their mobility; therefore, an external stimulus is needed to liberate these charges (light exposition, vibrations, etc.). Some of the causes are transitions from coherent to incoherent transport, energy distribution and the filling of these states determining the trapping rate of the remaining free carriers. Structural defects are significantly affected by the grain boundary (interface between two unit cells of a crystalline solid) and are essential to determine what type of recombination will happen. Shockley-Read-Hall (SRH) recombination is common for non-radiative processes in solids and occurs as a two-step process: i) a forbidden energy state traps an electron or hole due to defects on the lattice (intentionally created or not), ii) if a hole or electron moves to the same energy state before re-emission of the carrier, it then recombines. The release of energy produces thermal vibrations, or phonons, which will travel along with the unit cell, resulting in heat.

Traps can be shallow or deep traps; the former is likely to recombine and the latter not. The temperature will play a vital part in the trapping/untrapping mechanism. Shallow traps are very sensitive to temperature and easily tuned by dopants[14,22,25,26].

Figure 9 (taken from [25] ) shows the necessary process behind trapping recombination.

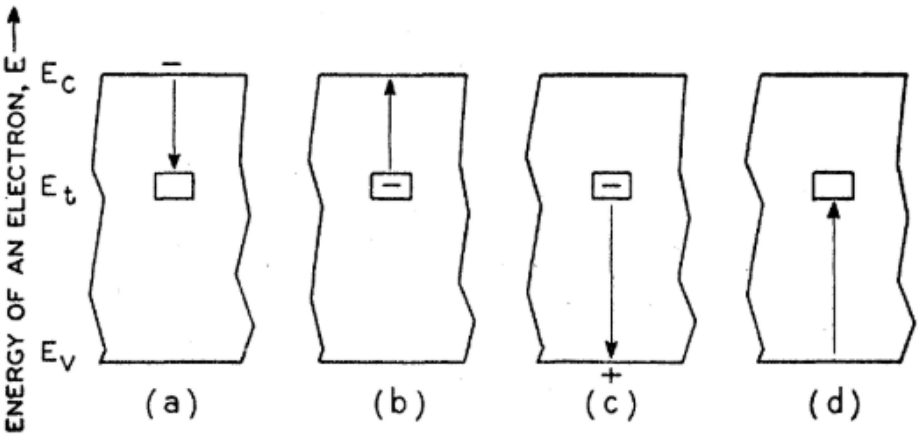


Figure 9- (a) and (c) – electron and hole capture, respectively; (b) and (d) emission of electron and hole.

## Overview of Photodynamics

This work focuses on two systems; although the spectroscopy techniques are similar, their photophysical and photochemistry properties are unique.

Porphyrin chemistry and photophysics are widely studied, particularly in unveiling the photosynthesis mechanism. These compounds are among the best candidates for solar energy harvesting (artificial photosynthesis) and non-toxic dyes due to porphyrin vibrant colours.

The second class of compounds to be approached are oxides of the first-row transition metals. Another well-known set of compounds with extensive literature available with endless possibilities of applications: energy capture devices, corrosion inhibitors, and sterilising agents—next, an overview of what is already known about these compounds is given, which also highlights the literature gap.

### A) Porphyrins

The relationship between man and the study of porphyrins is quite long now (almost 150 years), and it was Lecanu, Berzelius, Scherer and Mulder[6] the initial research on these compounds. However, it was only in 1945 with R. Willstätter and H. Fischer that the synthesis of porphyrins was possible, and the basis of this compound chemistry was introduced.[26]

Porphyrins are known for one particular characteristic: their colours. The name derives from the Greek word *porphyria*, which means purple—it originated with the Phoenicians who

extracted a purple pigment from molluscs to use in dyes for the royal family[27]. Later on, porphyrins were also related to the appearance of the porphyria disease. Porphyrin is a molecule that belongs to the tetrapyrrole compounds class, which means four carbon-based rings are attached, and the colours arise from the conjugated bond existent on these compounds. These colours can change dramatically depending on the radicals on the carbonic ring or the coordinated metal (Figure 10). Consequently, porphyrins are highly tunable.

How tetrapyrroles act inside organisms is fundamental to science: from human blood to chloroplasts, understanding these compounds' behaviour is crucial to understanding life.

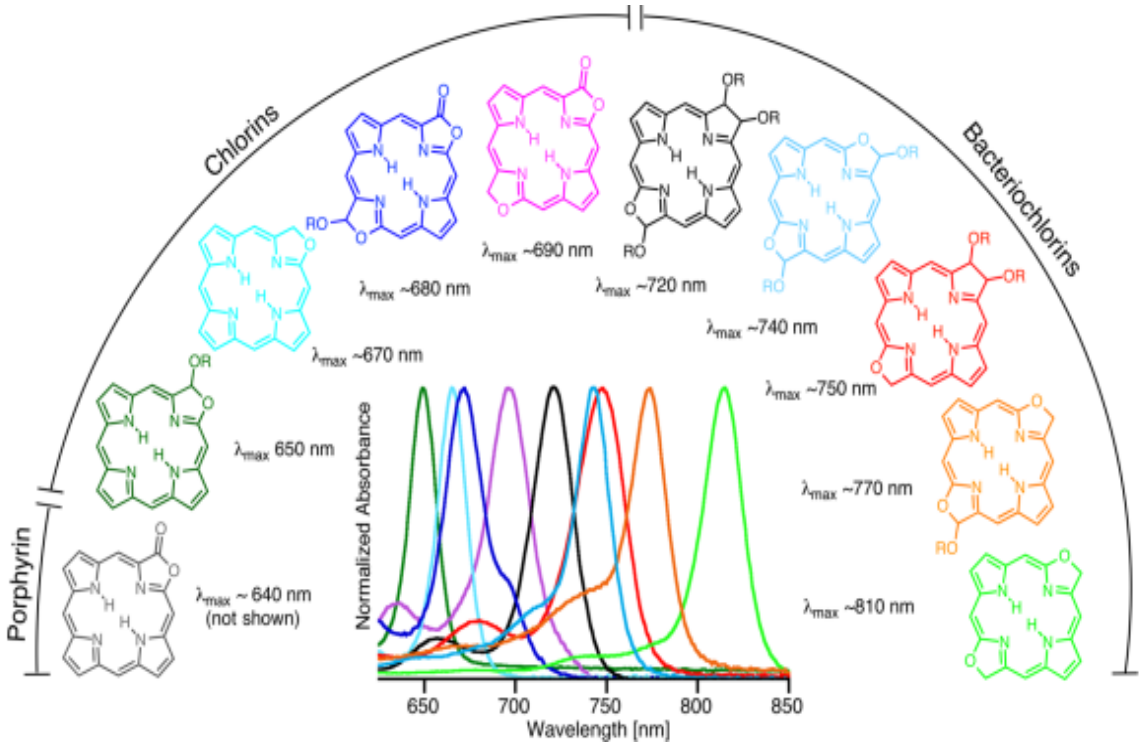


Figure 10- Structural changes and tunability of porphyrins. Taken from [28]

As previously stated, the basic structure of porphyrin is a tetrapyrrole ring, and they may have metal in the internal cavity (then metalloporphyrins) or not (free-base). Porphyrins correspond to the "main structure" (Figure 11); any radicals added are not part of the porphyrin macrocycle. In recent years, one of the most popular research fields in chemistry is the so-called artificial porphyrins, which consist of molecules that are not found in natural systems.

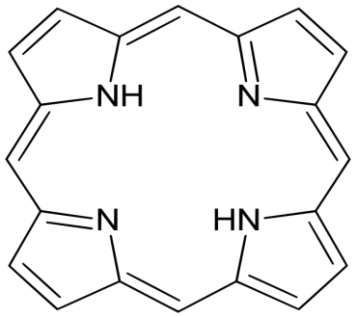


Figure 11- Porphyrin macrocycle structure

Tunability property encourages scientists to modify the molecule core (i.e. adding metals or radicals) to cause changes in absorption/emission to a specific wavelength. This same property explains why blood is reddish, and chloroplast is green; both contain a porphyrin ring.

This molecule is also interesting from a symmetry point of view, primarily because it is planar and highly symmetric ($D_{2h}$ for free-based/no metal porphyrins, and $D_{4h}$ for metalloporphyrins in most cases). The metals play an essential role in metalloporphyrins electronic structure, thus further discussed in this thesis. Electron-transfer processes are favourable in these molecules since electrons flow increases due to the planar structure and the conjugated bonds.

All the recently summarised information is essential to understanding the introductory chemistry of life: photosynthesis or how to convert sunlight into energy. The plants are masters in the field, but one question remains: can researchers improve it? What is the mechanism behind it? Where can it be applied?

Green and renewable energy are now necessary since natural resources quickly become scarce. Nevertheless, the idea of solar energy and the struggle to mimic what plants do so well. Artificial photosynthesis is the science of producing and/or analysing systems that capture the sunlight and transform it into energy using molecules with no previous report on natural systems, such as investigating radiant the conversion rate of radiant energy and its efficiency[29,30]. Chlorophyll (Figure 12) is a porphyrin molecule with a magnesium atom as a central metal and a long carbon chain as a radical on a BETA position. The porphyrins within a photosynthetic system form the antennae-reaction centre structure, where the big organic groups harvest the light energy and transfer it to the reaction centre, which conducts the chemical reactions.

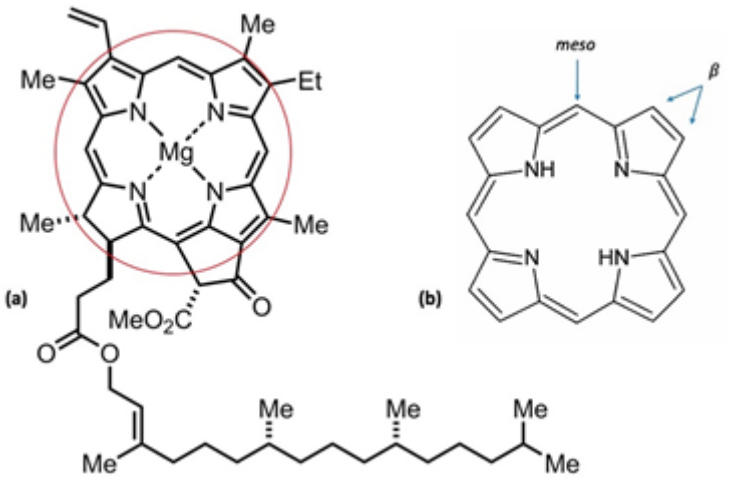


Figure 12- Figure 12- Chlorophyll structure (a), Beta positions [31]

Electronic Structure of Porphyrins

In 1961, Martin Gouterman created a model to explain the origins of porphyrin UV-Vis spectra from the highly conjugated $\pi$-electron system with the four-orbitals model[32–34]. Regular porphyrin spectra exhibit two distinct regions in the UV-Visible: one intense peak, the Soret Band, or B band, and four other minor peaks, the Q bands (Figure 13). The Q bands split into $Q_x$ and $Q_y$ regarding the axis alongside the porphyrin chemical structure. From Gouterman's work, the bands arise from the interaction of two sets of HOMO and two LUMO (two highest occupied $\pi$ orbitals and two lowest unoccupied $\pi^*$ orbitals). The Soret band is usually located between 380-500 nm and corresponds to the transition between an $S_0$ State to an $S_2$ ($S_0 \rightarrow S_2$), which is an allowed optical transition, whilst the Q bands (500 - ~750 nm) represent forbidden transitions, from $S_0$ to $S_1$ (a reason that makes this band way less intense than the Soret)[35]. The formally forbidden Q bands are attributed to the molecular vibration: the Q bands only gain intensity via vibrational borrowing from the Soret – by the Herzeber-Teller effect[31,36,37]. The Q bands result from dipole transitions that almost cancel each other and result in weak absorption, while the Soret band results from a linear combination of two transitions that reinforces transition dipoles[38]. The Soret Band is the region of significant absorption. For this reason, it is the one mainly responsible for the colours of these compounds[35], whilst the Q bands are good indicators of the chemical environment of the porphyrin (i.e. metalloporphyrins have abrupt change on Q bands, and depending on the ligand, significant changes are expected into this region).

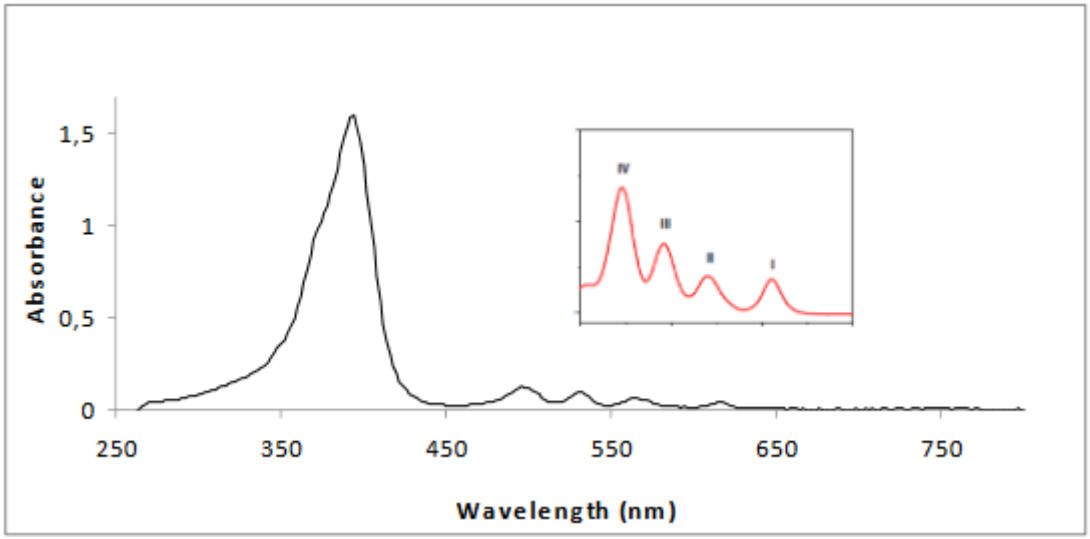


Figure 13- Main features of porphyrin spectrum. Taken from[35]

Gouterman's model considers transitions occurring from $b_1/b_2$ HOMO to $c_1/c_2$ LUMO, and it is well discussed in his original paper why both b orbitals have the same energy. Four major transitions can occur[33]; figure 14 exemplifies the schematic for the model.

The LUMO has $e_g$ symmetry based on this model, and HOMOs are $a_{2u}$, $a_{1u}$. The Soret band is the most intense transition, thus the most intense peak in the absorption spectra. At the same time, the forbidden transition is shown as a transition from the ground state to the E state of the lowest energy.

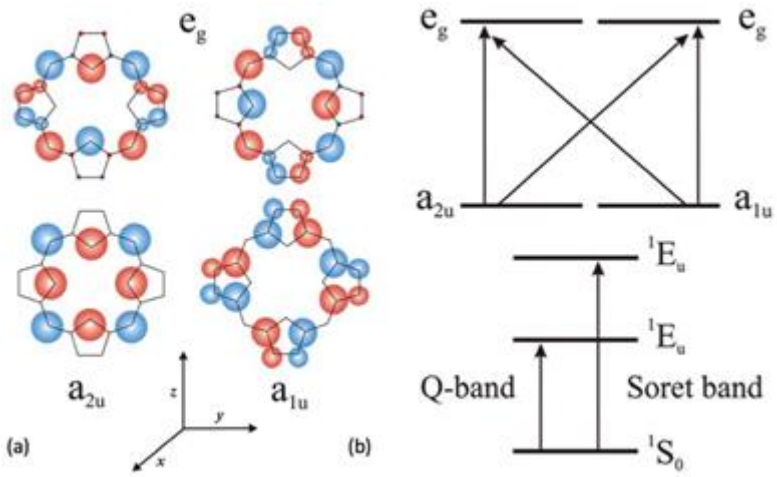


Figure 14- Gouterman model representing transitions of a Porphyrin. Taken from [31]

Spectra are classified according to the intensity of transitions and nature. Spectra subdivisions are the following:

Normal Spectra

These types of spectra are similar to the pure porphyrin: an intense Soret at 320-450 nm region and four Q bands between 450-700 nm. Metalloporphyrins are expected to have only 1 or 2 Q bands. The band changes are related to the molecule's symmetry point group ($D_{4h}$ to $D_{2h}$, from the free-base to the metalloporphyrin). Figure 13 is typical of this type. Usually, Normal Spectra are found in metalloporphyrins containing metals from groups 1 to 5, with oxidation states from I to V. Also, $d^0$ or $d^{10}$ configuration usually possesses this kind of spectra[38,39]. Figure 15 shows the diagram regarding the porphyrin orbitals for this case.

Hypso Spectra

Compared to the first group, Hypso porphyrins are blue-shifted; it is common to find these spectra in metalloporphyrins with metal configurations varying from $d^6$ to $d^9$. The mix of the orbitals explains the blue shift from the porphyrin and the metal (LUMO $e_g$ orbital from porphyrin and filled $e_g$ ($d_\pi$ from the metal), causing a charge transfer from metal to ligand, and then increasing the energy gap between transitions (LUMO orbitals are pushed to higher energy).[32,39]Antipas and Gouterman's work[32] also considered a strong spin-orbit coupling that will decrease the triplet state lifetime for this class of porphyrins.

Hyper Spectra

There are two subdivisions of Hyper Spectra, *p-type* and *d-type*. Either *p* or *d* type exhibits additional bands of moderate intensity if compared to hypso porphyrins. The difference is the origin of the additional bands, from charge transfer from the porphyrin ring to metal for *d-type* and metal to ring for *p-type*. Extra bands are $a_{2u} \rightarrow e_g$ (metal to ring) for *p-type* and $a_{1u} \rightarrow e_g$ for *d-type* (ring to metal)[32].

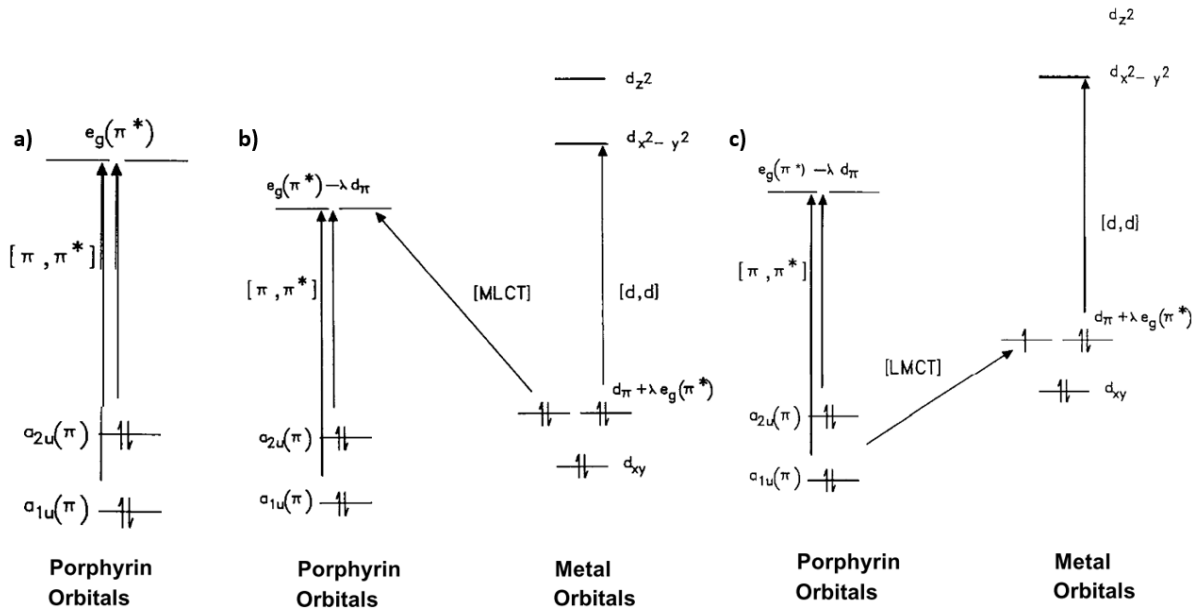


Figure 15- Molecular Orbitals. Normal (a), Hypso (b), Hyper (c) types. Taken from [38]

The Q bands feature four bands for free base porphyrins, which are classified into $Q_x$ and $Q_y$ regarding the polarization directions of the macrocycle plane. The presence of the nitrogen protons allows further splitting due to the break in symmetry, generating the X and Y components, resulting in $Q_y$ (1,0) $Q_y$ (0,0), $Q_x$ (1,0) $Q_x$ (0,0)[33,40]. The relaxation pathway is not always clear, but studies[41–43] suggest that it is most likely an excitation from Ground State to $S_2$ allowed excited state, followed by an ultrafast decay to $S_1$ (<100fs). $S_1$ is a combination of $Q_x$ and $Q_y$ and their components. It decays to triplet states from the Q bands and then returns to the ground state. It is the case for most free-based porphyrins or metalloporphyrins containing closed d-shell metals. Metalloporphyrins possesses a different pathway due to the interaction and mixing of the metal orbitals and the porphyrin ring, resulting in a retro donation system generating a d-d* state instead of $S_1$[41,42].

Upon excitation, the S2 state is populated and is followed by non-radiative processes. Singlet excited state can decay via Internal Conversion (IC) and/or Intersystem Crossing (ISC), which is induced by spin-orbit coupling[44,45].

The main structure of the decay pathway is similar to free-base porphyrins and derivatives[46–48]:

i) IC from $S_2$ to $S_1$ (Soret to Q states) within tens of femtoseconds.

ii) Upon arrival at the relevant electronic state (likely a Q bands ($Q_y$) ), rapid IC to the $Q_x$, within the same $S_1$ state.

iii) Electrons are now in a higher energy level within the $Q_x$ band (hot states), and next, they relax to the lower energy level, intramolecular vibration (IVR)[49]

iv) Finally, ISC from $S_1$ to a triplet state, ending with radiative decay back to the ground state

As previously discussed, ISC is slower than IC as it is a forbidden process (spin multiplicity selection rule). Although the overall process is similar to most porphyrinoids, some factors can interfere (enhancing or not) with the pathway. Among these is the macrocycle expansion, in which vibrational movements (in special C-C stretching and out-of-plane vibrations) make the crossing between other energetic states available [50]. The overall dynamics are linked to Spin-Orbit coupling; thus, anything that affects the SOC will also change the decay mechanism. Adding heavy atoms (such as metals and fourth-row atoms and onwards) increases SOC, making ISC rates faster. This directly applies the bandgap rule: the larger the molecule, the smaller the energy gap between the triplet-singlet and the quantum yield for phosphorescence. [11,50,51] This reflects the addition of large radicals, increasing the non-planar conformation; thus, the triplet lifetime decreases with the increasing number of β-Substituents. Adding functional groups (especially with free electron-pairs) like carbonyl, nitro and diazine promote enhanced n-π* and π-π* transition probabilities (SOC matrix element, SOCME)[10,52].

B) Metallic oxide – films

Thin film is a material layer, with nano to micro-scale in thickness, having unique properties. Tracking the historical background for thin films can be challenging since these films' uses are extensive, and the appearance of the first material to be considered a thin film is tough to determine accurately. What can be said is that at the end of the 19th century, the science behind those films developed rapidly. Table 2 (from reference [53]) summarises thin-film development advances with relevant techniques and discoveries.

Table 2- Thin films historical overview.

| Time | |
|---|---|
| End of 19th Century | unusual properties of deposits on the walls of glass discharge tubes eroded interest of researchers: optical & electrical properties (P. Drude, Ann. Der Physik, 36(1889)532) |
| 1927 | electron diffraction on thin films (David -Germer) |
| 1930 | high reflectivity surface mirrors on non- conducting substrates |
| 1940 | vacuum and thin films (PVD) techniques , devices, electron microscopy (Ruska) |
| 1960 | in situ electron microscopy (Bassett, Pashley, Poppa, Pócza, Honjo); surface decoration (Bassett, Bethge, Distler); ultrahigh vacuum technique; surface analytical methods: Auger spectroscopy, LEED, SEM, ESCA, etc. |
| 1970 | high resolution (also surface imaging) and analytical TEM ( Halle School); chemical vapour deposition (CVD); computer simulation: atom-by-atom structure building (Gilmer & Bennema, Barna, Thomas et al; Dirks & Leamy) |
| 1980 | atomic resolution surface imaging techniques: STM, AFM (Binning & Röhrer); atomic layer epitaxy; electron energy loss analysis - dedicated scanning TEM |
| 1990 | aberration corrected ultrahigh resolution analytical TEM (Urban) |
| 2000 | advent of in situ techniques (UHV TEM, fast STM, synchrotron) |

Immense use of films has been reported [53–58]: in engineering, medicine, energy harvesting and generation, and many others. One of the most promising areas is the production of high efficiency and fast sterilization, in other words, killing bacteria[23,57]. The long chain reaction drives the process when the films are under ultraviolet light.

From a medical point of view, sterilization is one of the most significant concerns: the risk of propagating foreign bodies and pathogens is still considerable, and the number of patients using surgical procedures is continually rising[59]; thus is essential for the development of a better coating for surgical tools and methods of fast and good sterilization. Studies show that some films such as $TiO_x$ and Ag have antibacterial performance rates of 99.99% against *Escherichia coli* in visible light. Some metal oxides are semiconductors, which can act as photocatalysts for organic molecules and kill bacteria[56,60].

The four steps of the decay mechanism previously mentioned have their timescale closely related to the bandgaps value and the bands of the solid's different atoms. However, the carriers' recombination rate is the determining factor which causes most of the energy loss and dictates its overall lifetime. In photocatalytic reactions (such as ROS production), the carrier recombination must be slower than the reaction timescale [24,61].

Figure 16 shows a few examples of bandgap energies for different metal oxides, taken from [62].

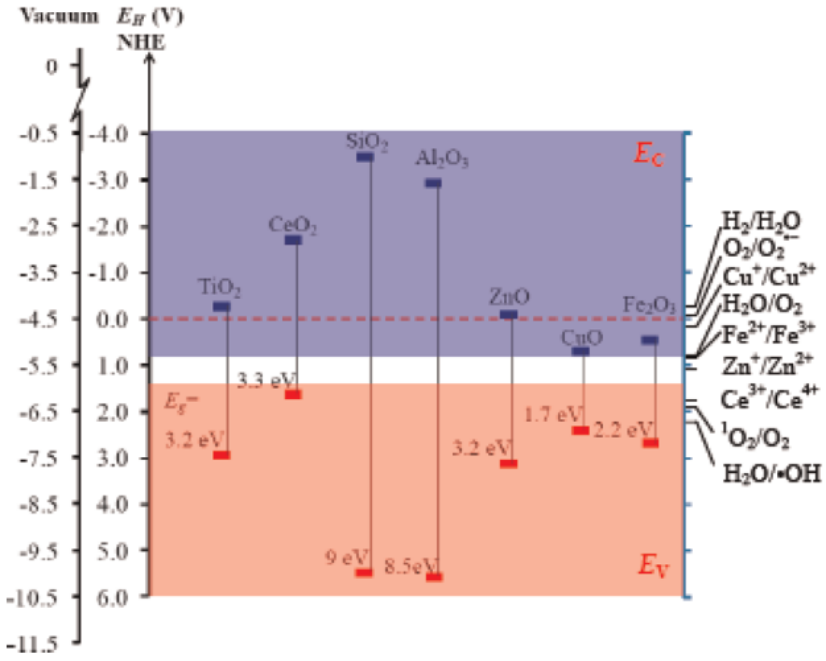


Figure 16- Band energies for metal oxides

ROS formation and Deactivation mechanism

Upon excitation above the bandgap value, a decay cascade starts within the solid, triggering a redox reaction. Carriers form within a femtosecond timescale and recombine, releasing energy; charges can then reach forbidden states and be trapped within those. Those trapped charges will then react with adsorbates and initiate the redox reaction.

For example, the cascade reaction of $TiO_2$ will be presented and can be easily adjusted for other metal oxides[63].

$$TiO_2 + h\upsilon \rightarrow TiO_2(h^+_{VB}) + TiO_2(e^-_{CB}) \qquad \text{(eq. 24)}$$

Equation 24 describes the generation of electrons and holes within the fs timescale. Oscillatory formation and charge annihilation happen within the first few tens of femtoseconds and only after relaxation [24].

$$e^-_{CB} + Ti^{IV} \rightarrow Ti^{III}(\text{deep trapping}) \quad \text{(eq. 25)}$$

$$h^+_{VB} + Ti^{IV}OH \rightarrow \{Ti^{IV}OH^{\bullet}\}^+ \text{ (hole trapping)} \quad \text{(eq. 26)}$$

Immediately after excitation, the system does not follow a Fermi-Dirac distribution and takes up to a few hundred femtoseconds to stabilize. The trapping of electron and hole is displayed in equations 25 and 26, respectively. The carrier-phonon scattering is another event within the same timescale up to a few picoseconds. The energy from this type of transfer energy to the lattice until it reaches thermal equilibrium[24]. Equations 27 and 28 represent the carrier recombination. This step can take hundreds of picoseconds to a few nanoseconds and can occur radiatively (photon emission) or non-radiative through the Auger process (ejection of a second slower electron) or defect recombination.

$$h^-_{VB} + Ti^{III} \rightarrow Ti^{IV} \quad \text{(eq. 27)}$$

$$e^-_{CB} + (Ti^{IV}OH^{\bullet}) \rightarrow Ti^{IV}OH \quad \text{(eq. 28)}$$

Finally, the last two equations, 29 and 30, show the trapped carriers (eq. 25 and 26) combining with other chemical species to produce ROS. The forbidden nature of this transition makes this step slower than the previous ones, and it also competes with thermal and structural effects, happening within several picoseconds up to hundreds of microseconds.

$$Ti^{III} + O_2 \rightarrow Ti^{IV} + O_2^{\bullet -} \quad \text{(eq. 29)}$$

$$\{Ti^{IV}OH^{\bullet}\}^+ + H_2O \rightarrow Ti^{IV}OH + {}^{\bullet}OH + H^+ \quad \text{(eq. 30)}$$

As elucidated in the equations above, the charge transfer process must occur from the metal atom to the adsorbates (oxygen and water); thus, the metal's band edge must be in an appropriate energy level (above) electrochemical potential scale of the adsorbates. ROS can be one of four chemical species: superoxide radical, hydrogen peroxide, singlet oxygen and hydroxyl radical[64]. Figure 17 shows a simplified schematic of different ROS production and their respective electrochemical potential.

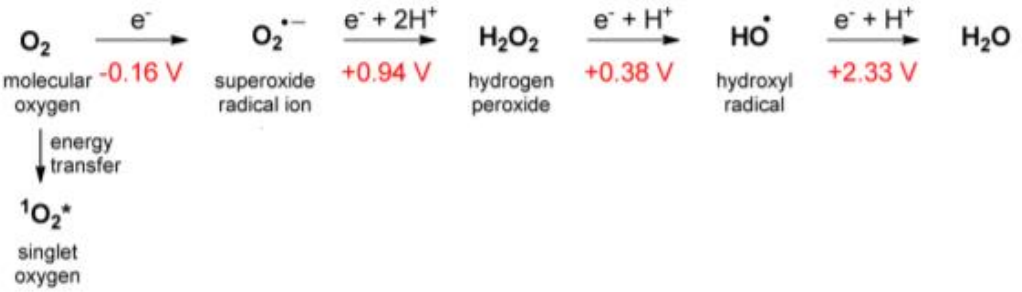


Figure 17- ROS formation through electron transfer. Adapted from [64]

Molecular oxygen has a ground-state triplet, paramagnetic, occupying π* orbitals, reacting fast with other free radicals via electron transfer. One electron reduction of oxygen results in the superoxide anion, and the reduction of superoxide forms peroxide. Further reduction and the hydroxyl appear, and it decomposes into water. Singlet Oxygen is one of the main factors for the antibacterial properties; thus, it will be further explored. The next chapter will introduce the instrumentation and describe the methodology adopted for the experimental part of the project.

# Chapter 3: Methods

## Materials

Porphyrin samples were synthesised and sent by professor Christian Bruckner; the synthesis route can be found elsewhere[28,65,66]. Solvents (HPLC grade) and singlet oxygen references were bought from commercial sources (WVR, Sigma Aldrich, Fisher Scientific, etc.) or the University of Sheffield – Chemistry stores and used as received.

Metal oxide films were prepared and sent by Dr Sami Rtimi, and detailed preparation methods are discussed in other sources[23,57,67].

## Sample preparation

### Porphyrin samples

A set of artificial porphyrins were received from Prof. Bruckner; those are structural modifications of the Octaethylporphyrin with additional carbonyl groups. Figure 18 shows all the structures received and analysed in this work.

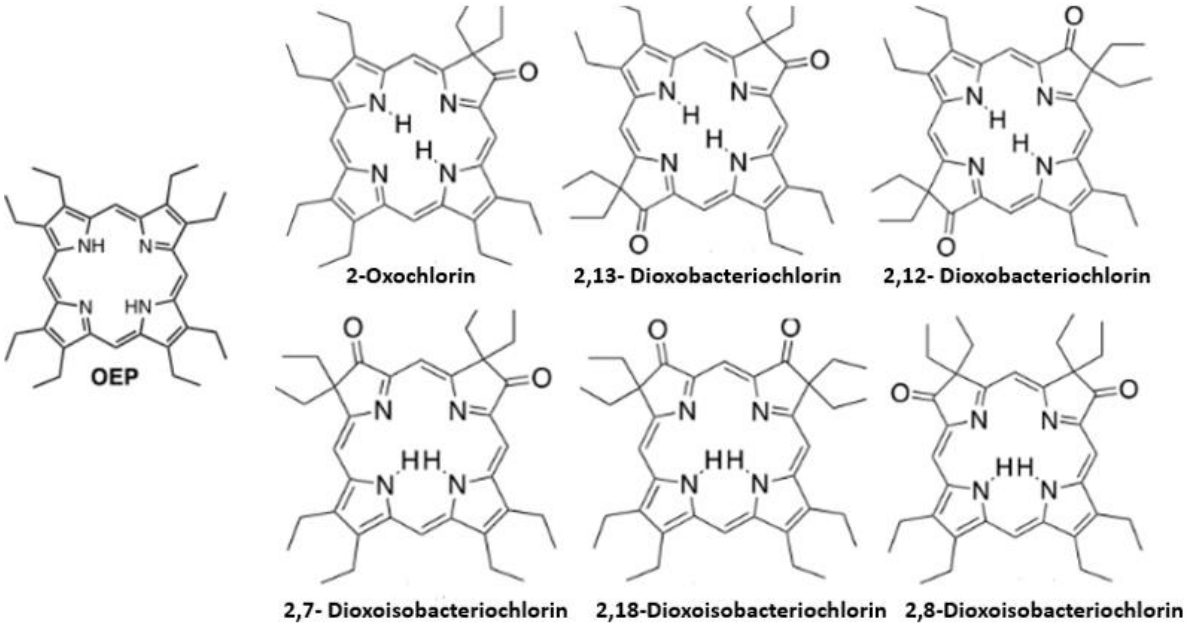


Figure 18- Artificial porphyrin set

The sample solutions were made with dichloromethane, and to avoid degradation, oxygen was removed using the pump-freeze-thaw degassing method. This method uses a Schlenk line to

remove the oxygen from the sample by freezing the solution (in a solvent that freezes in liquid nitrogen) and sucking out oxygen with a vacuum pump. The procedure is repeated a few times until the oxygen is not more present, and then the flask is filled with an inert gas (Argon).
Singlet Oxygen measurements were done in a solution of acetonitrile and using Perinaphthenone as a reference; detailed procedures and results are in later chapters.

### Metal Oxide Films

Dr Ritmi prepared the samples using a combination of Chemical Vapour Deposition and Plasma treatment.
Two samples were received: An Iron/Copper-based film and another Titanium/Copper film. The first set contains the following samples: $Fe_xO_y$; $Cu_kO_l$ *and* $Fe_xO_y - Cu_kO_l$.
The second group is: $TiO_2, Cu_kO_l, TiO_2 - Cu_kO_l$ $(80\%, 20\%), TiO_2 - Cu_kO_l$ $(60\%, 40\%)$.
Later in this thesis, the metal and Oxygen proportion will be defined via X-ray Photoelectron Spectroscopy (XPS).

## Characterisation

### Steady State Absorbance

Absorption spectra were measured using Agilent Technologies Cary 60 Spectrometer.
The spectra were recorded at room temperature and corrected against pure solvent or
blank substrate.
Beer-Lambert law quantifies the concentration of the specimens from the steady-state absorption spectra. The relationship is given by the absorption and transmittance of the sample, equation 31:

$$A = -log_{10}T = log_{10}\left(\frac{I_0}{I}\right) \qquad \text{(eq. 31)}$$

where $T$ stands for transmittance, $A$ for absorption, $I_0$ and $I$ is the light intensity before and after interacting with the medium.
Experimental transmittance is exponentially dependent on the path length – the distance that the light travels – and the analyte's concentration. With the introduction of a new parameter, $\varepsilon$ – molar absorptivity coefficient- equation 32 the is known as the Beer-Lambert law:

$$A = log_{10}\left(\frac{I_0}{I}\right) = \varepsilon lc \qquad \text{(eq. 32)}$$

Emission spectra were obtained with 365 nm excitation wavelength from a 450 W Xe1 xenon arc lamp.

### X-Ray Photoelectron Spectroscopy (XPS)

This technique has its roots in the photoelectric effect, and it is a powerful tool to map the electronic structure of the atoms and structural organisation and a quantification method. Photoelectrons are ejected as a photon interacts with matter, depending on the energy deposited. X-ray energy range allows the ejection of inner core electrons, and the analysis of those gives valuable information about binding energy, oxidation states and quantity. Equation 33 correlates the energy source(h as Plank's constant, and $\nu$ the frequency), Kinetic Energy (*KE*), binding energy (*BE*) and work function ($\Phi$).

$$h\nu = \Phi + KE + BE \qquad \text{(eq. 33)}$$

The difference between Fermi`s and the vacuum levels is equivalent to the work function. The work function is the minimum amount of energy required to release an electron from an atom, and it is the same as ionisation energy when a conduction band is full. Energies with a lower value than the work function will not be sufficient to remove the electrons[58,68].

XPS consists of using soft X-rays to excite the sample. Due to X-rays high energy, electrons from the atom's core are ejected instead of valence electrons. Figure 19 shows a schematic of the process. The instrumentation measure the kinetic energy of the electrons ejected by the sample, using an electric field to deflect selected electrons.

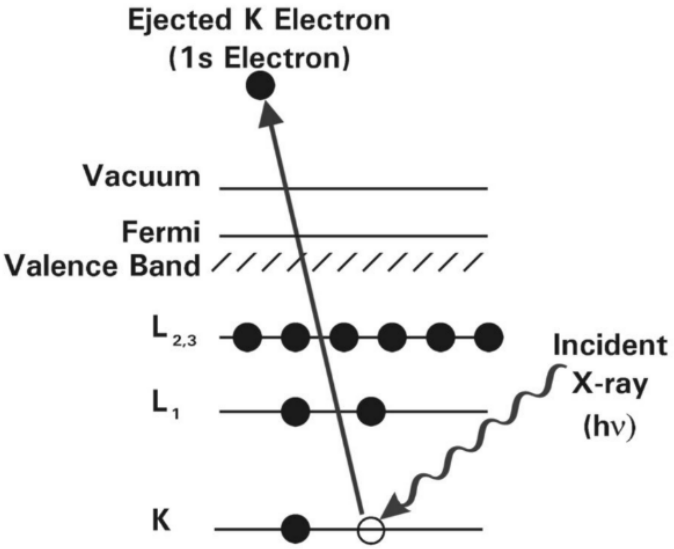


Figure 19- Photoelectron ejection from inner levels. Taken from [69]

The experimental analyses were carried out on the surface chemistry lab facility at the University of Sheffield, and the operator provided all the following information. A Kratos Supra instrument was used, with a monochromatic aluminium source and two analysis points per sample.

The area of analysis was 700 by 300 µm. Survey scans were collected between 1200 to 0 eV binding energy at 160 eV pass energy, 1 eV intervals, and one 300 second sweep across the energy range. High-resolution O 1s, N 1s and C 1s XPS spectra were also collected at 20 eV pass energy and 0.1 eV intervals for each analysis point over an appropriate energy range, with one 300 second sweep for carbon and oxygen and two sweeps for nitrogen. For UPS: As these samples were all insulators, it was expected that charge neutralisation would have to be used. However, the photoelectrons would dominate the He(I) spectrum due to the charge neutralisation. Consequently, it was first confirmed that a negligible signal was obtained in a He(I) spectrum if charge neutralisation was not used. Instead, He(II) was used with charge neutralisation. Spectra were collected between 33 to 0 eV at 0.05 eV intervals, 300 seconds / sweep and 6 sweeps collected. The pass energy used was 10 eV, and the 110 µm collimation aperture was used.

## Time-resolved measurements

### Time-correlated Single Photon Counting (TCSPC) and Time-Resolved Emission Spectroscopy (TRES)

Time-resolved fluorescence data were collected on an Edinburgh instrument FS5 spectro-fluorimeter. In TCSPS measurements, samples were kept in a 1-cm transparent quartz cuvette, and a NanoLED of 365 nm was used as an excitation source, with an instrument response function width of 1 ns.

### Transient Absorption Spectroscopy – Introduction and Instrumentation

Energy transfer in photochemical systems is one of the fastest molecular events known. The photosynthesis process begins with harvesting the light by a complex antenna-reaction centre system. A long-chain reaction is triggered by it, and it involves multiple electron transfers to different photosynthetic complexes within the chloroplast[70].

This system already loses energy due to internal conversion, fluorescence and intersystem crossing. The charge transfer must happen at atto to femtoseconds to compensate for this loss. Only techniques with femtosecond timescale resolution can achieve the results to track excited stated dynamics.

With pulsed laser systems, time-resolved spectroscopy is the best suitable tool to track short-lived species (i.e. excited states, solid band dynamics, and others). The ultrafast Transient Absorption (UTAS) technique originated with the flash photolysis created by George Porter (Lord Porter), awarded the Nobel Prize in 1967 for his achievement. The idea consists of using an intense light pulse with a suitably short time duration to perturb the equilibrium of a system and follow the evolution of transient electronic states. As the name suggests, the technique is based on absorption, which follows the Beer-Lambert equation, which can be suitably adapted for time-resolved purposes. Equation 34 refers to the system after the pulse, and equation 35 is right before [12].

$$I(\lambda, t) = I_{incident}(\lambda) x 10^{-A(\lambda,t)} \quad \text{(eq. 34)}$$

$$I_0(\lambda) = I_{incident}(\lambda) x 10^{-A_0(\lambda)} \quad \text{(eq. 35)}$$

Where $I$ is the beam's intensity, A is the sample's absorption after the analysis beam, whereas $A_0$ refers to the absorption from the excitation beam. Rearranging the equation leads to eq. 36:

$$\Delta A(\lambda, t) = -\log\left[1 + \frac{\Delta I(\lambda,t)}{I_0(\lambda)}\right] \quad \text{(eq. 36)}$$

Following the Lambert-Beer equation, where c is the concentration of the transient, $l$ is the cuvette path length and $\varepsilon(\lambda)$ the coefficient of molar absorption of the transient state; the final equation, 37, can be summarised as:

$$\Delta A(\lambda, t) = \left(\varepsilon(\lambda) - \varepsilon_{S_0}(\lambda)\right) lc \quad \text{(eq. 37)}$$

where $\varepsilon_{S_0}$ is the absorption coefficient of the ground state. UTAS is a technique that allows exploring chemistry with a time resolution in the order of $10^{-14}$ to $10^{-15}$s. The pump-probe spectroscopy scheme is applied here: a pump pulse is emitted and excites the molecules to a higher energy level, exciting only a small fraction of molecules. A probe pulse is then sent and is used to take a snapshot of the sample. From the latter, the difference absorption spectrum is calculated. The probe is delayed, using mirrors on the experimental setup to acquire the temporal dependence. UTAS is useful for obtaining a temporal profile and kinetics of fluorescent and non-fluorescent transient species and gives relevant information regarding the relaxation pathway and electronic transitions[42,70]. The signal acquired from this technique contains several processes, and the most important of them are the following:

a) Ground-State bleach: The Ground State's absorption is expected to be negative since it is a depopulated state. The excited state is more populated than the ground state, implying that its absorption will be lower. The resulting signal thus will be negative in the TA spectra.
b) Stimulated Emission: As the name suggests, if an electron in an excited state is perturbed by additional energy, it can be stimulated to return to the ground state. In this case, it is lowering the population of this excited state. The absorption of this state decreases, and it will show as a negative signal on the spectra.
c) Excited-State Absorption: Since the technique measures the absorption of excited states, it is expected to result in a positive signal.

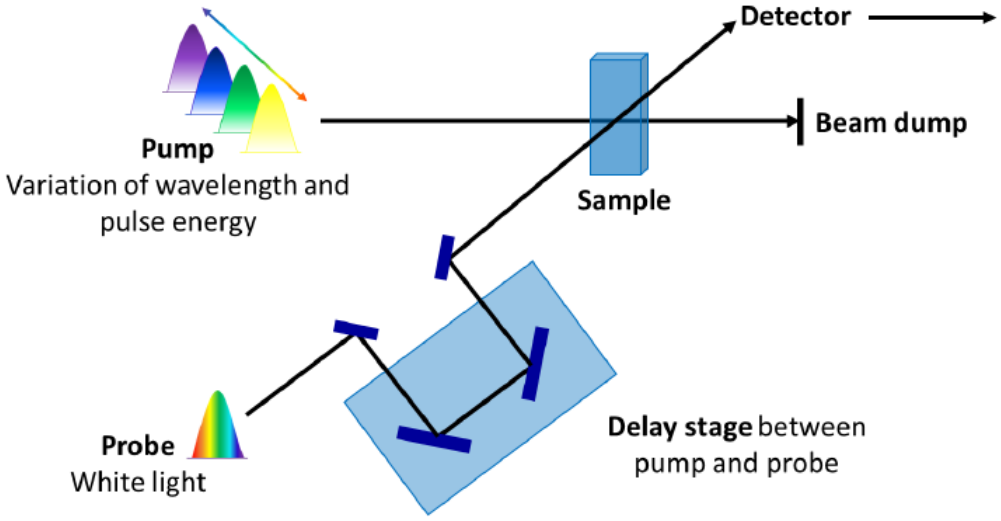


Figure 20- Pump-probe scheme Adopted from [63]

Analogue to liquid systems described, for solid-state, the dynamics are summarised in figure 21. Positive signals are ascribed as either hole or electron absorption, whereas the negative features are Stimulated Emission and Ground State bleach[57]. Electron Absorption (EA)/Hole Absorption (HA) is the main positive signal, whereas GSB and SE are the negative features in the spectra.

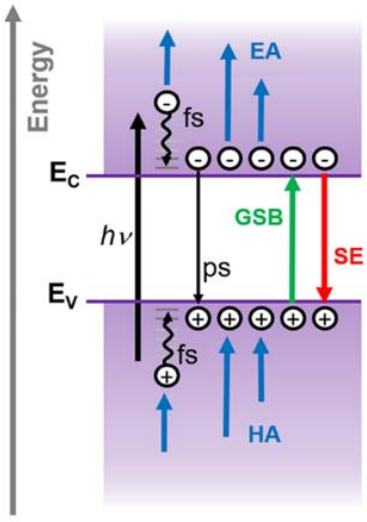


Figure 21- TA features on solids. Taken from [49]

The kinetic profile and lifetimes can be obtained via equations 38[12,24,42,45,49]. Multiple exponential models are used, as most of the data collected contain multiple time constants within the analysed range.

$$\Delta A(\lambda, t) = I_1(\lambda)e^{-k_1 t} + I_2(\lambda)e^{-k_2 t} + I_3(\lambda)e^{-k_3 t} \ldots \quad \text{(eq. 38)}$$

Where *k* is given by:

$$k = \frac{1}{\tau}\ (s^{-1}) \quad \text{(eq. 39)}$$

The laser system for this type of spectroscopy needs to produce a pump pulse of the same energy of the electronic transition of concern to promote electrons to the excited state. A probe pulse comes shortly after, delayed by a moving delay stage. The probe is typically a white light continuum generated through a $CaF_2$ crystal. The relative intensities between probes with and without pump pulse are used to calculate the difference absorption spectra[12,71]. Solid-state laser amplifiers such as Ti: Sapphire can extract high energies from modest-scale laser systems due to the high saturation fluorescence. To do so, a technique called Chirped Pulse Amplification is used[70].

The regenerative amplifier principle involves trapping the laser beam by changing the polarization in a cavity where the light goes back and forth: each passing through the Ti: Sapphire crystal increases the pulse intensity. The pulse is trapped until it reaches the limit of the cavity saturation, then the polarization is changed, and the pulse is released[16,70].

Transient absorption spectroscopy (TA) was performed at the Lord Porter Laser Laboratory, University of Sheffield. A Ti: Sapphire regenerative amplifier (Spitfire ACE PA-40, SpectraPhysics) producing 800 nm pulses (40 fs FWHM, 10 kHz,1.2 mJ) is used as the primary laser source. Pump excitation is kept at 400 nm and generated using the second harmonic generation of the 800 nm output in a β-BBO crystal within a commercially available higher harmonic generator (TimePlate, Photop Technologies). The amplifier output generates white light super-continuum probe pulses by focusing an 800 nm beam on a $CaF_2$ crystal (340–790 nm). Detection was achieved using a commercial transient absorption spectrometer (Helios, Ultrafast Systems) using a CMOS sensor for the UV-vis spectral range. The pump and probe pulses' relative polarisation was set to the magic angle (54.7°). Removal of leaking 800 nm in the WL is achieved by putting an 800 nm, $0^0$ deg AOI hot mirror before focusing the WL onto

the sample. The TA system's temporal resolution is 150 fs measured from the cross-correlation between the pump and probe. Samples were held in 1-mm path length degassing quartz cells and continuously stirred during experiments using a magnetic stirring system. The optical density at the excitation wavelength was kept at ~ 0.3.

Figure 22 shows the experimental setup and correlates with the general scheme discussed.

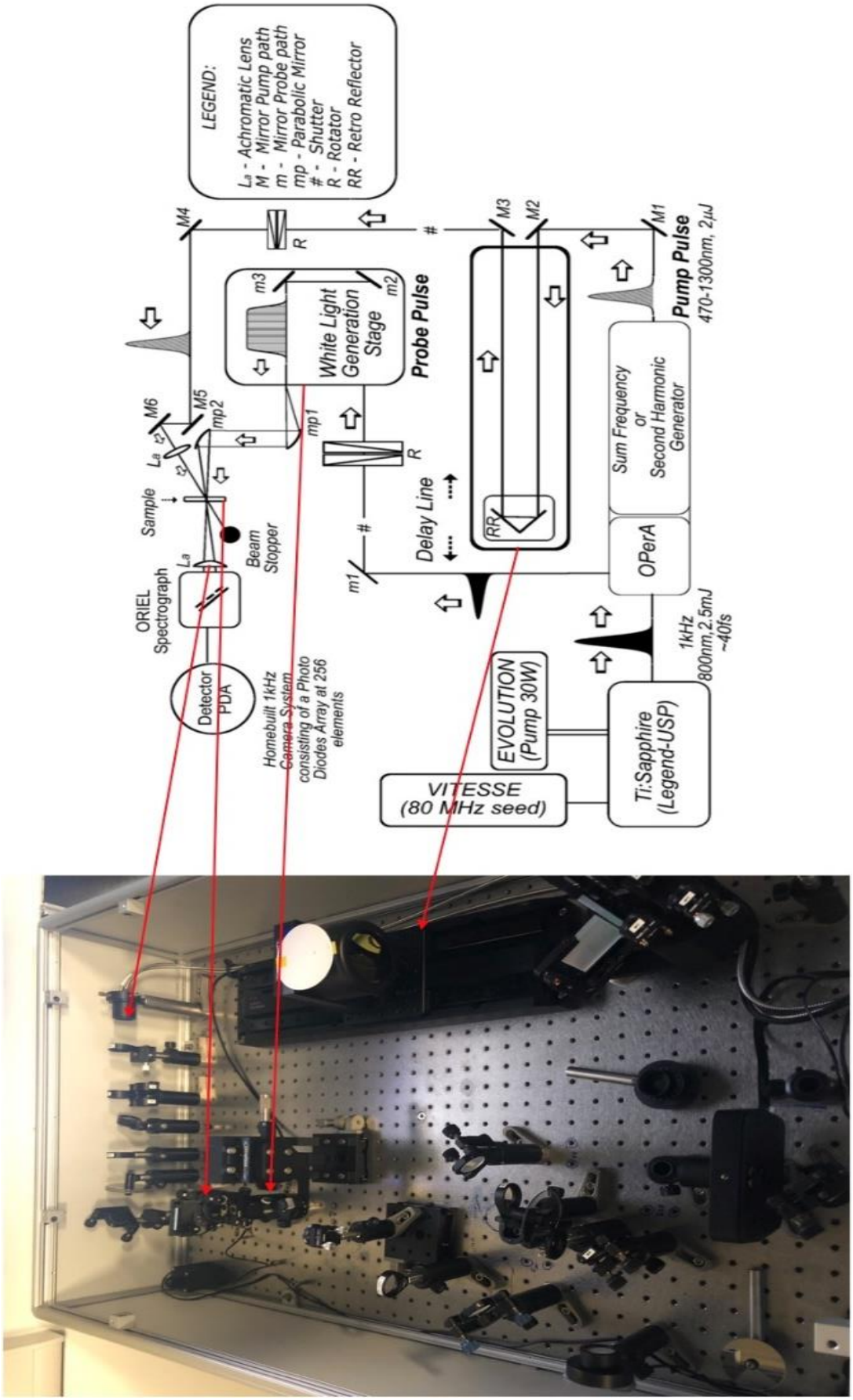


Figure 22- Helios Setup at Lord Porter Laser Lab. Schematic adapted from [61]

## Singlet-Oxygen Methodology

The laser setup consists of a Q-Switch Nd: YAG laser (n= 355 nm, 8 ns pulse length, laser model LS-1231M from LOTISII). A liquid nitrogen InGaAs photodiode detected the signal (J22D-M204-R03M-60-1.7, Judson Technologies). The output signal was recorded with a digital oscilloscope (TDS 3032B Tektronix). A high-contrast bandpass optical filter (1277 nm, 28 nm FWHM, by Izovac, Belarus) is placed on the setup to correctly select the singlet oxygen emission 72. Commercially available perinaphthenone is used as standard.

To ensure reliability, the samples and standard's optical density are the same at 355 nm. Singlet oxygen data were acquired with increasing laser power, up to 60 mJ, to avoid detector saturation. A linear relationship between singlet oxygen signal amplitude (y-axis) and power (x-axis) is obtained. The quantum yield value is obtained by dividing the sample fitted line slope by the standard fitted line slope.

## Data Analysis

Time-resolved data is analysed by a global analysis method suitable to fit the large volume of data in datasheets. To obtain a reasonable number of individual components, the number of exponential components gradually increased until the residuals were approaching zero, which was observed when the singular values displayed were too noisy with little or little structure. Glotaran[74], a graphical interface user software based on R package TIMP, the acronym "Global and Target Analysis", performed the fitting task for transient absorption data analysis. Glotaran was (initially) developed in the physics department of the VU University of Amsterdam.

As expressed several times, the absorption equation is a differential equation dependent on time and wavelength (see eq. 38). Adjustments must be made to get the kinetic expression for the overall process to arrive at the exponential decay expression. The expression of the absorbance in terms of exponential decays is given by:

$$\Delta A(\lambda, t) = c_1(\lambda)e^{-k_1\tau} + c_2(\lambda)e^{-k_2\tau} + c_3(\lambda)e^{-k_3\tau} + \cdots = \sum_{n=1}^{n} c_n(\lambda)e^{-k_n\tau} \qquad \text{(eq. 40)}$$

Where $c_n$ is the amplitude of the $n^{th}$ decay component as a function of wavelength, and $k_n$ is the rate constant for the respective exponential decay component where and $\tau_n$ represents the characteristic lifetime[71]. Adopting a parallel kinetic model, it is possible to monitor each component's rise and decay, called Decay-Associated Difference Spectra (DADS), and correspondent lifetimes. The final fitted data will simplify the analysis of the data and the process. The analysis results in the lifetime values, how many processes are happening (i.e. internal conversion, intersystem crossing, etc.) and the overall photochemical system's kinetic.

The global analysis uses the parallel kinetic model with mono-exponential decaying components, each represented by a single rate constant and an amplitude at each wavelength recorded. It is essential to always consider sequential models during this type of analysis, where all the process occurs in a specific order (i.e. 1→ 2→ 3…), which will lead to the evolution--associated difference spectra (EADS). The photophysical process happens in a sequence, one after another; this option is always ticked on; thus, parallel decay is not used.

XPS fitting was done by Avantage Analysis software from Thermo Scientific. The software uses a combination of Gaussians and Lorentzians to fit each spectra band. The software suggests a mix of 70% of Gaussians and 30% of Lorentzians, but this proportion can be adjusted well. The binding energy values for each band are assigned based on the fitted band generated and not the experimental peak. Any noisy or satellite bands were neglected during the analysis without losing any physical meaning. For elements containing spin-orbit coupling (i.e. metals or any other where the ejected electron is different from an s orbital electron since the L quantum number is different from 0), the peak of most significant intensity was used as a reference fitted in most cases, $p_{3/2}$. The final adjustments on the curves were made using OriginPro 8.0. The calculator for "Remaining Oxygen" uses the values of individual species contributions (i.e., amount of oxygen on the survey spectra, amount of carbonyl species in the high-resolution spectra, etc.) to calculate how much of the oxygen is not bounded to adventitious carbon.

## Theoretical Calculation (provided by Dr Cardozo)

Ground state and excited state geometry optimizations were performed at the B3LYP/def2-SV(P) level. Excitation energies were obtained at the TDDFT level of theory using B3LYP and the def2-SVPD basis set. Relaxed scans were used to obtain potential energy curves for the

stretching movement of the C-C bond connected to the carbonyl group in oxochlorin **2** and the corresponding C-C bond in OEP. Relaxed scans were carried out similarly for the out-of-plane carbonyl displacement. Both DFT and TDDFT calculations were performed using the TURBOMOLE 6.6 software. Spin-Orbit Coupling Matrix Elements (SOCME) between singlets and triplets were evaluated at the B3LYP/def2-SV(P) level using ORCA 4.2.12. Furthermore, the state averaged CAS (4,4) and CAS(8,6) calculations using def2-SV(P) and def2-SVPD basis set was performed to validate our TDDFT results using ORCA 4.2.1. The bonding used to calculate is the C-C bond adjacent to the carbonyl group.

# Chapter 4- Mechanisms of excited state decay in artificial porphyrins

## Isomers

Using the theoretical background presented in chapter 2 as a starting point, a more detailed approach to the porphyrins and the set shown in chapter 3 will be discussed. Prof. Bruckner highlights the formation of isomers (tautomers) during the products' synthesis [73]. This information is particularly important as the isomers' recombination will impact steady-state spectra and excited-state dynamics. The definition of Chlorins lies in the number of electrons conjugated and the positions of the conjugated bonds. A porphyrin has a 22 $\pi$-$e^-$ system, chlorin 20 $\pi$-$e^-$, and bacterio/isobacteriochlorins have 18 $\pi$-$e^-$. The difference between the last two lies in the position of the conjugated bond, bacteriochlorin on opposite sides and isobacteriochlorin on the same side (figure 18).

The crystal structures, via X-ray diffraction (XRD), of the oxochlorins, confirm their spectroscopically assigned symmetry groups. The symmetry of most OEP-derivatives belongs to the planar groups ($D_{2h}$, $D_{4h}$, etc.), although the out-of-plane distortions turn the molecule away from a perfect planar molecule. From all the samples, dioxo-isobacteriochlorin has a modest saddling conformation ($B_{2u}$). Figure 23 shows XRD details and calculations made by Prof. Bruckner and Dr Nemykin groups.

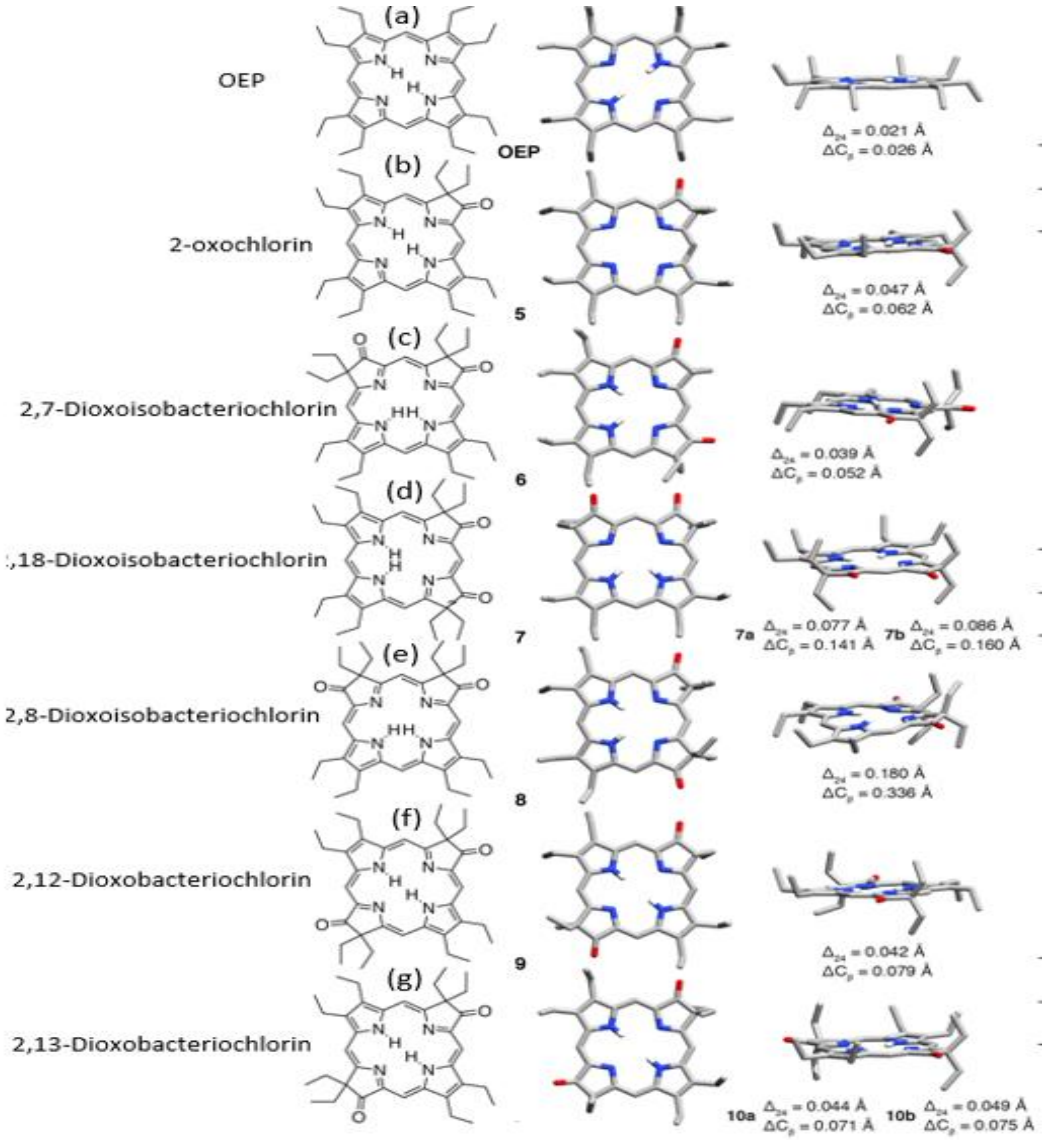


Figure 23- OEP set XRD and distortion, courtesy of Prof. Bruckner.

As shown in image 23, 2-dioxochlorin (labelled as 5) exhibits more planarity than the other isomers. Deviations are more pronounced in the case of 2,8-dioxoisobacteriochlorin (marked as 8) as a possible result of the gem-diethyl facing each other.

## Photophysical properties

As the substituted carbonyl group is electronegative, some level of interaction between the molecule and the solvent might be present, as the charge is initially weighted towards the oxygen atom and the solvent used to possess a polar character.

The characteristic features of porphyrin spectra are observed in all samples, as predicted by the Gouterman model, figures 24 and 25. Steady-state electronic absorption spectra show intense

Soret bands at 398-440 nm and Q-bands from 450-650 nm. An unexpected splitting in the Soret Band is present for most samples (around 400nm), and shoulders appear redshifted (regarding soret position). The theoretical model does not predict the splitting for any samples; thus, it is not credited to an extra electronic transition. Instead, it is due to the absorption of the isomers, which will be discussed later on. Comparisons of several B bands and Q bands are summarised in table 3 for all oxidised OEPs. From OEP to 2,7-dioxobacteriochlorin is observed a clear trend, an increasing redshift in all the bands. This information alone shows that the number of carbonyl groups and their relative position are vital in electronic transitions. A Stokes shift was also observed for OEP and 2,13-Dioxobacteriochlorin, whereas 2-oxochlorin and 2,12-dioxochlorin shifts are neglectable (less than 1 nm). Bacteriochlorins have a sharper soret band and less intense Q-bands than the isobacteriochlorins. The appearance of clear Q-bands is also noticeable for the bacteriochlorins. The dioxo-isobacteriochlorins, however, express a more chaotic behaviour, making it harder to interpret. More intense peaks for $Q_x(0,0)$ (increased oscillator strength) suggest a more allowed character for the transition when compared to OEP and the bacteriochlorin samples. Stokes shift is also more pronounced in these samples, with 2,8-dioxoisobacteriochlorin having 9 nm indicating a more distorted excited state. The Soret band is wider than the bacteriochlorins, and the Q-band has less structure. The orientation of C=O groups affects the energy levels of the frontier orbitals, which affects the steady-state spectra[74,75].

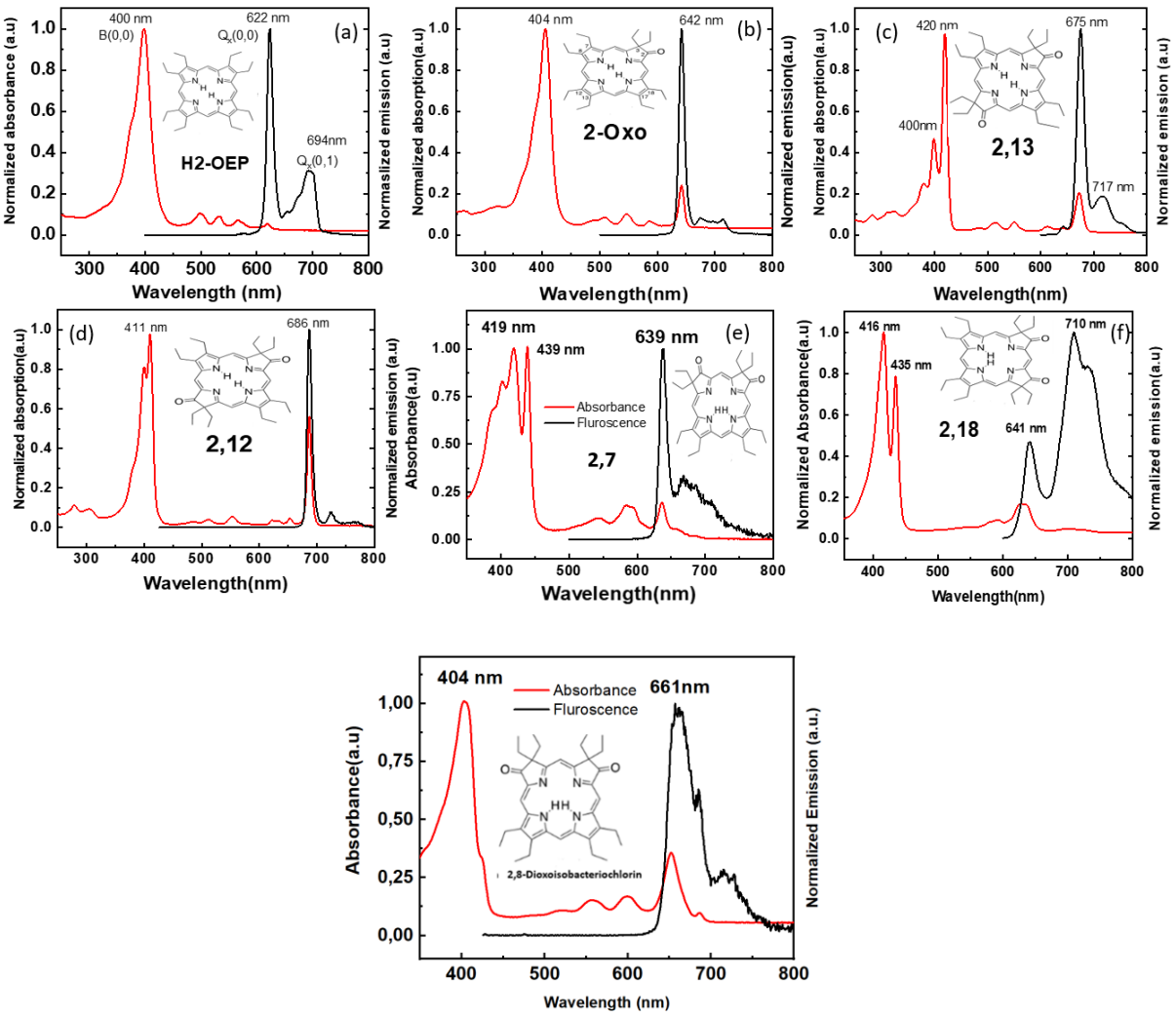


Figure 24- Absorption and emission spectra for OEP and modified porphyrins in DCM

Table 3- Band positions for porphyrins.

| Sample | Soret Band position (nm) | Qy (1,0) position (nm) | Qy (0,0) position (nm) | Qx (1,0) position (nm) | Qx (0,0) position (nm) | Emission main peak (nm) | Stokes Shift (nm) |
|---|---|---|---|---|---|---|---|
| OEP | 400 | 499 | 533 | 565 | 620 | 622 | 2 |
| 2-oxochlorin | 404 | 509 | 547 | 585 | 642 | 642 | - |
| 2,13-Dioxob. | 400/420 | 515 | 551 | 613 | 673 | 675 | 2 |
| 2,12-Dioxob. | 400/411 | 555 | 638 | 653 | 686 | 686 | - |
| 2,7-Dioxoisob. | 419/439 | 544 | 582 | 592 | 637 | 639 | 2 |
| 2,18-Dioxoisob. | 416/435 | 577 | 593 | 627 | 636 | 641/710 | 5 |
| 2,8-Dioxoisob. | 404/424 | 517 | 556 | 600 | 652 | 661 | 9 |

Similar behaviour can be observed across the emission pattern. Luminescence appears in the near IR wavelengths, as shown in figures 24 and 25. The principal peak redshifts position is similar to the absorption spectra: band position moving into lower energies from OEP up to 2,12-dioxobacteriochlorin. In the literature, this effect was ascribed to out-of-plane distortions in the conjugated macrocycle [51,74–76] when the porphyrin ring is attached to bulky substituents.

## Time-Resolved Measurements

TCSPC measurements elucidate the fluorescence dynamics of the samples. A single lifetime is observed for all the samples. The need for two components to fit the 2,18/2,7 dioxo-isobacteriochlorins data might indicate tautomers' presence. The values of the lifetimes are shown in figure 26. Interestingly, 2,8-dioxoisobacteriochlorin is fitted satisfactorily with a single exponential (instead of a typical multi-exponential decay), suggesting that the carbonyl position has some significant impact (in this, isobacteriochlorin is where the group is more distant from each other). We observed a considerable decrease in the lifetimes by adding one and two carbonyl groups. The relative position of the hydrogen and the carbonyl also impacts photophysics: isobacteriochlorins excited states decay faster than bacteriochlorins.

Overall, the lifetime decreases for all samples compared to the OEP and 2-Oxochlorin. A similar decreasing trend is observed within the groups: 2,13-dioxochlorin has a faster decay than 2,12-dioxochlorin (2.65 ns and 3.16 ns, respectively)– once again, the carbonyl group is further away from each other. 2,8-dioxoisobacteriochlorin also shows a faster decay within the isobacteriochlorin samples.

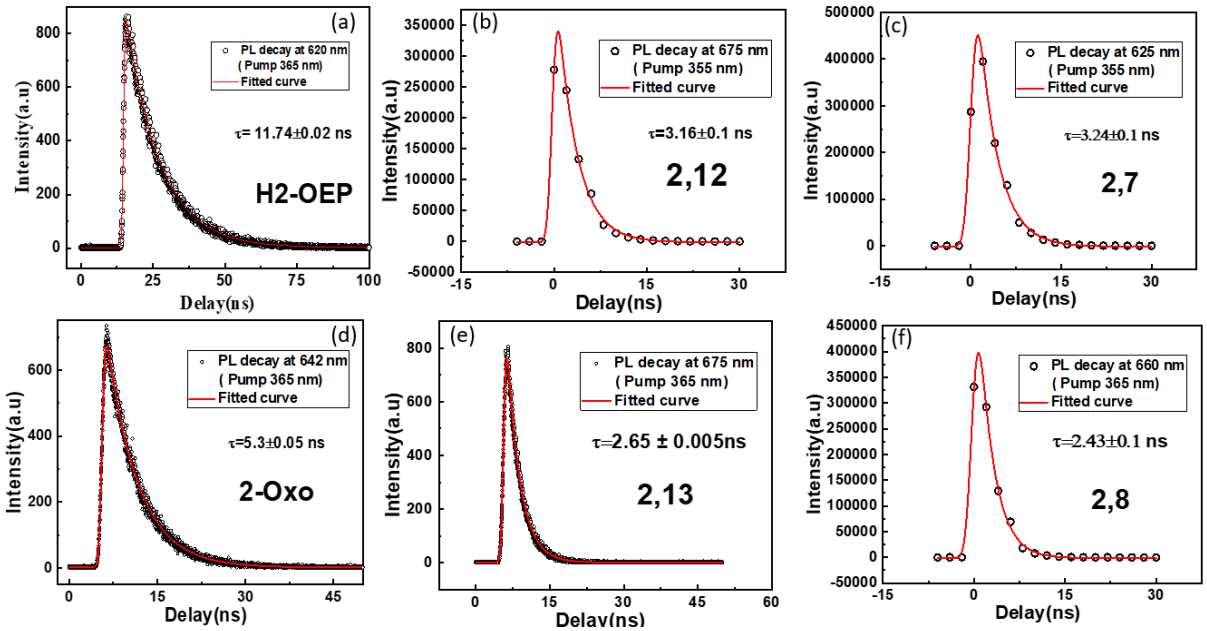

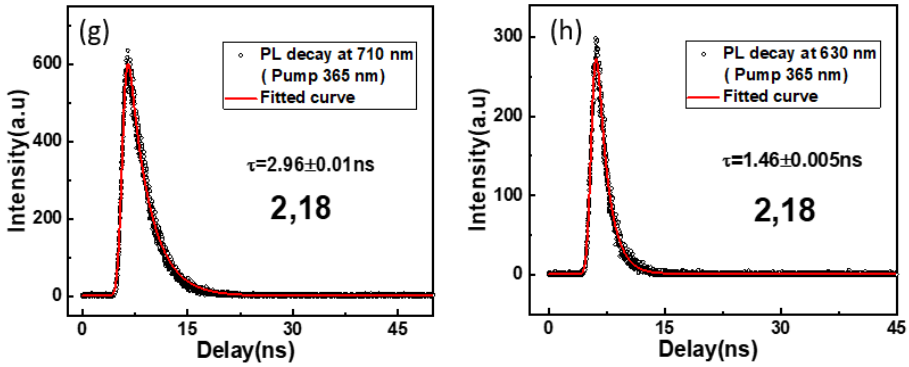


Figure 25- TCPS Spectra and decay constants for all the samples. a) $H_2OEP$, b) 2,12-dioxobacteriochlorin, c)2,7-dioxoisobacteriochlorin, d) 2-oxochlorin, e)2,13-dioxobacteriochlorin, f)2,8-dioxoisobacteriochlorin, g/h) 2,18-isobacteriochlorin (two lifetimes)

The trend in lifetime may be related to the oscillator strength increase for $Q_x(0,0)$. Table 4 shows the values for PLQY for all the samples and uses $Ru(bpy)_3^{2+}$ as a reference. Samples were excited at 416nm, and emission was collected gradually decreasing the solutions' concentration. ISC rates are calculated, as shown by Turro[18].

Table 4- PLQY and ISC rates for the porphyrin samples in DCM

| Sample | PLQY (DCM) | Emission Lifetime (ns) | ISC rate |
|---|---|---|---|
| OEP | 0.041 | 11.7± 0.02 | $8.2x10^7$ |
| 2-Oxochlorin | 0.034 | 5.3± 0.05 | $1.8x10^8$ |
| 2,13-Dioxobac. | 0.052 | 2.65±0.01 | $3.6x10^8$ |
| 2,12-Dioxobac. | 0.046 | 3.16±0.1 | $3x10^8$ |
| 2,7-Dioxoisobac. | 0.029 | 3.3±0.14(637nm)<br>3±0.08(675nm) | $2.9x10^8$ |
| 2,18-Dioxoisobac. | 0.051 | 2.96 ± 0.01(640nm)<br>1.46±0.005(675nm) | $3.2x10^8$ |
| 2,8-Dioxoisobac. | 0.045 | 2.48±0.09 | $3.8x10^8$ |

*Measurements by Dr Sayantan Battacharya

## Transient Absorption

Femtosecond TA spectra were collected for all samples in DCM and excited into the Soret band with a pump wavelength of 400 nm. For the sake of clarity, the data will be split into three groups: (i)OEP, (ii) 2-Dioxochlorin/2,12-Dioxobacteriochlorin/2,13-Dioxobacteriochlorin, (iii) 2,7-Dioxoisobacteriochlorin/2,18-Dioxoisobacteriochlorin/2,8-Dioxoisobacteriochlorin.

The grouping facilitates comparison and was chosen based on the molecules' structural similarities. However, the discussion and comparison of the data will be made simultaneously. The relaxation from $S_2$ to $S_1$ and $Q_y$ is expected to occur within the first few hundred femtoseconds[46,49]. However, because the resolution of our fs-ns TA is ~150 fs, only $Q_x$ excited state dynamics can be successfully measured ($Q_x$ relaxation and ISC).

## Femtosecond Transient Absorption

### (i) OEP

Figure 26 displays the excited state dynamics for the OEP sample. Delay points were selected to elucidate dynamics in areas of interest of the sample. TA spectra (a) show an intense GSB in the Soret region, followed by ESA and the subsequent bleach of the Q bands. Is it worth mentioning that the bleach of the Q bands overcomes ESA; nonetheless, it is negative. ESA signal shows different relaxation dynamics depending on probe wavelengths. Transient recovers gradually within the span of 7ns with varying scales of time.

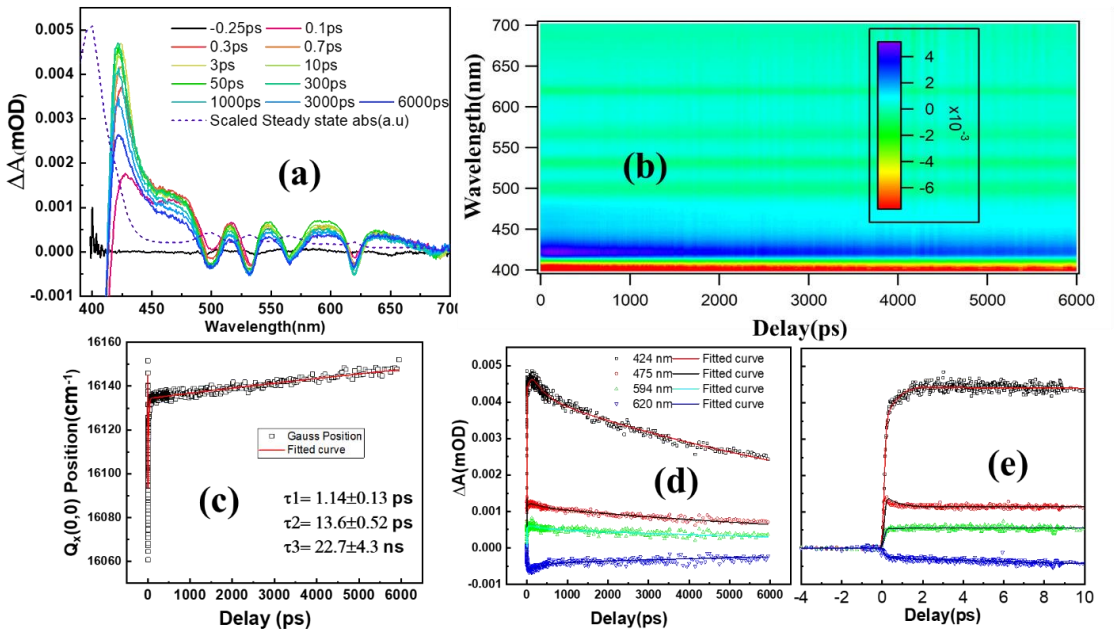


Figure 26 H2OEP sample in DCM - a) TA spectra, b) contour map for whole spectra c) Qx (0,0) band shift temporal profile, d) kinetic profile, e) early time kinetic traces. All in DCM.

Kinetic profile (d and e, figure 26) shows that the ESA goes through different relaxation depending on the wavelength region. It has been documented[50] that a red shift followed by a blue shift for the Qx(0,0) band for different time delays. To elucidate these phenomena, the Qx(0,0) bleach is fitted for all delay positions and plotted as a function of delay (figure 26 c). Baskin et al. [79] described the phenomena as a mix of cooling dynamics and shift processes. The Qx(0,0) lifetimes obtained by TA and TCPCS are also concording with the cooling mechanism literature via solvent interaction. [77,80,81] This feature will be further explored in the discussion section.

(ii) 2-Dioxochlorin/2,12-Dioxobacteriochlorin/2,13-Dioxobacteriochlorin

TA spectra and kinetic decay for the samples are shown in figure 27. Compared to the regular OEP, those samples show a more intense Qx(0,0) band; this is reflected in TA spectra as a prominent bleach on the region. For all the samples, kinetic spectra also do not decay entirely within the 7ns time window, suggesting a long-lived species, and as such, a non-decaying component is needed to fit the end tail of the kinetics.

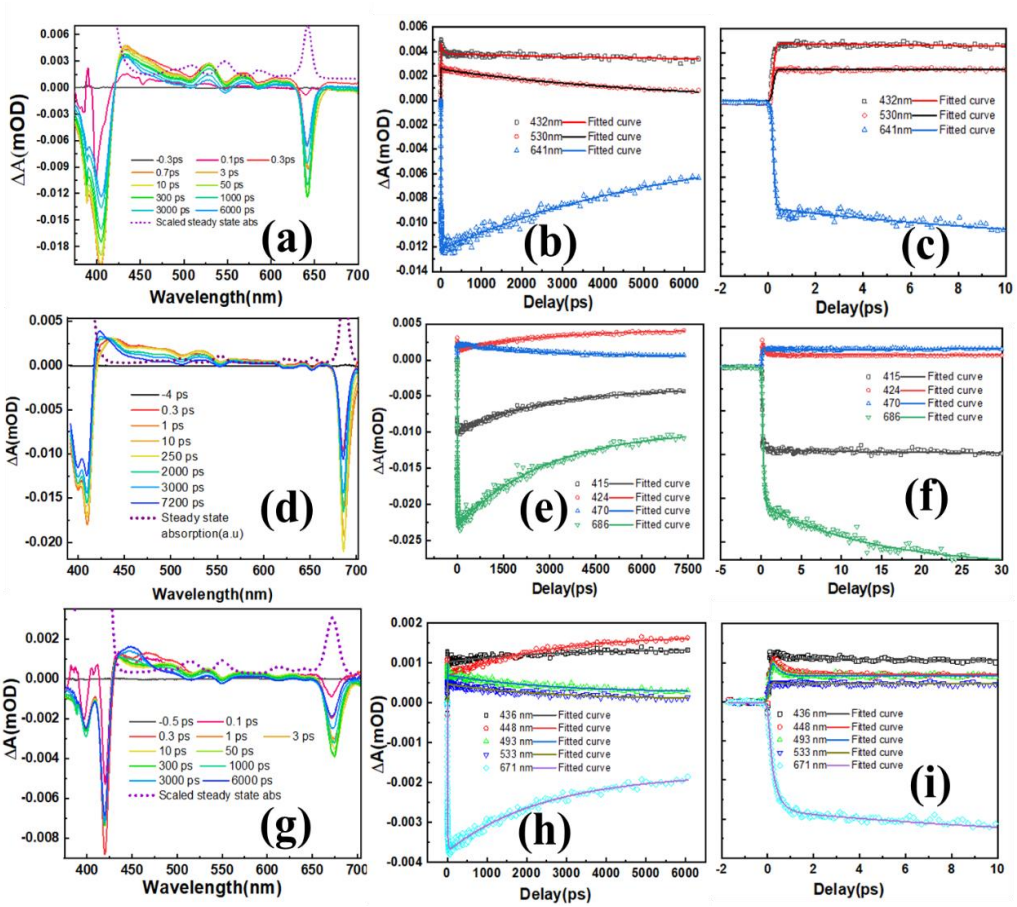


Figure 27- TA spectra (in DCM) for 2-dioxochlorin (a), 2,12-dioxobacteriochlorin (d) and 2,13-dioxobacterio chlorin (g) and their respective kinetic profile (b/c,e/f and h/i)

iii) 2,7-Dioxoisobacteriochlorin/2,18-Dioxoisobacteriochlorin/2,8-Dioxoisobacteriochlorin

Similarly to the (ii) group, the spectra shown in figure 28 have an intense bleach reflecting the $Q_x$ (0,0) (which has increased oscillator strength in the steady-state spectra). This third group also indicates the existence of long-lived triplet states. As observed in the previous group, the region between 450 and 550 nm exhibits decreased ESA, while the 410-450-nm region shows a delayed signal increase.

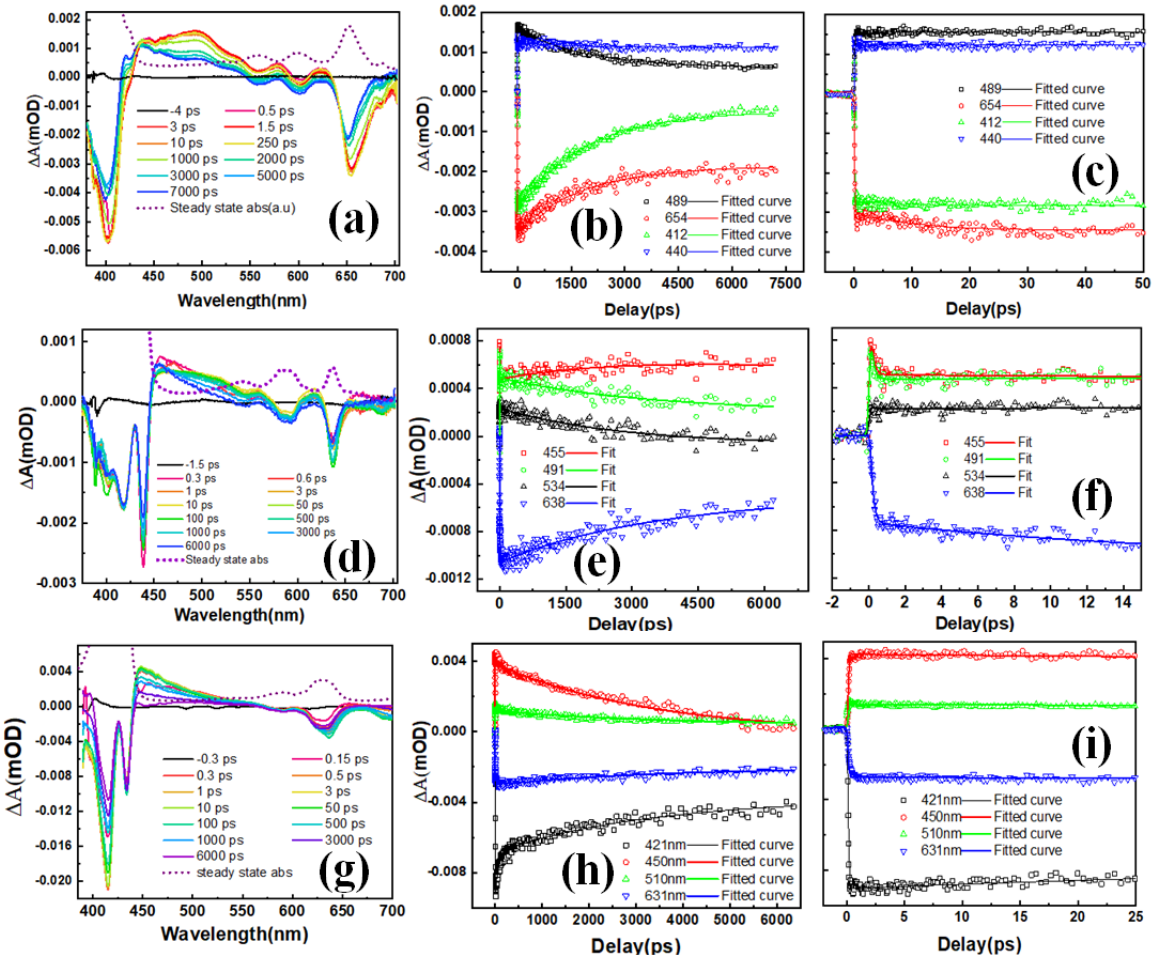


Figure 28- TA spectra in DCM for 2,7-dioxoisobacteriochlorin (a), 2,18-dioxoisobacteriochlorin (d) and 2,8-dioxoisobacteriochlorin (g) and their respective kinetic spectra (b/c,e/f and h/i).

## Discussion

Summarising the time constants used to fit the data appropriately facilitates understanding of each sample's photophysics, Table 5. The first-lifetime component increases as one carbonyl group is added, whereas a decrease is seen in all other samples (apart from 2,18-dioxoisobacteriochlorin and 2,8-dioxoisobacteriochlorin). The hundreds of fs component is usually attributed to IVR and IC from $S_2$ states to $S_0$. Previously, it was reported that this feature is present in fluorescence as decay on the blue side of emission spectra and not on longer wavelengths[77]. As discussed, internal conversion between Q bands occurs within the first few femtoseconds, thus not observed in these measurements. The second component is around

~10ps for all the samples except for 2-Oxochlorin and 2,18-Dioxoisobacteriochlorin. The Qx band tracking (figure 28c) shows that the 10-20ps component is expected to coincide with the relaxation via coupling between solvent and excited state. It is facilitated by the renormalisation of the frontier orbitals energy gap, as the polar solvent interacts with the electrons on the orbitals. It is followed by an expansion of the macrocycle and gradual recovery of the porphyrin ring via vibrational cooling. Non-decaying components are needed to fit the data tail, but its lifetime is higher than 15ns.

Table 5- TA time constant values obtained.

| Sample | τ1(ps) | τ2(ps) | τ3(ps) | τ4(ps) | τ5(ps) |
|---|---|---|---|---|---|
| H2-OEP | 0.63 ± 0.02 | 13.9 ± 1.2 | 57.5 ± 5.1 | 315.5 ± 22.4 | 10594 ± 131 |
| 2-Oxochlorin | 15.3 ± 0.9 | 69.3 ± 18.3 | 5674 ± 482 | non-decaying | - |
| 2,12-Dioxobac. | 0.19 ± 0.02 | 14.3 ± 1.2 | 2833 ± 45 | non-decaying | - |
| 2,13- Dioxobac. | 0.42 ± 0.01 | 18.6±1.4 | 2423 ± 99 | non-decaying | - |
| 2,7- Dioxoisobac. | 0.19 ± 0.01 | 18.5 ± 1.2 | 2815 ± 251 | non-decaying | - |
| 2,8-Dioxoisobac. | - | 10.8 | 1883 ± 99 | non-decaying | - |
| 2,18-Dioxoisobac. | - | 89.4 ± 3.8 | 3336± 202 | non-decaying | - |

OEP's third and 2-Oxochlorin's second components are equivalents (~50 ps time-scale) and correspond to VR dynamics either by solvent inelastic collisions or conformation relaxation due to non-planar distortion of the macrocycle. It was predicted by the Dr Nemykin group the possibility of tautomerism for the isobacteriochlorin samples. Piotr et al. reported double proton transfer in porphycenes to be around ~190 ps, which is highly dependent on the strength of the hydrogen bonding; hence the distance N-N is relevant[78]. The 90-ps component in 2,18-Dioxobacteriochlorin may be assigned to ultrafast proton transfer. The third component is a rise component that builds up the signal profile on the 10 to 100-ps time window. All nanosecond components match the TCSPC data and are thus safely assigned to $Q_{x(0,0)}$ 's lifetime. A trend is clearly observed as the $Q_x$ lifetime decreases with the increasing number of carbonyl groups. Therefore, ISC rates suggest a 2-fold increase in the ISC rate for OEP and 2-Oxochlorin and a 4-fold increase from OEP to bacteriochlorin and isobacteriochlorin. This trend might be correlated with a SOCME increase between $S_1$ and triplets, as it will be further explored in the DFT calculations section.

## ns-Transient Absorption (measured by Dr Battacharya)

The femto/picosecond TA shows a non-decaying signal, which might be related to the triplet state dynamics; furthermore, a longtime setup is needed. The data collected and the time constants values are shown in figure 29 and 30 and Table 6. This data first component in accord with fs-TA describes the Q band dynamics and subsequent ISC to the triplet states in agreement with fs-TA. Multiexponential decay is observed for each data set, where three components are used to fit OEP, 2-Oxochlorin, and the bacteriochlorin group, whilst two suffice for isobacteriochlorin. A non-decaying component may be assigned to triplet transitions, suggesting that the carbonyl group can tune ISC from Q bands to triplets via a spin-vibronic channel[52,74]. As the non-decaying component lies beyond the detection limit, 50 μs was set to fit the exponential end-tail.

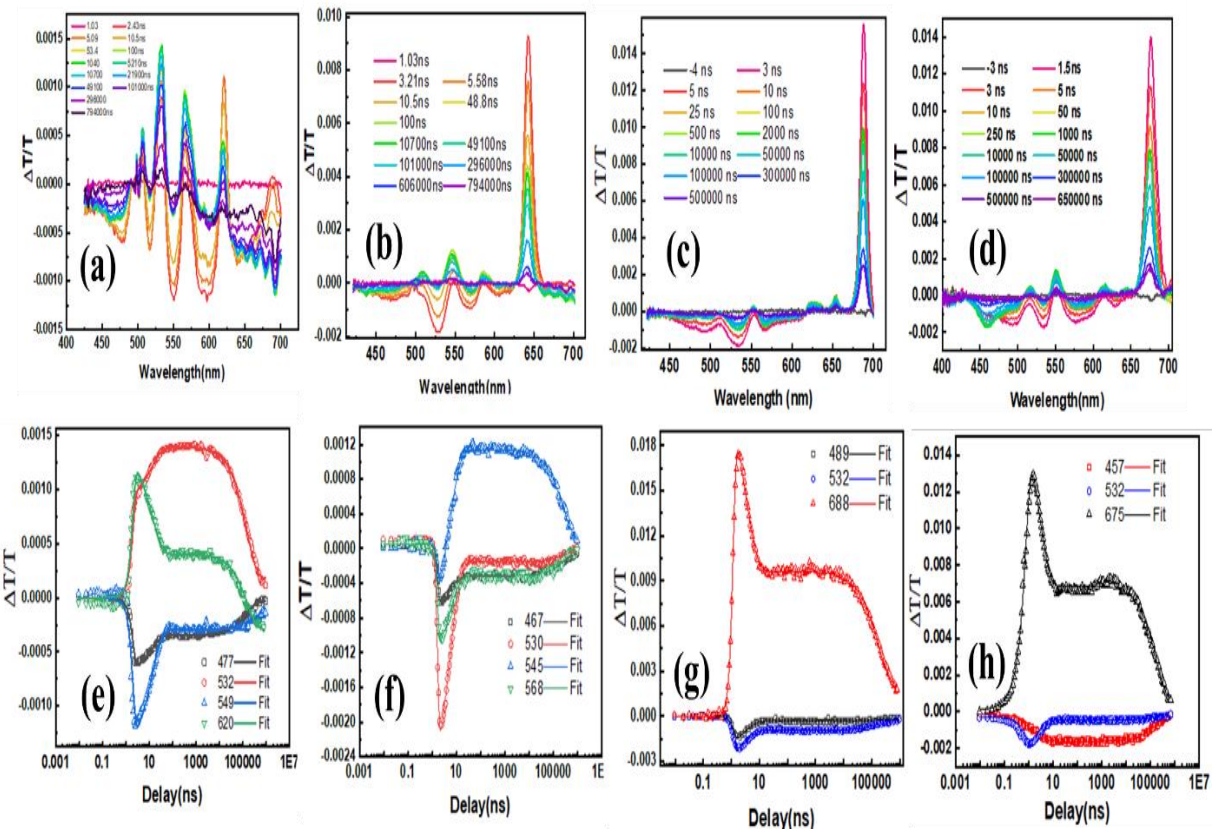


Figure 29- a,b,c and d – ns-TA for OEP, 2-oxochlorin, 2,12-dioxobacteriochlorin and 2,13-dioxobacteriochlorin in DCM, 350nm excitation. The bottom row is the respective kinetic profile.

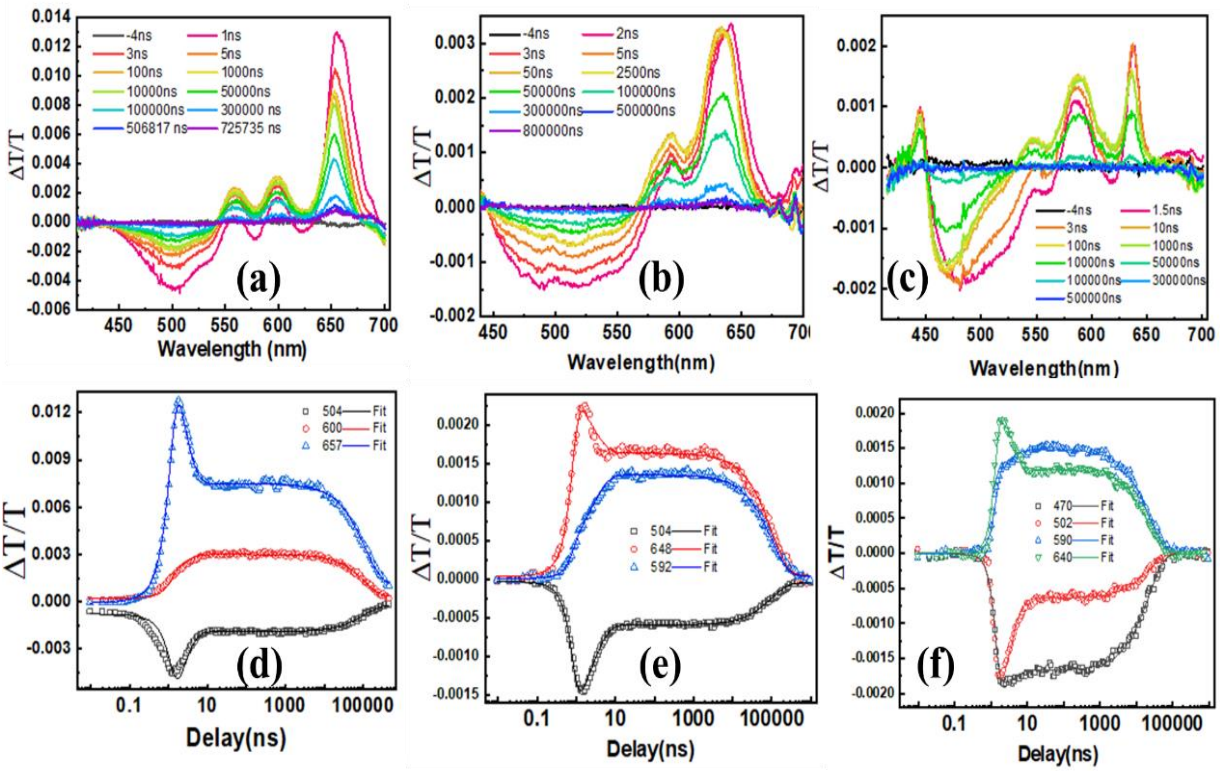


Figure 30- a,b and c – ns-TA for 2,8-dioxoisobacteriochlorin, 2,18-dioxoisobacteriochlorin and 2,7-dioxoisobacteriochlorin, in DCM, 350nm excitation. The bottom row is the respective kinetic profile.

Table 6- ns-Transient Absorption time constants in DCM. 350nm excitation.

| Sample | τ1(ns) | τ2(μs) | τ3(μs) |
|---|---|---|---|
| H2-OEP | 12.4±0.4 | 146±3.2 | non-decaying |
| 2-Oxochlorin | 5.2±0.1 | 254±8.4 | non-decaying |
| 2,12-Dioxobac. | 3.1±0.05 | 163±2.9 | non-decaying |
| 2,13-Dioxobac. | 2.2±0.05 | 172 ±11 | non-decaying |
| 2,7-Dioxoisobac. | 3.2±0.1 | 108 ±4.1 | - |
| 2,8-Dioxoisobac. | 1.8±0.1 | 97 ±1.7 | - |
| 2,18-Dioxoisobac. | 2.4±0.1 | 22 ±2.2 | - |

Like the short-time TA and TCSPC, increasing the number of carbonyls decreases the early component's lifetime value (τ1). The second time constant was an overall increase from OEP to 2-oxochlorin and the bacteriochlorins. Isobateriochlorins, however, a decrease is observed from 2,7 to 2,18. τ2 is assigned to the triplet transition back to the ground state. As observed, the number and position of carbonyl groups can either enhance or decrease the triplet lifetime. The reasoning behind this needed theoretical calculations to understand how it affects the

energy of excited states. Our collaborator Dr Thiago used computational methods to unveil what was happening.

## Theoretical Calculations (Dr Thiago Cardozo and Karol Gomes)

As the experiments showed, the increasing carbonyl amount made the decay (both from singlets and triplets). Using computational chemistry allows for predicting these states' energy behaviour and simulating bond stretching.

Calculations were made for OEP, 2-Oxochlorin, 2,13-bacteriochlorin and 2,18-isobacteriochlorin (one of each group). All images and data presented in this section are courtesy of Dr Cardozo and Karol Gomes.

Figure 31 shows the frontier orbitals for each sample; as expected, they behave mostly as described by the 4-orbital model Gouterman predicted [33,34], except for 2,18-dioxoisobacteriochlorin. A few deviations, such as some band predictions on the simulated spectra, are in Figure 33. These are not yet fully understood, but the splitting observed on B bands is more likely due to tautomers' presence. However, the increased oscillator strength for $Q_x$ (0,0) is neither predicted in intensity nor position.

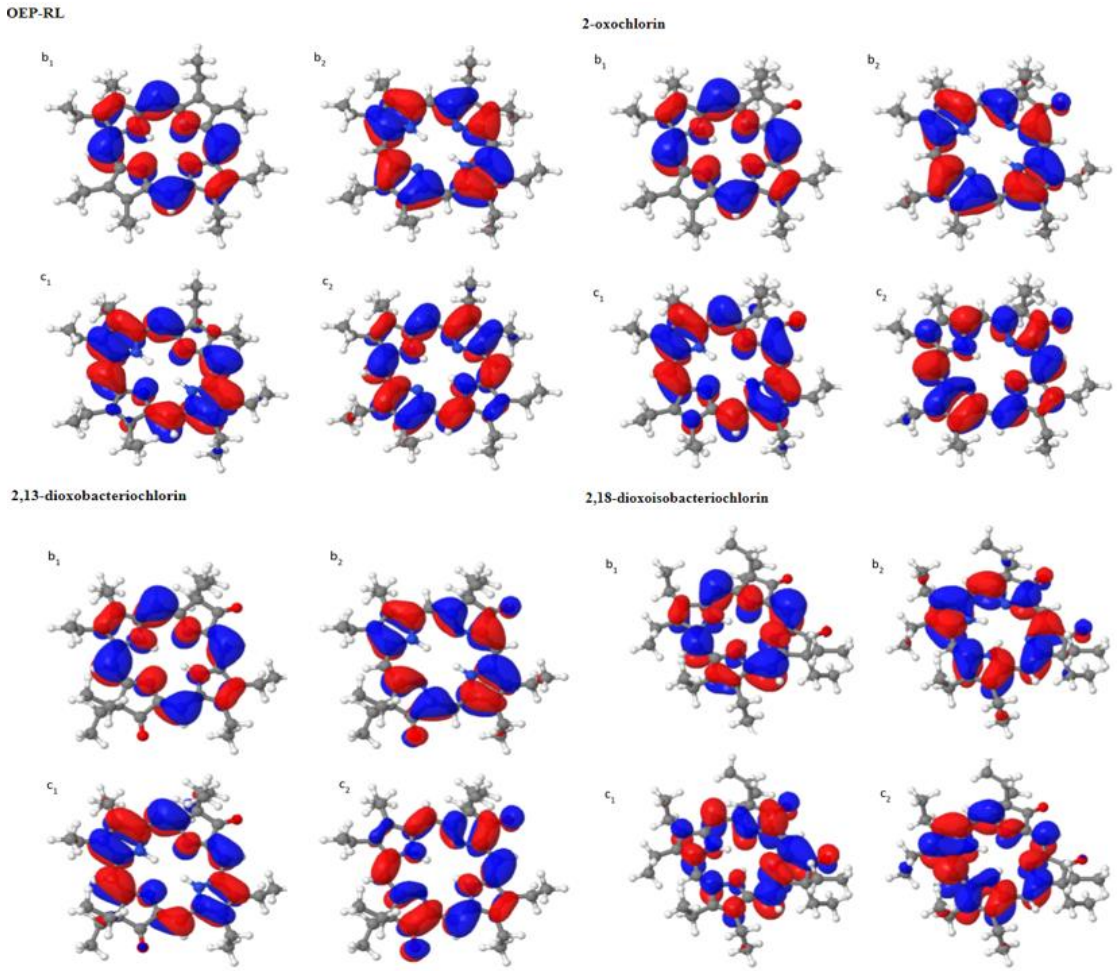


Figure 31- Frontier Orbitals for OEP, 2-oxochlorin, 2,13- Dioxobacteriochlorin and 2,18-dioxoisobacteriochlorin

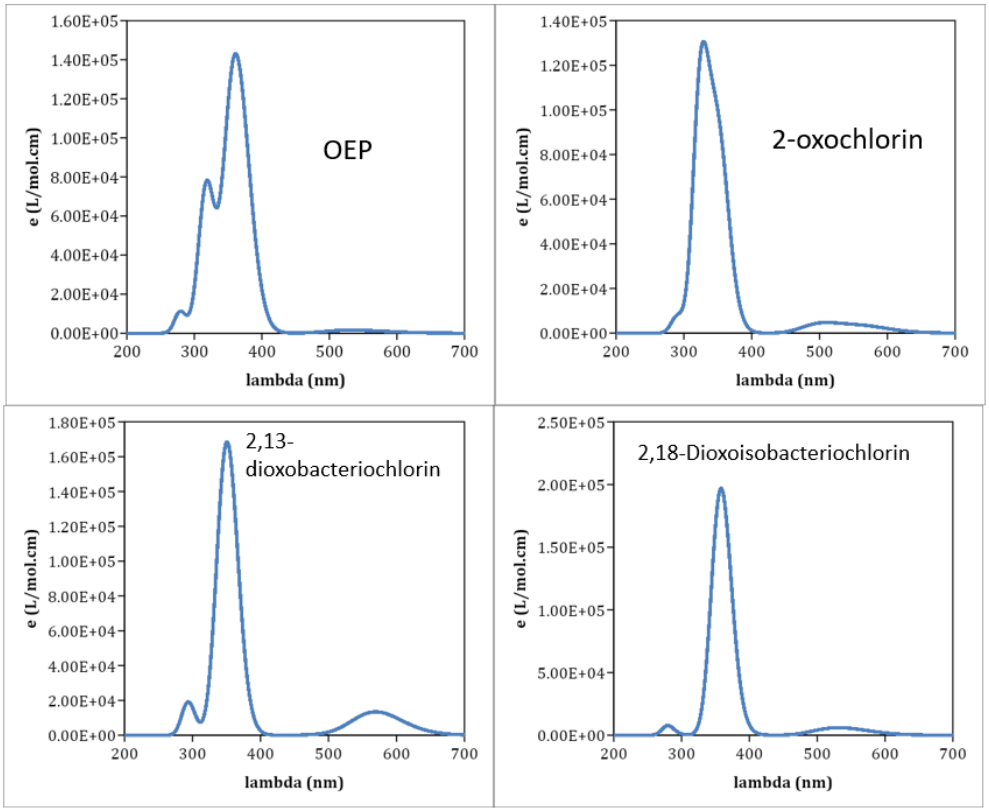


Figure 32- Simulated spectra for the samples.

## C-C stretching

The macrocycle expansion plays an essential part[74,79] in the decay mechanism. To fully understand this process, the C-C stretching behaviour was analysed. As the bond stretches, all states increase in energy. The energy increment is not equal to all states; some increase more than others, reducing the next excited state's distance for the molecules with C=O. Figures 34 and 35 illustrate the C-C bond stretching along the breathing mode and the energy change in several excited states. Breathing mode is also represented by a gif image in the supplementary material. Steps refer to the geometry distortion of the molecule, 0 being the equilibrium geometry. Each step represents the molecule breathing mode in a different geometry, meaning each step stretches the whole molecule in the same way as the vibrational distortion performed. It is worth noting that the nomenclature of the calculated states is different from the previous spectroscopic notation. For understanding and simplifying, the state's label (i.e. $S_2$ means the Soret band, but the second state that appeared from the calculations and so forth) from the calculations will be used in this part. Singlet separation, figure 34, shows a possibility of IC from bright states from higher energy levels for all oxygenated samples, as the energy gap

between levels decreases with the increasing number of carbonyl substituents. The C-C-stretching also shows no direct crossing between singlets and the ground state. That is also true for the triplet states crossing (Figure 35), meaning that the node alone is not responsible for the whole decay process, although it does affect a good part of it. Red arrows indicate the lowest values between states with minimal energy values.

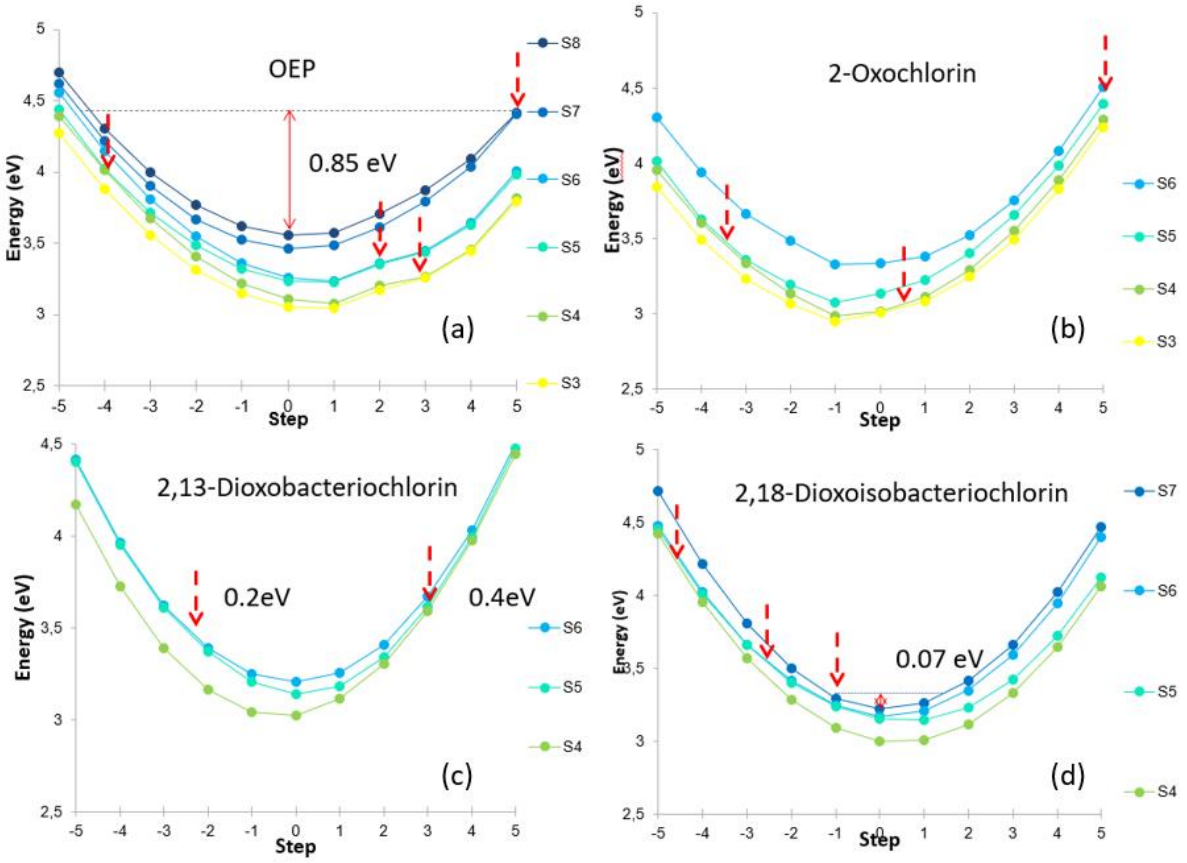


Figure 33- Excited singlet state energy level, C-C stretching. a) OEP, b)2-oxochlorin, c) 2,13-Dioxobacteriochlorin, d) 2,18-dioxoisobacteriochlorin

Dashed lines in figure 35 represent the triplet states. Triplets and Siglets approach each other (in energy, y-axis) as C=O more C=O is added, facilitating ISC. It is clear that in step 5, the energy approximation of the states explains the faster decay rate. It is worth mentioning that the number of crossings cannot alone explain the difference between one carbonyl to two carbonyl crossing rates. There is insufficient evidence to support that increasing carbonyl groups mean more crossings; however, the molecules have extra sites where this specific C-C

stretching can happen (two sites on dioxo vs one on oxo). Hence two crossing versus one crossing probability occurs.

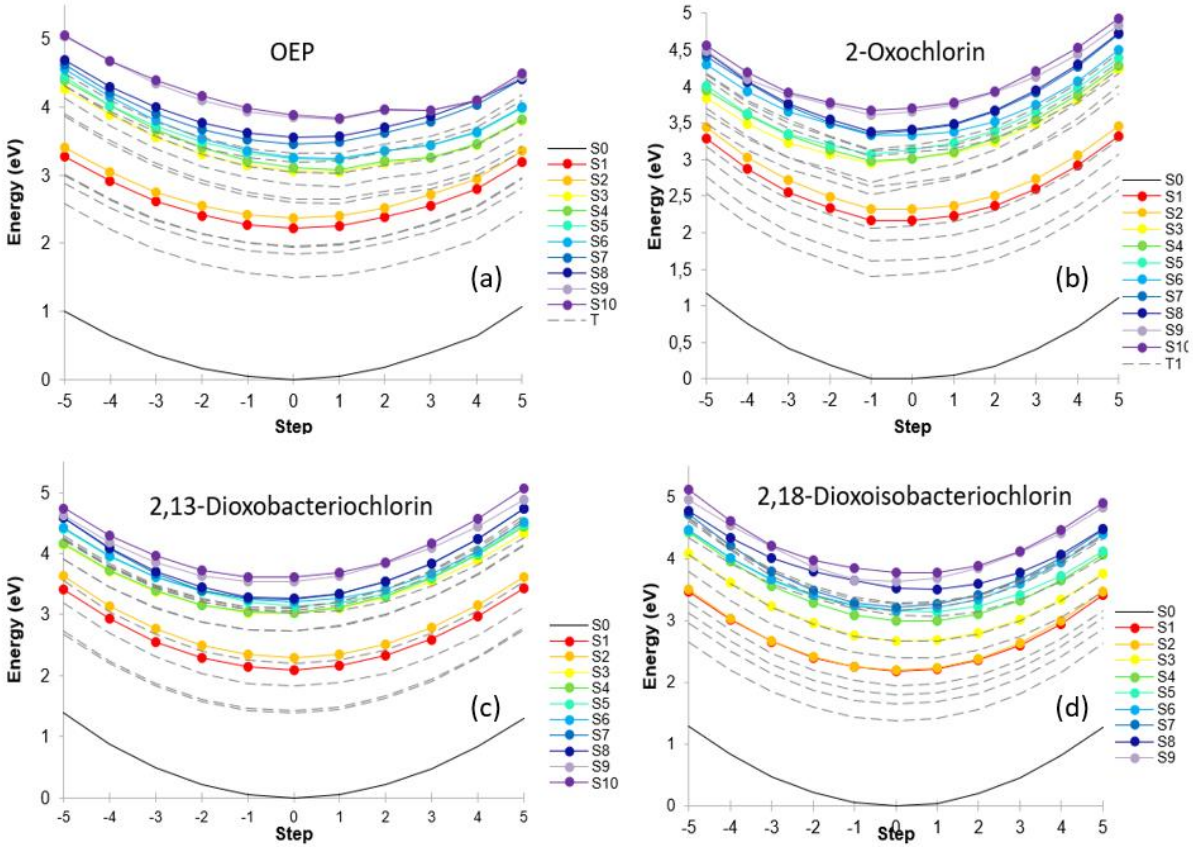


Figure 34- Excited Singlet/Triplet states level, C-C Stretching

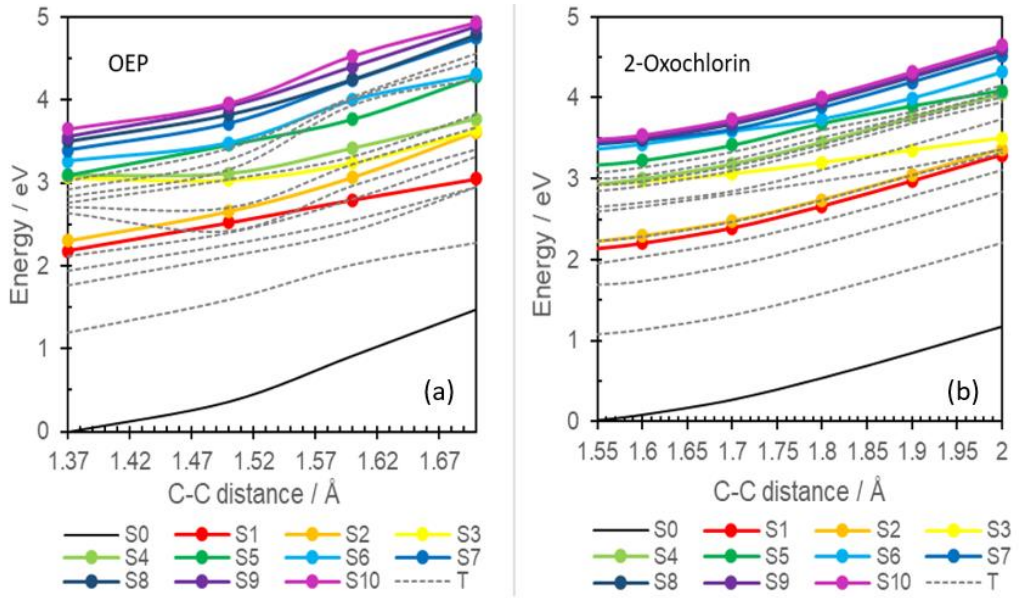


Figure 35- C-C distance and energy levels.

Figure 36 shows the effect of C-O stretching. The larger the stretch, the closer the singlets and triplets are to each other. Molecules containing carbonyl need less energy to reach the crossing point. This small gap should impact the Q band excited state, making it decay faster than the OEP sample.

## C-O Stretching

Singlet and triplet states approach each other when the distance between them is approximately 1.6 Å through carbonyl stretch along the breathing mode (figure 37). However, dioxochlorins require almost two times more energy than oxochlorin for the crossings to happen, suggesting that stretching might be as important (i.e., increasing the crossing probabilities or decreasing states energies) for these molecules.

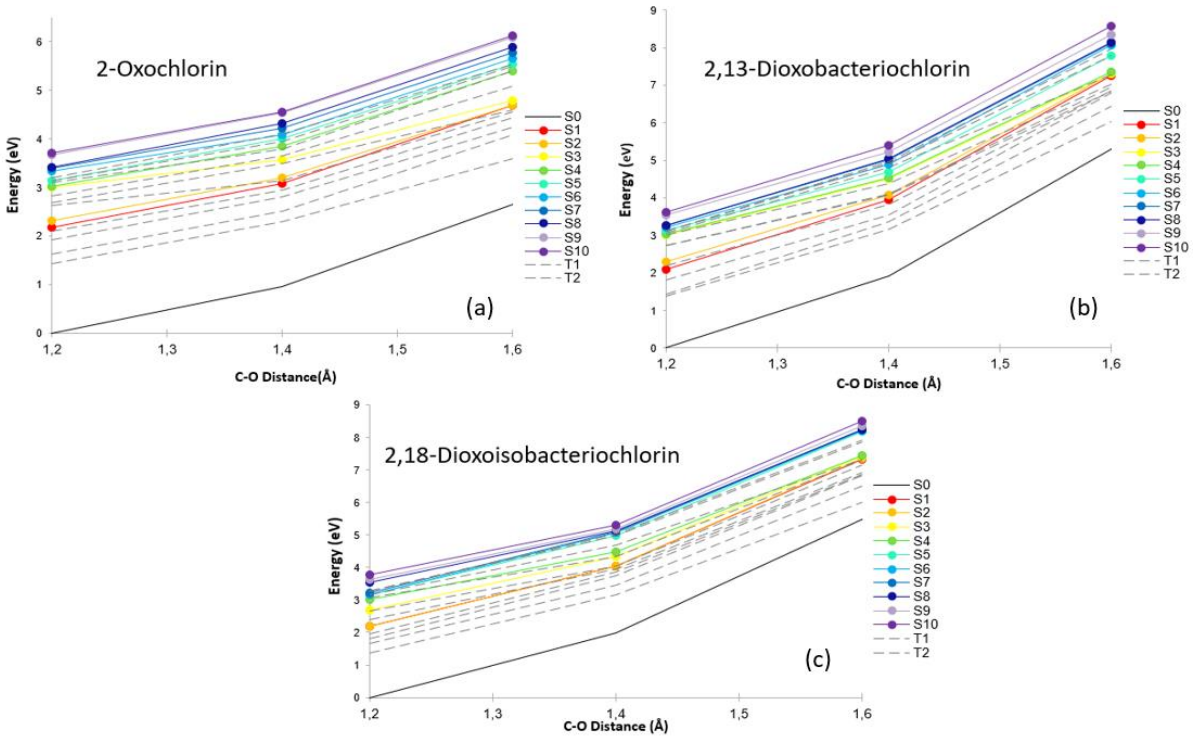


Figure 36- Excited singlet/triplet energy levels, C-O stretch.

The data indicate that Soret to Q-bands conversion is faster for the oxygenated molecules as the number of channels connecting higher energy states with Q bands increases. Accessing the crossing requires around 2 eV (starting from the Franck-Condon region), two times higher than for the C-C stretch, figure 38.

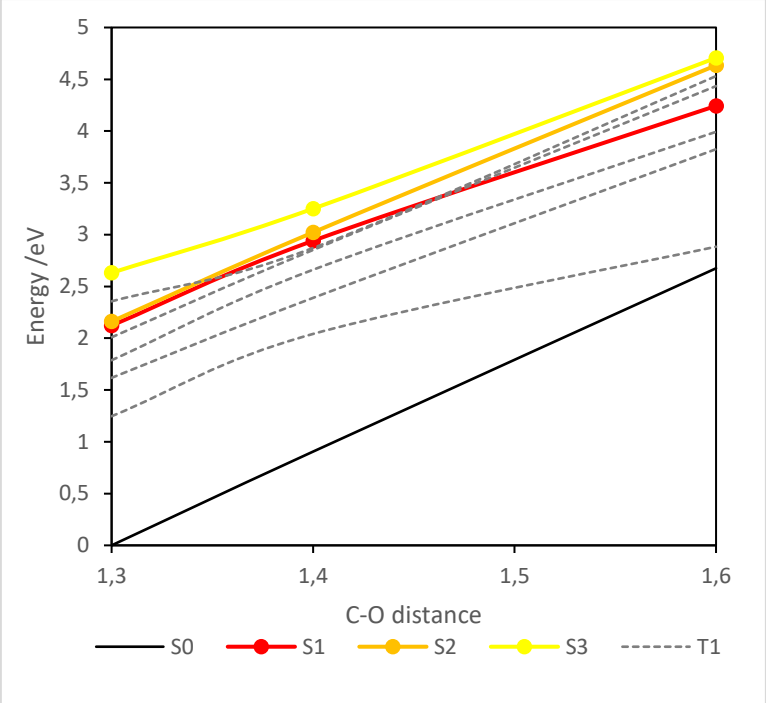


Figure 37- C-O distance Energy level

Dr Cardozo calculations show no significant difference in oscillator strength between Q bands and Ground State transitions; thus, they do not explain the increased fluorescence. It is possible that vibronic coupling or faster arrival at Q-states bands via non-radiative decay might enhance radiative decay. As the oscillator strength does not vary much, the faster arrival at the Q states might be behind the increased excited state population. Dr Cardozo checked the Q band to ground state oscillator strength along the out-of-plane distortion along the C=O stretching and found no evidence of these motions promoting any significant increase.

### Spin-Orbit coupling

New crossings are available between Q state bands and higher energy triplet states whenever the angle of the carbonyl group and the molecular plane increases. As Q states energy and the first triplet state are far apart, it is more likely that the crossing happens between singlets and higher energy triplets states $T_n$ (n= 3, 4, 5). Figure 39 relates the SOCME, angle and energy for an out-of-plane distortion of the C=O. The minimum difference in energy coincides (around 55 degrees) with the maximum spin-orbit coupling, suggesting greater crossing probabilities, thus a faster ISC rate.

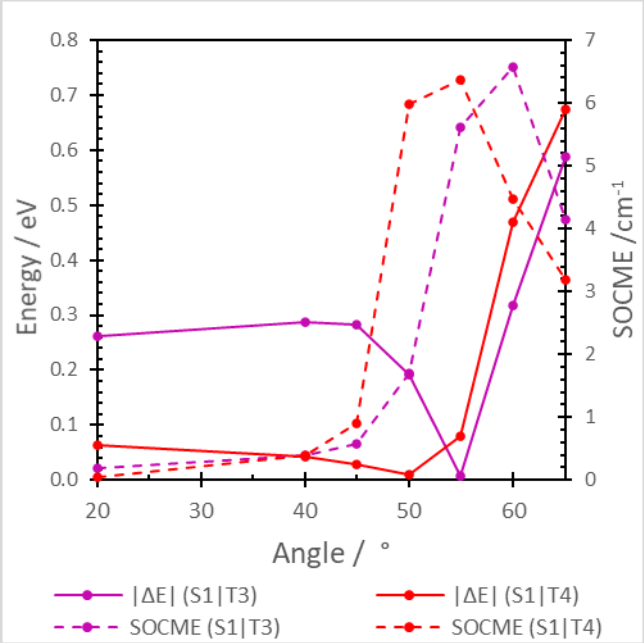


Figure 38- SOCME and the Energy difference for angle distortions C=O.

These findings corroborate the experimental data of increased ISC rate from OEP to oxochlorin and dioxochlorins. The relationship between angle displacement and energy levels can be seen in figure 39. All carbonylated samples show a decrease in energy between ground state and triplet ($T_1$) as the angle increases, explaining the reduced triplet lifetime obtained by the ns-TA for the isobacteriochlorins. As the spin-orbit coupling increases, the gap between the ground state and $T_1$ is reduced; thus, a new non-radiative channel is available. Experimental data is supported by this, as ns-TA shows a considerable decrease in lifetime for the measured triplet lifetime. 2,18-dioxoisobacteriochlorin shows a decay around 22 µs compared to 146 µs of the non-oxygenated sample.

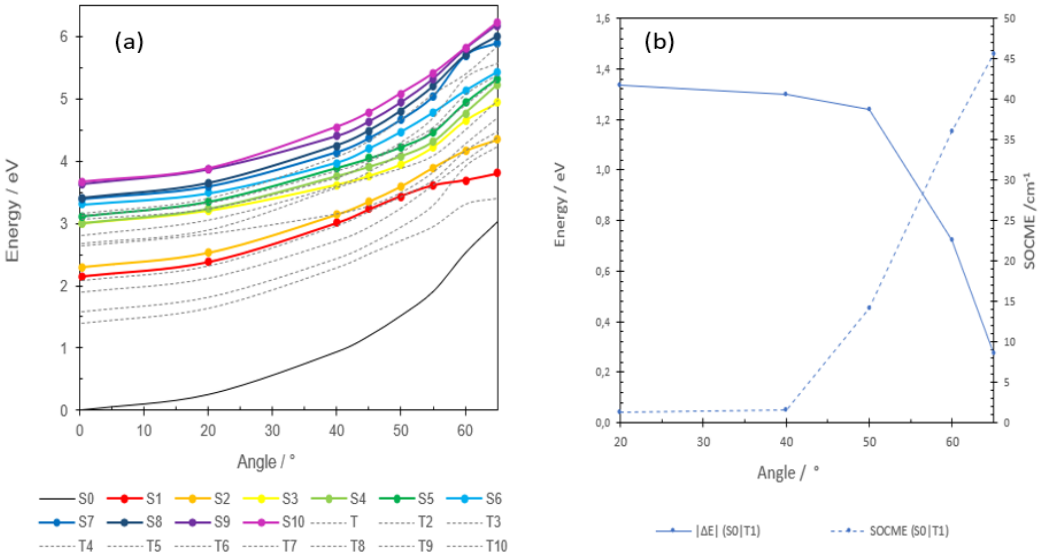


Figure 39- Left: Angle displacement C=O energy levels. Right: Angle displacement and SOCME

## Singlet-Oxygen

A direct measure of singlet oxygen formed is done by exciting the sample with a 355 nm (8-ns pulses) laser. The quantum yield of Singlet Oxygen production, $\Phi_{1_{O_2}}$It is determined by detecting the emission of singlet oxygen at 1270 nm, relative to the standard solution of perinaphthenone, both sample and standard in acetonitrile. Perinaphthenone quantum yield is referred to as 100% [72,80].

## Singlet Oxygen Data

Table 7 summarises the Singlet Oxygen quantum yield referent values to the sample. No notable trend correlates the number of carbonyl groups to the generation of singlet oxygen, but it does confirm that these samples produce singlet oxygen, ~70% to ~73% relative to the standard.

Table 7- Single Oxygen Quantum Yield

| Sample | SO QY | SO Error |
|---|---|---|
| OEP | 0.50 | 0.035 |
| 2-Oxochlorin | 0.4 | 0.015 |
| 2,13 Dioxobac. | 0.17 | 0.039 |
| 2,12-Dioxobac. | 0.15 | 0,019 |
| 2,7 Dioxoisobac. | 0.15 | 0.045 |
| 2,8 Dioxoisobac. | 0.73 | 0.28 |
| 2,18 Dioxoisobac | 0.7 | 0.12 |

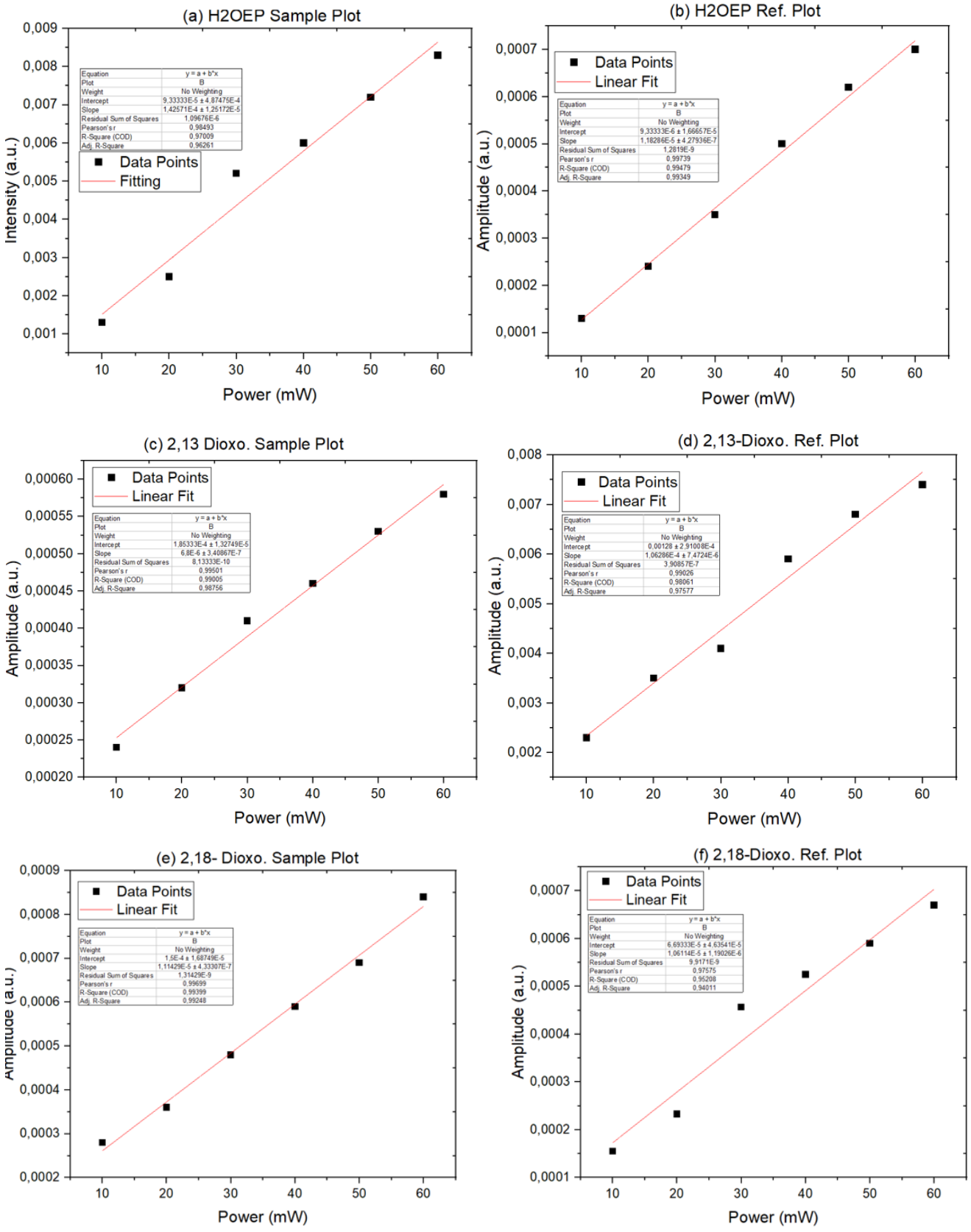


Figure 40- Sample and reference plots for singlet oxygen measurements. Top- H2OEP, Middle- 2,13-Dioxobacteriochlorin; Bottom- 2,18-Dioxoisobacteriochlorin

## Chapter Conclusion

The set of samples shows promising and interesting photophysical/chemical dynamics. The properties tunability investigation was carried out using a range of time-resolved spectroscopy and computational techniques. The effect of the isomers (tautomers) on the absorption spectra as Soret Band splitting is observed and not predicted by the theory; however, these species are. Adding the carbonyl group causes the porphyrins to deviate from the Gouterman model. This is not observed as much in 2-oxochlorin and the bacteriochlorin groups; however, it is more evident in the isobacteriochlorins. The Q bands in the absorption spectra are not clearly distinguishable in the latter, and the oscillator strength for $Q_x$ (0,0) is increased compared to the other samples. UTAS tracked the early times (femto to few nanoseconds) electron dynamics, and the number of carbonyls increased, and the lifetimes decreased. A difference in lifetime and photophysical dynamics is also noted by changing the carbonyl position, suggesting that different crossings might be available. The Qx (0,0) position also shifts, and this motion is tracked by Dr Battacharya (data not shown), revealing the coupling between excited states and solvent. TCSPC and long-time TA show the nanosecond to microsecond regime, and the same conclusion is obtained: the lifetime decreases with the increasing number of carbonyls and position change. Theoretical calculations backed up the experimental data. The increasing number of carbonyls decreases the excited energy state separation, forming new decay channels. This is true for both C-C and C-O stretching, validating the explanation of the macrocycle expansion. Dr Cardozo also found out that the angle of distortion of each carbonyl group affects the decay by affecting the spin-orbit coupling. Hence, our study has shown that porphyrins' photodynamics can be successfully tuned by modifying and adding carbonyl radicals. Although this project made advancements, there are remaining questions such as: What is the relationship between the singlet oxygen and the excited state dynamics? How do other radicals and carbonyl affect the porphyrin dynamic? To what extent the tautomers can affect the overall decay pathway?

# Chapter 5- Metal Oxide Thin Films

## Chapter Introduction

Shining light on metallic oxide films will trigger photochemical reactions that lead to several reactive oxygen species (ROS). Figure 41 schematizes the process. As previously mentioned, one possible outcome is the formation of singlet oxygen via electrons in trapped states. Holes from the valence band can form hydroxyl radicals recombining with bacteria to produce carbon dioxide and water[81]. Hole trapped states form hydroxyl radicals. ROS formation happens within a few nanoseconds, thus somewhat controllable and efficient.

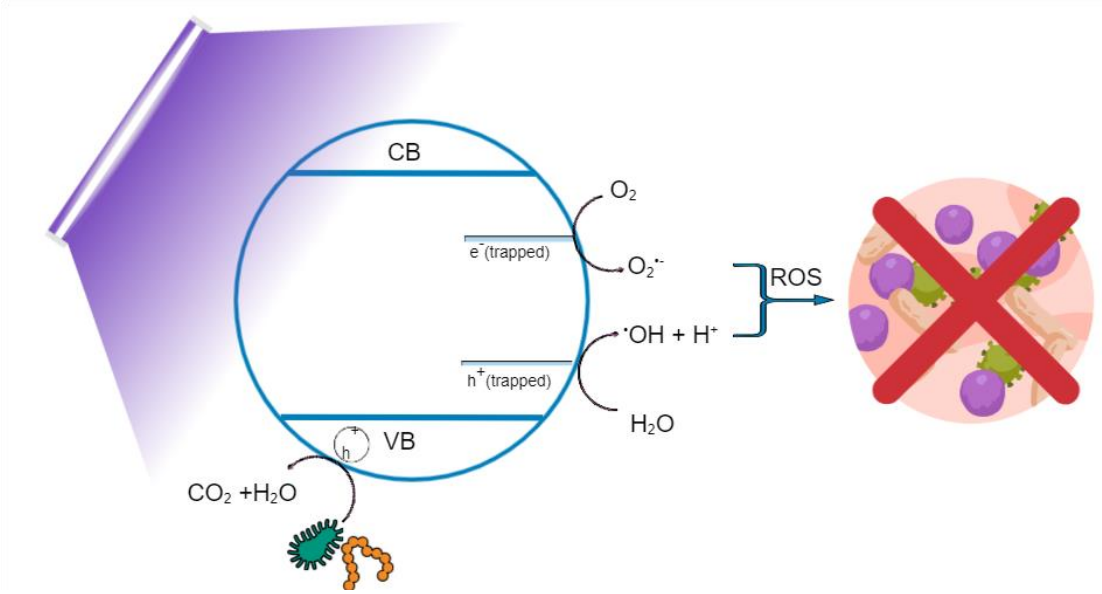


Figure 41- Light processes in metal oxide films and ROS formation

Dr Ritmi, who collaborated on this work, and synthesised the films, has widely studied the efficiency of films antibacterial properties [57,59,67,82–84]. Figure 42 shows the effectiveness of eradicating bacteria from iron and copper-based films under light irradiation. Different sputtered times are displayed ( samples 1 to 7). The films are made from low-cost and earth-abundant metals, like copper, iron and titanium. Their combination can alter the photophysical properties of the films, creating an interplay between metals. Those metals are also non-toxic, making them even more desirable in a hospital environment.

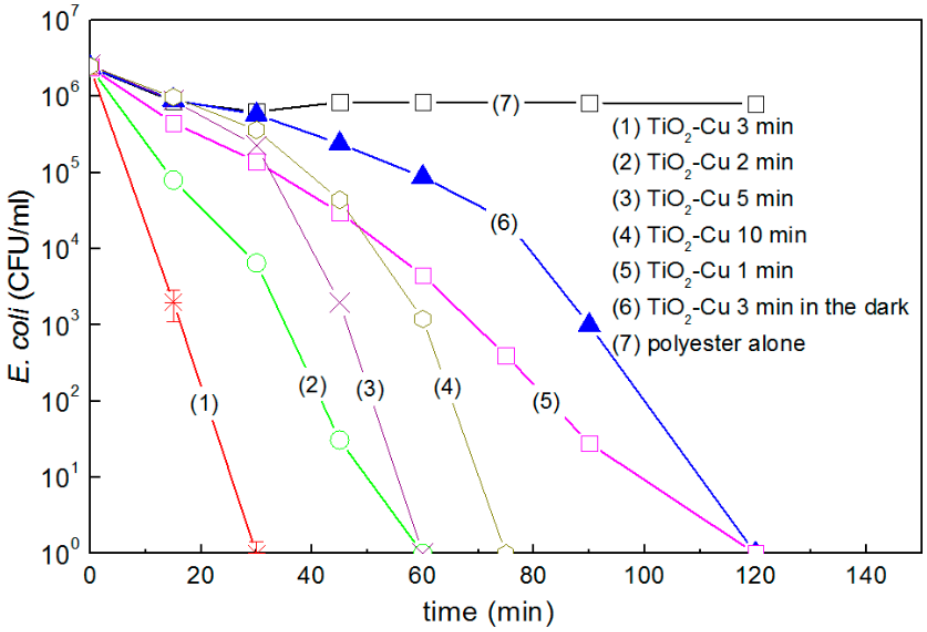


Figure 42- *E. Coli* inactivation on $TiO_2$-Cu co-sputtered for different times on PES. Adopted from [51].

The whole picture behind the mechanism is still to be understood. Some mechanisms have been proposed, such as destroying the bacterial wall via direct metal ion interaction [85] or ROS degrading the cytoplasmic membrane and the cell wall [86]. ROS is associated with oxidative stress in biomolecules and has been studied for some time. [87,88]

## Thin Films preparation

Methods are provided by Dr Rtimi, who provided the samples. High Power Impulse Magnetron Sputtering (HiPIMS) was the technique used to make the films. The method is a variation of physical vapour deposition using high voltage and shot a burst of energy focused on the target. It also uses a plasma source that ionises the material extracted by a substrate near the source. Figure 43 represents a simplified version of HiPIMS. To increase the samples' adhesion to the substrate, samples were submitted to a post-treatment with IF-Plasma.

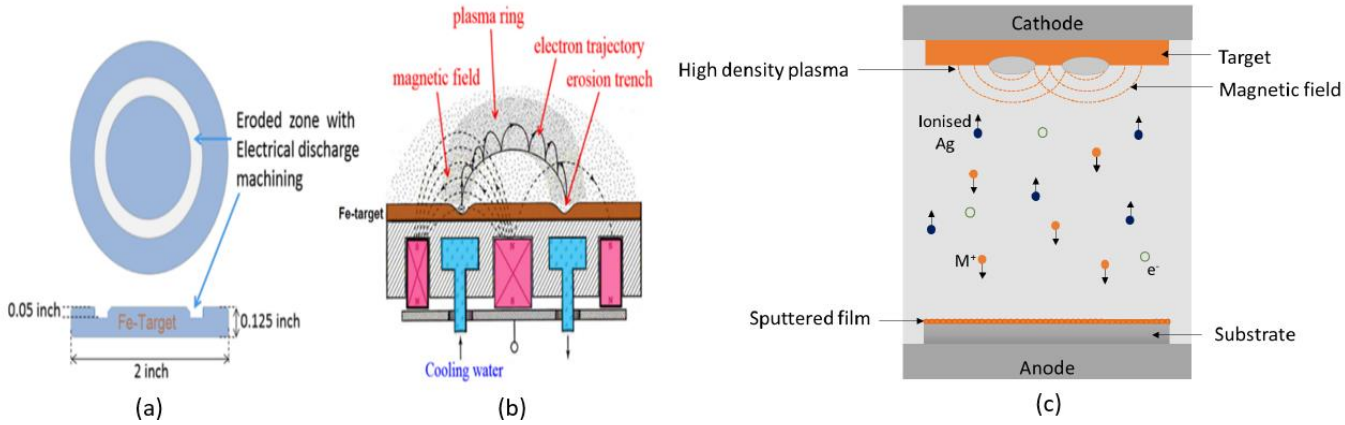


Figure 43- HiPIMS schematics. A/B) Iron target artificially modified, allowing the magnetron sputtering deposition[49] C) Technic summary [55]

## Copper/Iron samples

### XPS data

A) Survey Spectra

Initial analysis by survey spectra, figure 44, shows the atomic composition and ratio of all atoms present in the samples. All films present the expected composition, table 8, with Nitrogen's neglectable presence on the copper oxide film. Carbon makes most of the composition, meaning the substrate (PET) accounts for most of the signal. Satellite and Auger peaks were not taken into account.

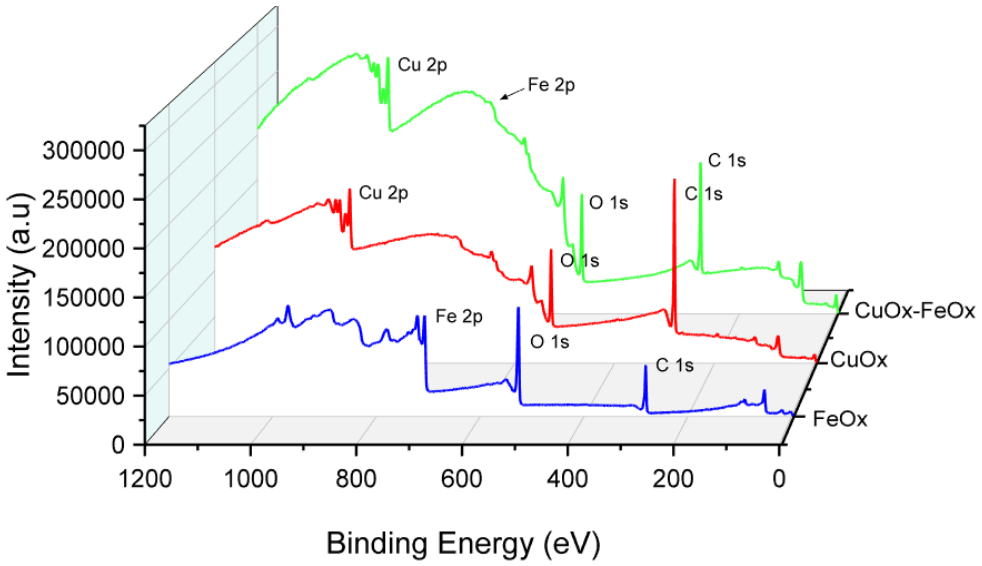


Figure 44- Survey spectra for Iron/Copper set.

Table 8- Atomic composition for Iron/Copper samples

| Film/Atomic Composition | Carbon | Oxygen | Copper | Iron | Nitrogen |
|---|---|---|---|---|---|
| FeOx | 48.69% | 46.40% | - | 4.91% | - |
| CuOx | 80.80% | 16.98% | 1.89% | - | 0.33% |
| CuOx-FeOx | 71.75% | 22.10% | 4.90% | 1.25% | - |

The amount of oxygen varies with the sample; thus, this alone is inconclusive on how much of the actual oxide is present; therefore, a more in-depth analysis of the high-resolution spectra is done and further discussed in the next section. The amalgam sample has over twice the quantity of copper as iron and might reflect the film's ultrafast dynamics. Iron Oxide sample contains the most considerable oxygen percentage, either from air exposure or sample preparation.

B.1) Copper Oxide - High-resolution spectra

Carbon 1s spectra show the contribution of three distinct peaks; binding energy values are displayed in table 9 and spectra in figure 45.

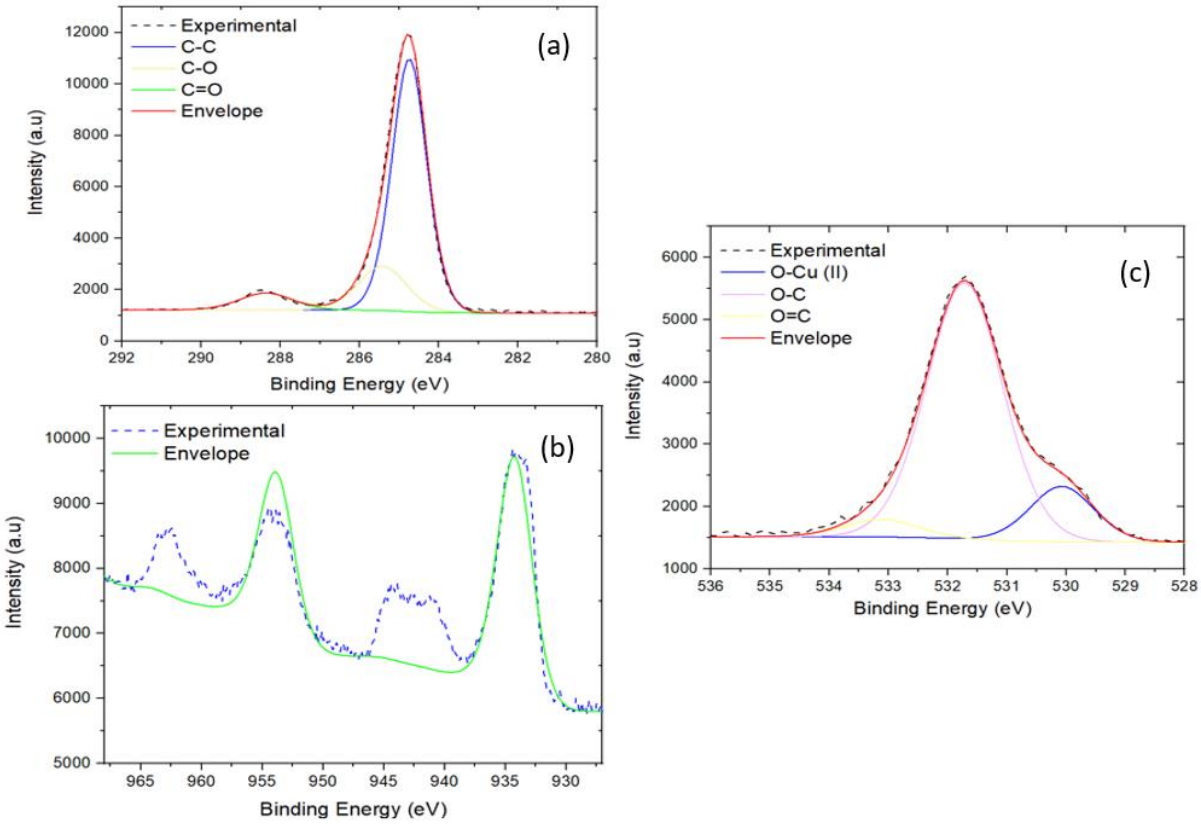


Figure 45- High-Resolution Spectra. a) C 1s spectra. b) Cu 2p spectra. c) O 1s spectra.

Carbon energies are in the region expected for the sample; a mild oxidation level due to air exposure reflects C=O as a minor band. The majority of the carbon signal comes from C-C. The lack of a C-Metal bond means that the substrate and film are linked together by oxygen only.

Table 9- Binding Energies for Carbon 1s[82]

| | C-C | C-O | C=O |
|---|---|---|---|
| Binding Energies (eV) | 284.74 | 285.5 | 288.5 |

Oxygen spectra reveal that most oxygen is bonded to carbon (as expected from the survey spectra as carbon and oxygen are present in significant quantities). Similarly, as is shown on the carbon spectra, C=O appears as a small signal. A calculator determines how much oxygen is bonded to metal, a method explained elsewhere.[89] The following table, table 10, contains the values imputed on the calculator. All values were obtained by the fitted spectras. The results

show that 1.21% of oxygen is not bound to any carbon. Comparing to the survey values of 1.89%, an almost 1:1 ratio of metal-oxygen is inferred. In other words, the amount of oxygen bonded to metal is nearly the same in quantity.

Table 10- Spreadsheet inputs acquired both from the survey and high-resolution spectra

| Peak and Result | |
|---|---|
| A) Area, Percent of Peak A,) C-C, C-H | 73.9 |
| B) Area Percent of Peak B) C-OH, C-O-C | 19.59 |
| C) Area Percent of Peak C) C=O | 6.51 |
| D) Area Percent of Peak D) O-C=O | 0 |
| E) Area Percent of Peak E) (CO3)2- | 0 |
| F) Amount of Carbon from Survey | 80.8 |
| G) Amount of Oxygen from Survey | 16.98 |

Binding energies for Oxygen are as follows:

Table 11- O1s binding energies

| | O-Cu(II) | O-C | O=C |
|---|---|---|---|
| Binding Energy (eV) | 530.07 | 531.71 | 533.13 |

The values are consistent with those available in the literature[90–93]. Cu 2p spectra satellite exhibit the expected band shape for $Cu^{2+}$ and the band position for the most intense $p_{3/2}$ peak [94–96]. Another confirmation of the CuO structure relied on the maintained distance between main peaks and satellites. Copper $2p_{3/2}$ peak is centred at 934.19 eV.

B.2) Iron Oxide – High-Resolution spectra

Carbon 1s spectra show three main bands, including C=O showing some oxidation level. The organic substrate is present in significant quantity, and there is no signal of bonding with metal. Table 12 contains the values for binding energies. Oxygen shows a majority of oxygen bound

to the metal; in contrast to the previous sample, the prevalence was O-C, which the values can further discuss in the calculator table, 13.

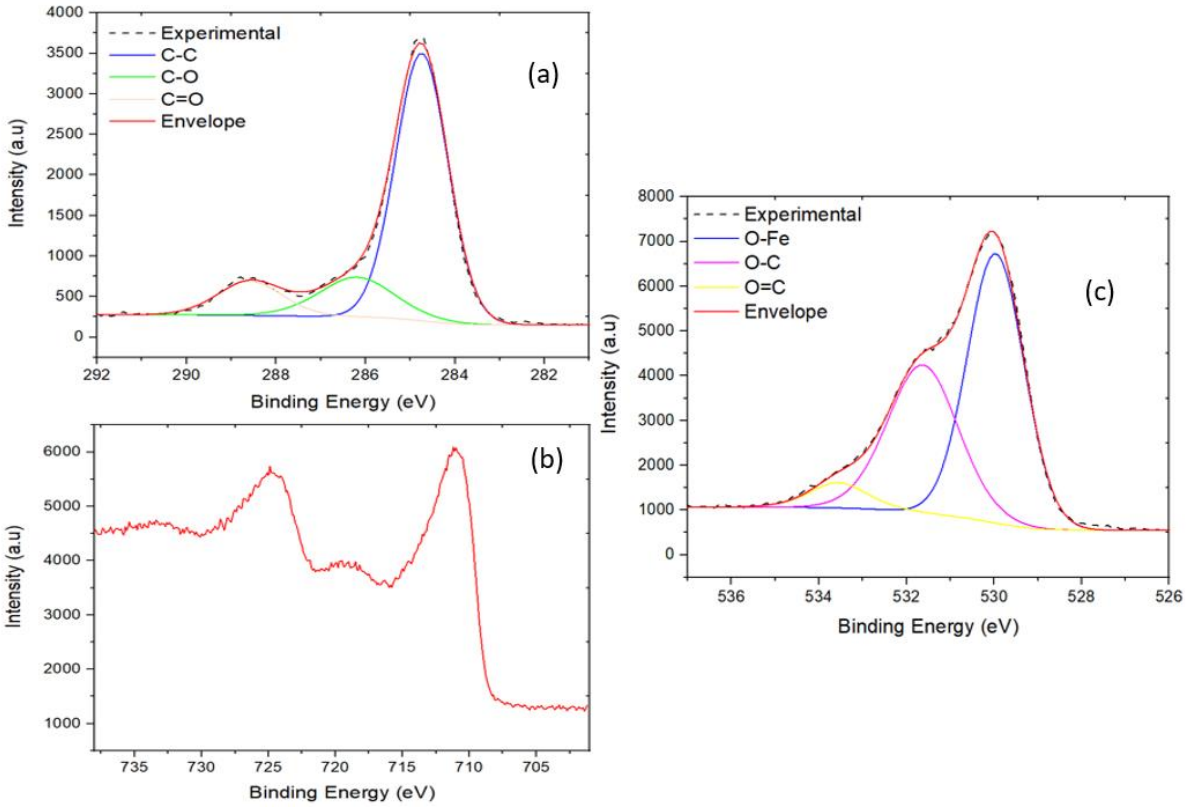


Figure 46- High-resolution spectra for Iron Oxide sample. a) C1s. b) Fe 2p. c) O1s.

Table 12- Carbon 1s binding energies.

| | C-C | C-O | C=O |
|---|---|---|---|
| Binding Energies (eV) | 284.71 | 286.19 | 288.58 |

The values in table 13 show that the C 1s composition is similar to the copper oxide sample (A, B and C). However, the remaining amount of oxygen is 33.4% which is way higher than the amount of metal found in the survey data (~5%). It is safe to assume that extra oxygen comes from surface contamination (i.e. fingerprints, oils, dust) and the sample and storage mishandling. The sample condition is not an obstruction, as it helps to simulate real-life conditions.

To determine which oxidation states and oxide composition, Fe 2p spectra is thus essential.

Table 13- Spreadsheet inputs for oxygen content – Iron oxide.

| Peak and Result | |
|---|---|
| A) Area Percent of Peak A) C-C, C-H | 64.67 |
| B) Area Percent of Peak B) C-OH, C-O-C | 25.85 |
| C) Area Percent of Peak C) C=O | 9.37 |
| D) Area Percent of Peak D) O-C=O | 0 |
| E) Area Percent of Peak E) (CO3)2- | 0 |
| F) Amount of Carbon from Survey | 48.69 |
| G) Amount of Oxygen from Survey | 46.4 |
| H) Atomic Percent (portion of Oxygen Amount from Survey) | 13.0 |
| I) Remaining Oxygen Amount from Survey | 33.4 |

The binding energy for oxygen is found in table 14.

Table 14- Binding energy for O1s

| | O-C | O=C | O-Metal |
|---|---|---|---|
| Binding Energies (eV) | 531.66 | 533.53 | 529.96 |

The main Iron peak in figure 46, located at 710 eV, contains small satellites and an intense and broad peak. This is similar to the structure of $Fe_2O_3$[97]. This structure makes sense as the quantity of oxygen is large. FeO main peak should be centred around 708 eV and has a prominent splitting, and satellites are more intense. It is not observed here; henceforth, FeO is not considered for this sample [91,98].

B.3) Copper Oxide/Iron Oxide sample

The composition of carbon species has not changed much from the other samples, either in species or quantity. Once again, no C-metal bonding is present; thus, all the metal available is bonded to oxygen. Table 15 shows the energies relative to the high-resolution spectra for carbon 1s.

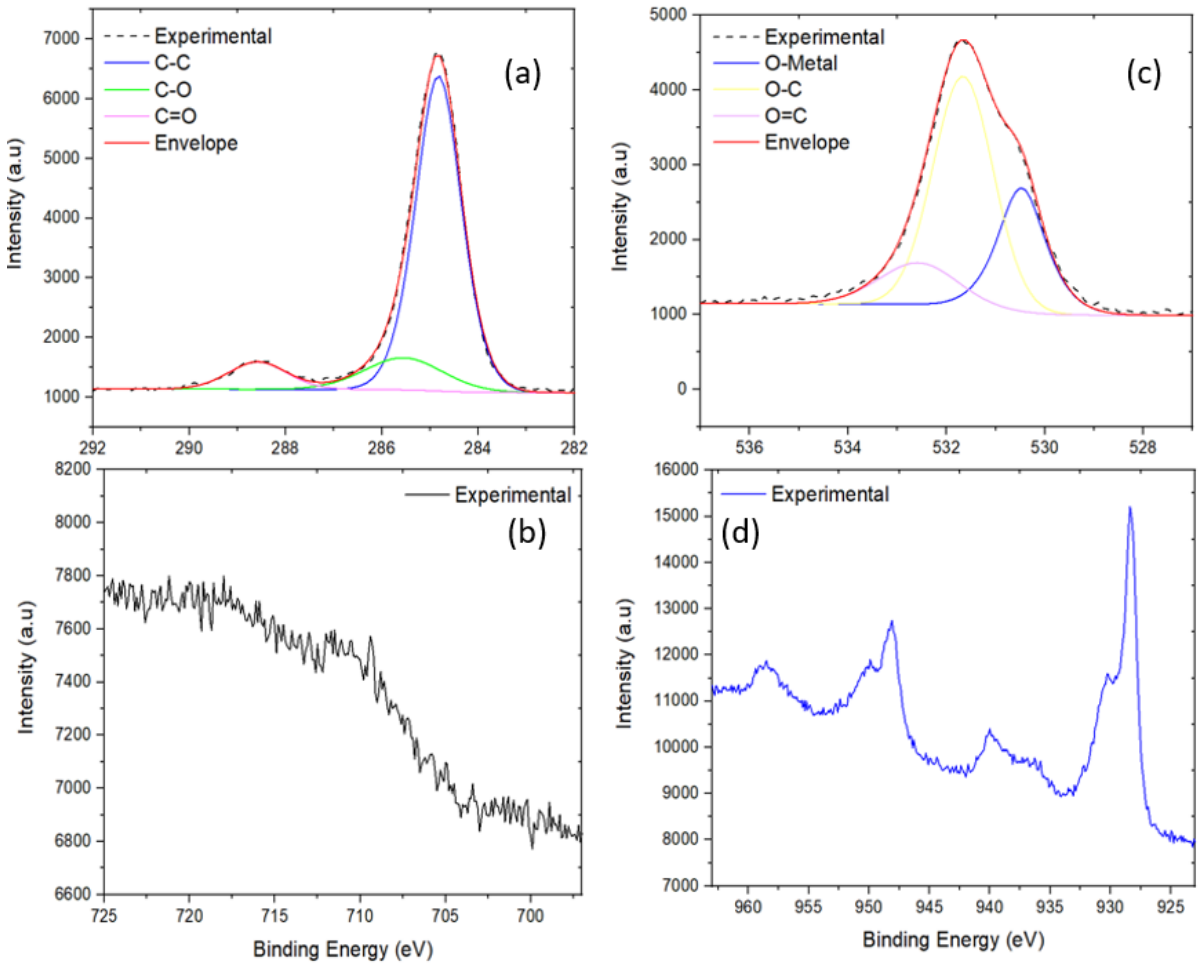


Figure 47- High-Resolution spectra. a) C1s, b) Fe 2p, c) O1s, d) Cu 2p.

Table 15- Carbon 1s and Oxygen binding energies

| | C-C | C-O | C=O |
|---|---|---|---|
| Binding Energy (eV) | 284.82 | 285.5 | 288.58 |

| | O-Metal | O-C | O=C |
|---|---|---|---|
| Binding Energy (eV) | 530.48 | 531.66 | 532.56 |

Oxygen is bonded to carbon and metal as expected, and no other contribution is seen. The energy values are also similar to what was found for the other samples. However, the metal band is much more intense than the previous samples, expected from a double oxide mix.

Table 16 contains the values used in the spreadsheet to calculate oxygen content. Carbon quantification is 73.90% C-C bonding, 17.72% for C-O, and 8.38% is the percentage of C=O bonding. The results show that 7.6% of oxygen is not bound to carbon.

The approximate sum of copper and iron is 6.15% (survey spectrum), indicating more than one oxygen atom per metal atom, but the exact rate is unknown for this case. The excess of oxygen can also be caused by sample contamination due to air exposure.

Table 16- Input values for the amalgam oxide

| Peak and Result | |
|---|---|
| A) Area Percent of Peak A) C-C, C-H | 73.9 |
| B) Area Percent of Peak B) C-OH, C-O-C | 17.72 |
| C) Area Percent of Peak C) C=O | 8.38 |
| D) Area Percent of Peak D) O-C=O | 0 |
| E) Area Percent of Peak E) (CO3)2- | 0 |
| F) Amount of Carbon from Survey | 71.75 |
| G) Amount of Oxygen from Survey | 22.1 |

Confirmed what is seen on the survey spectrum, almost no iron is found in the copper oxide/iron oxide sample, as the spectrum lacks the main features and is a lot noisy, especially compared to the pure iron oxide sample. Interestingly, an extra shoulder is observed in the copper spectra and a reduction at parts of the satellite. It confirms that copper has a mix of oxidation states, Cu(II) and Cu (I). This is likely the result either of laser exposition or plasma treatment effects when the films were made.

## Steady-State and Time-Resolved Spectroscopy

All thin films exhibit a very low absorption in the visible spectral regime, as shown in Figure 48. The mixed film has the most intense spectra. The XPS shows that those films have carbon and oxygen quantities higher than anticipated, suggesting contamination by fingerprints, dust, and oils. These factors might reflect on the intensity of the signal and a more precise interpretation of the signals.

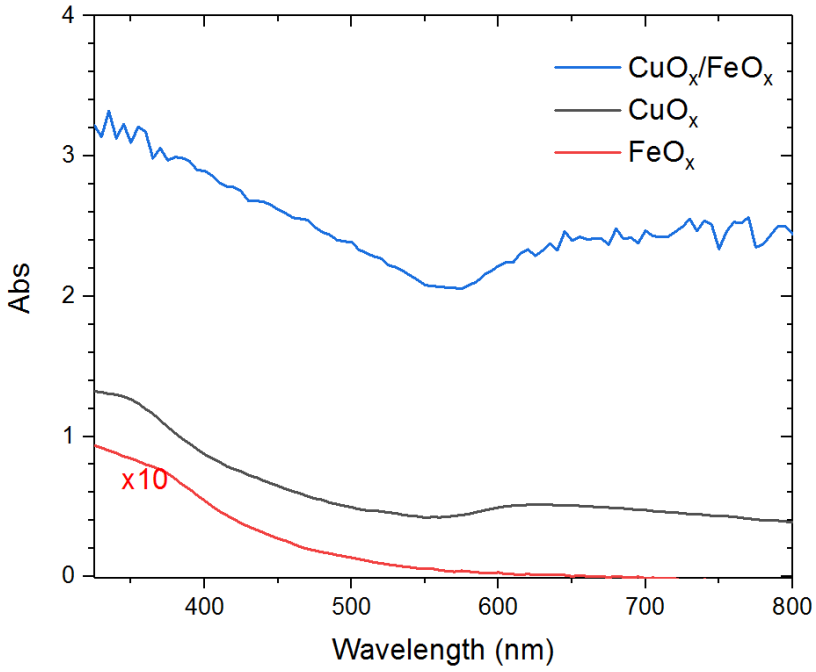


Figure 48- Steady-state absorption for the films

Metal atoms absorption is highly related to d-d forbidden transitions (Ligand Field), which causes the broad band before 400nm. Furthermore, absorption spectra bands and overall absorption are associated with the direct interaction between metal and ligand. In this case, the oxygen causes a LMCT with the interaction between not filled d orbitals from oxygen's metal and p orbitals. These will reflect in the bandgap and the intensity of hole and electron formation, transition probability, and trapped states existence. In a 3-dimensional metal oxide unit cell, the approximation of structures can generate a magnetic dependence between metallic atoms, causing simultaneous pair electronic[6782].

Transient absorption data can be fitted with a bi-exponential function and possess one picosecond component and one non-decaying (within the experiment time window) represented by the long microsecond component. Minimal changes are observed at later times. A unique constant can be used to fit the data correctly, suggesting that all processes (HA, EA, GSB and SE) occur within the same timescale (Figure 49). A long-lived state represents trapped electronic states described (non-decaying signal at the kinetic profile and population spectra[102] ) and smaller components summarized into a charge recombination state between holes and electrons. As transient data indicate in figure 49, a slight shift is observed in the first few picoseconds at early times, suggesting the presence of multiple electronic states. Thus,

recombining these multiple states is possible since they are very close to each other in energy since the charge recombination of HA and EA is most probable. Theoretical calculations must address this solid-state's correct relaxation pathway and cooling system.

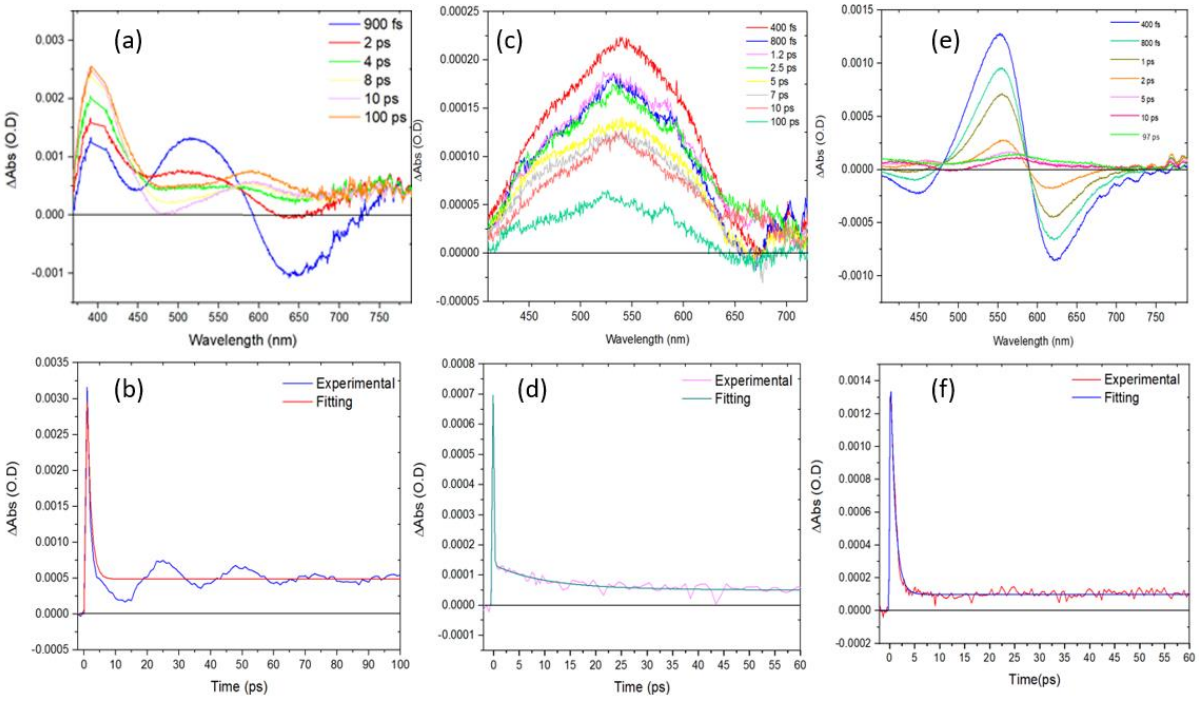


Figure 49- Transient absorption top and respective kinetic traces (bottom) a/b) copper oxide, c/d) iron oxide, e/f) copper-iron oxide

Table 17- Time constants for the copper/iron oxide films

| Sample | τ1 (ps) | τ2 (ps) |
|---|---|---|
| Copper Oxide | 1.2 | non-decaying |
| Iron Oxide | 9.7 | 5000 |
| Copper/Iron Oxide | 0.9 | non-decaying |

Electron and hole recombination is expected to occur within the first few hundred femtoseconds (as mentioned in previous chapters); thus, it is assumed that τ1 corresponds to this process. The long component needed to fit the spectra's kinetic tail is associated with the trapped stated or intergap states caused by the metal coupling in the oxides. Singlet oxygen forms within a few microseconds, in this case, would correspond to a long-lived signal into femtosecond TA. [57,72].

The oscillations presented on the kinetic profile can be associated with the lattice rigidity[57,99,100], suggesting that the copper oxide is less rigid. The iron oxide lifetime is expected for the hematite group [101]. Compared to the other samples, the mixed oxide has a shorter component as $\tau_1$, whilst maintaining the non-decaying component.

The oscillatory pattern extracted from the films is fitted using equation 41. The data was extracted from the original data set by subtracting the SVD fit. The residual 2D matrix and procedure details can be found elsewhere[102]. For the total transient signal amplitude, the oscillations and relative amplitude are unaffected by the pump power and are thus intrinsic to the metallic film. The time-dependent, *t*, oscillatory signal is modelled for each wavelength ($\lambda$) as a single damped sine wave following the equation where a is the amplitude, $\tau$ is the time constant of the envelope (damping), f is the frequency, and $\varphi$ is the phase of the oscillation.

$$\Delta A(\lambda) = ae^{(-t/\tau)} \sin\left(\frac{2\pi t}{f} + \varphi\right) \qquad \text{(eq. 41)}$$

The fitting is displayed in figure 50. From 440 to 560 nm, the oscillations mean frequency is about 40.0 GHz. This value matches a longitudinal acoustic phonon[22,100,103].

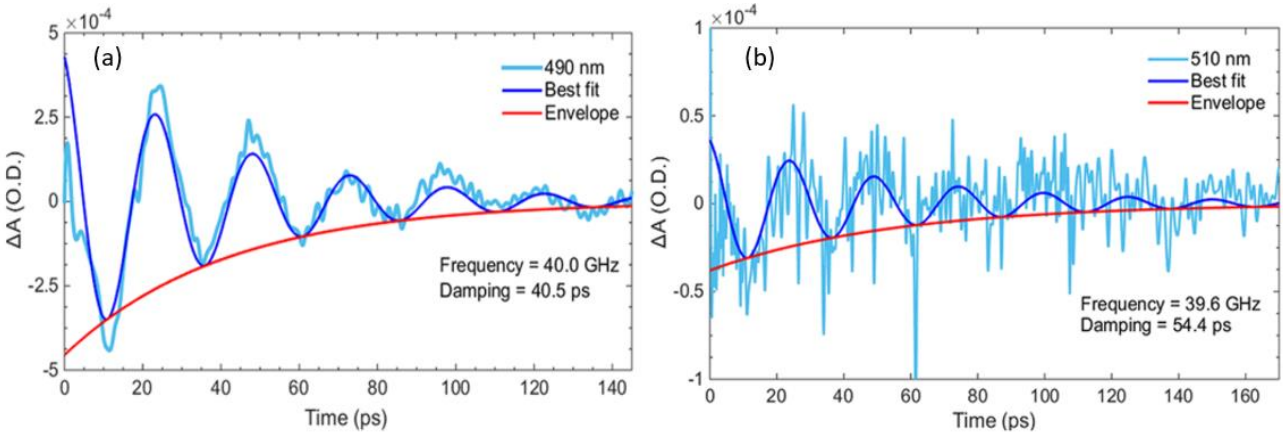


Figure 50- Fitted oscillations for (a) Copper Oxide and (b) Copper-Iron oxide. Taken from [57].

Photoinduced acoustic phonons imply a strong coupling between the electronic and lattice effects. These oscillations' frequency corresponds to those monitored in vanadium oxide thin films while in their metallic phases. It was shown that frequencies below 10 GHz.[103] mark the

insulating character of vanadium oxides. Hence, the 40.0 GHz in $Cu_xO$ could be a marker of its metallic character. Joly et al. correlated these phenomena to the material thickness. The kinetic profile for the iron and mixed oxides show weak oscillations. They range from 460 to 550 nm with maximum amplitude at 510 nm and a mean frequency and average damping constant of 39.6 GHz and 54.6 ps. The oscillation frequency and damping are similar to the CuxO film.

## Bacterial Inactivation (performed by Dr Rtimi)

Figure 51 (a) elucidates the efficiency of the sputtered films' antibacterial properties against *E. Coli*. As expected, the interaction between the two metals makes the chemical reaction more efficient. Thus double oxide film is the most efficient in killing bacteria two and three times faster than copper and iron stand-alone films. Meanwhile, figure 51 (b) shows the inactivation of different *E.Coli* exposed to indoor light in the presence of the mixed film.

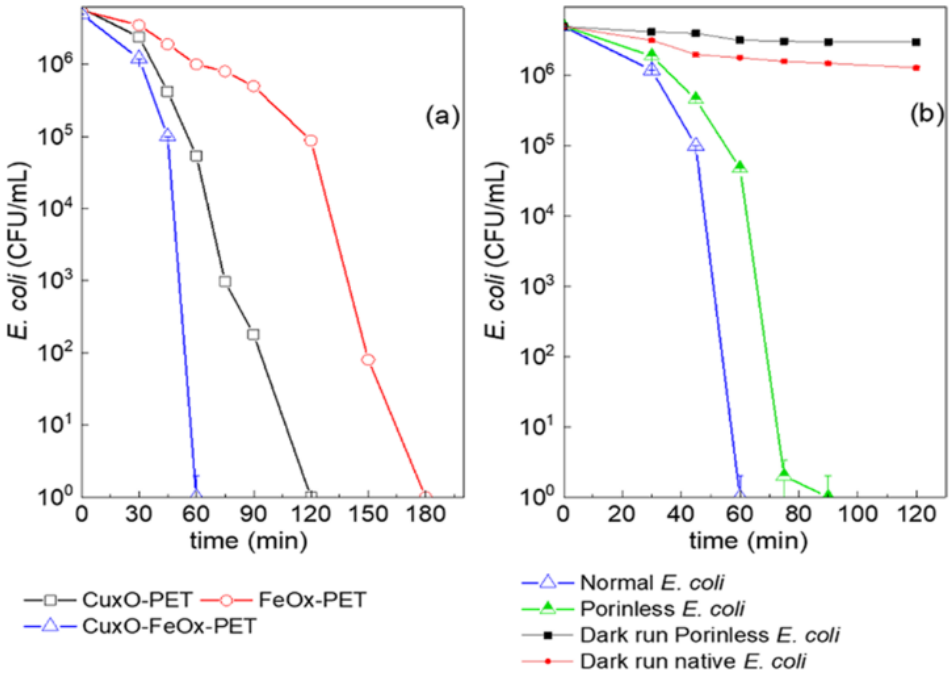


Figure 51- *E. Coli* inactivation. (a) films comparison, (b) types of *E.Coli* and Copper-Iron oxide film. Taken from [57]

Using genetically modified bacteria (porinless) allows differentiating between intracellular and extracellular inactivation mechanisms. Inactivation tests both in light and dark conditions (figure 51 (b)) of both types of bacteria are comparable, meaning ions and oxygen radicals

mainly act outside the cells. The photoproducts then potentially affect any living organism in its surroundings. As the samples release ions, the toxicity is less in this case, and the quantification was monitored by inductively coupled plasma mass spectrometry. Iron and copper released (µg/L) from the sputtered CuOx-FeOx-PET sample were 4 and 6 ppb, respectively. These levels are far below the allowed toxicity levels fixed by the regulation for water and health (around 1mg/L)[104,105].

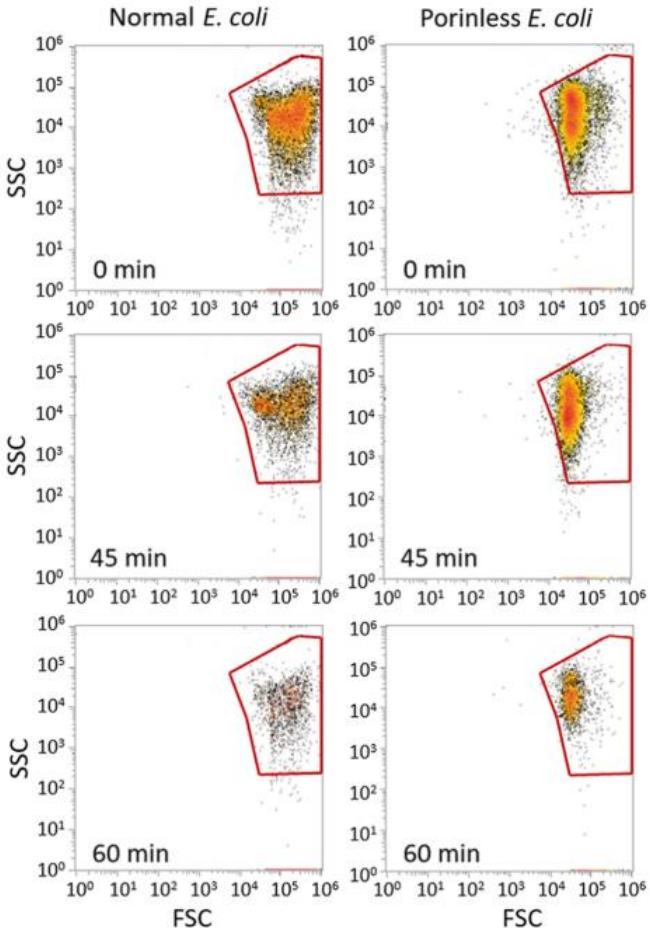


Figure 52- Flow cytometry for normal and modified *E.Coli*.

Flow cytometry helps understand the role of metallic films in the deactivation mechanism. Figure 52: Graf et al. show that two mechanisms take place. Inactivation happens as an external and minor effect of the metal ions. The latter points to a unique mechanism that rapidly degrades the cell debris. The tiny cell concentration observed after 60 min photocatalysis on the sputtered CuOx-FeOx-PET was around 102 CFU/mL. It coincides with the plate count agar

method's detection limit and corresponds to the tolerable bacterial concentration in hospital settings.[23,82,106]

## Copper/Titanium samples

### XPS Data

Differently from the other sample set, the data in this section will be presented differently. The surveys for the four samples are shown in figure 53. To better view the survey spectra, they are separated by sample, and so are the tables.

Copper and Iron Oxides present the expected carbon appearance from the substrate/dust/oils (i.e. hand oil and fingerprints). Graphs c/d confirm the proportion between metal atoms in the films. Mixed films reflect the metal composition directly; thus, copper satellites are more intense (d).

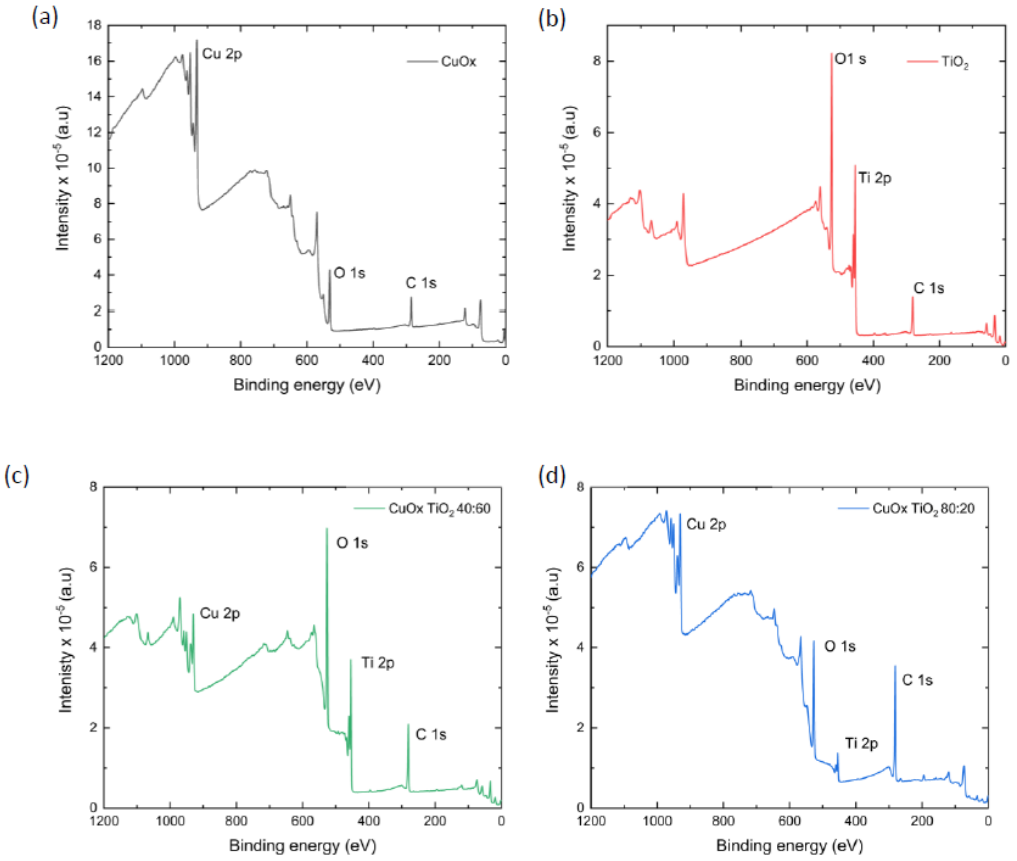


Figure 53- Survey spectra for all four films

A) Metal Oxide films

Data from the survey, table 18, reveals the atomic percentage for each atom, where the copper oxide has more than half of its carbon composition, whereas titanium oxide has almost half of its composition of oxygen atoms.

Table 18- Atomic percentage of pure copper/titanium films

| Atomic Composition (%) | Carbon | Metal | Oxygen |
|---|---|---|---|
| CuOx | 51.78 | 16.87 | 31.35 |
| TiO2 | 29.35 | 20.77 | 48.71 |

The polymer-based substrate explains the prominent presence of carbon, and all other carbon sources likely come from external contamination. Analysis of the high-resolution spectra shows a further oxidation level for the copper oxide sample in the carbon spectra (figure 54. These samples were exposed to an adhesion post-treatment, which can break and form new bonds within the lattice components. A direct link between substrate and metal is unusual and indicates how the treatment affects the film. On the other hand, titanium oxide does not exhibit O-C=O or C-metal bondings, suggesting being more resistant than copper oxide.

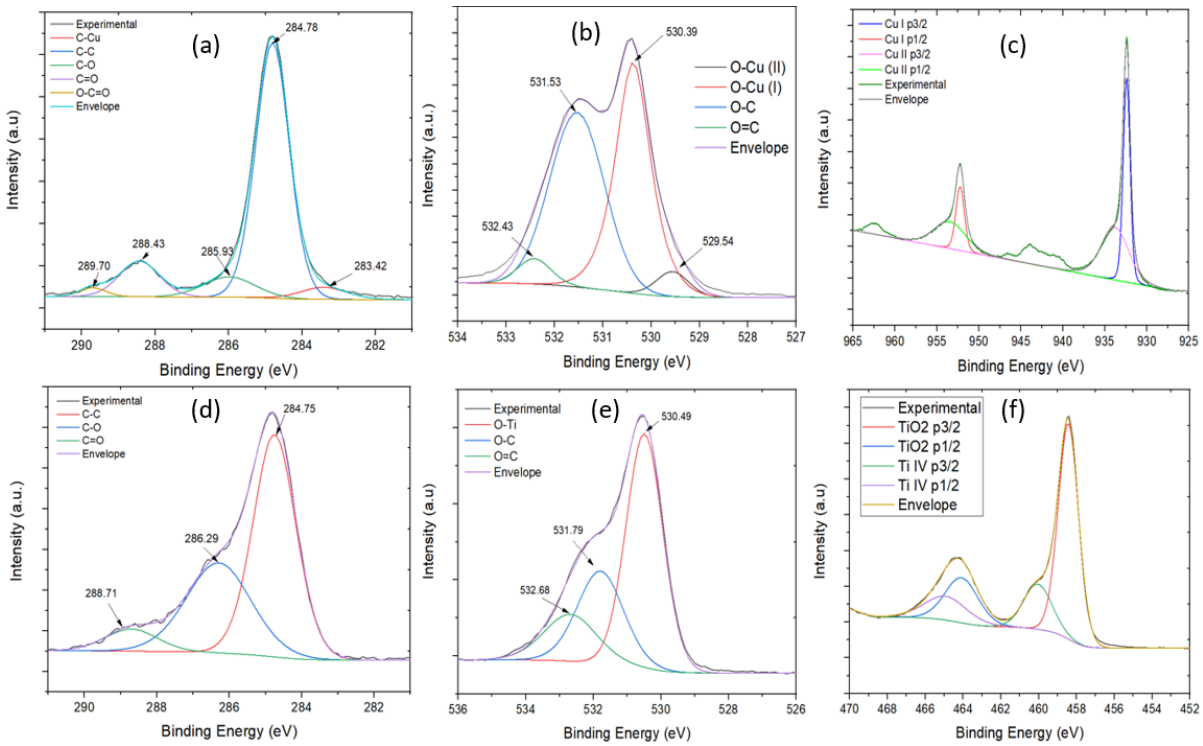


Figure 54- Top: Copper Oxide, Bottom: Titanium Oxide. Carbon 1s, Oxygen 1s, and Metal 2p, respectively, left to right.

Oxygen 1s spectra indicate the metal oxidation state and different oxidation forms of copper, Cu (II) and Cu (I). The presence of copper I reflect the plasma treatment, and the film is less resistant to the plasma than that of titanium. The high-resolution metal spectra also confirm those oxidation states. The titanium also shows a mixture of oxidation states, as observed on the high-resolution metal spectra (figure 54). Copper I and Titanium IV are present in larger quantities, suggesting that the treatment did not affect the film's titanium composition (i.e. larger quantities of the oxidized state); Titanium III is a minor impurity. Copper seems more susceptible to the treatment, as copper I is more present than copper II. The percentage of oxygen not bound to carbon is calculated as previously described for the other samples. Titanium bands (458.43 eV for 2p3/2, Ti IV. 460.04 eV for 2p3/2 for Ti III) position are in concordance with the literature. [97,107,108]

Table 19- Spreadsheet values for Copper oxide film

| Peak and Result | |
|---|---|
| A) Area Percent of Peak A) C-C, C-H | 72.45 |
| B) Area Percent of Peak B) C-OH, C-O-C | 8.84 |

| | |
|---|---|
| C) Area Percent of Peak C) C=O | 12.03 |
| D) Area Percent of Peak D) O-C=O | 1.98 |
| E) Area Percent of Peak E) (CO3)2- | 4.7 |
| F) Amount of Carbon from Survey | 51.84 |
| G) Amount of Oxygen from Survey | 31.39 |
| H) Atomic Percent (portion of Oxygen Amount from Survey) | 17.8 |
| I) Remaining Oxygen Amount from Survey | 13.6 |
| J) Percentage of Total Oxygen from Carbon Species | 56.7 |

Table 20- Spreadsheet values for Titanium oxide

| Peak and Result | |
|---|---|
| A) Area Percent of Peak A) C-C, C-H | 57.66 |
| B) Area Percent of Peak B) C-OH, C-O-C | 35.38 |
| C) Area Percent of Peak C) C=O | 6.97 |
| D) Area Percent of Peak D) O-C=O | 0 |
| E) Area Percent of Peak E) (CO3)2- | 0 |
| F) Amount of Carbon from Survey | 29.35 |
| G) Amount of Oxygen from Survey | 48.71 |
| H) Atomic Percent (portion of Oxygen Amount from Survey) | 9 |
| I) Remaining Oxygen Amount from Survey | 39.7 |
| J) Percentage of Total Oxygen from Carbon Species | 18.4 |

Oxygen high-resolution (figure 54) infers that most atoms are bonded to titanium. Table 19 shows 13.6% of the remaining oxygen, corresponding to almost a 1:1 proportion between oxygen and metal. The remaining oxygen is shared between different copper oxidation states, and the excess metal is thus bonded to carbon, as shown on the carbon spectrum. Table 20 presents almost ~40% of the oxygen that is not bound to carbon, whereas survey spectra show

~20% of metal composition. Thus the proportion is close to 1:2 between oxygen and metal atoms.

B) Mixed Oxide Films

Two films are being studied in this section, one containing copper in the majority (20% titanium, 80% copper) and the other with titanium as the main composition (40% copper, 60% titanium). Data retrieved from the survey (figure53) is compiled in Tables 21 and 22.

Considering only the metal composition, the proportion is close to 80/20. Carbon counts as the majority; they are followed by oxygen, whereas titanium has a bit more than 2%, as shown in the survey spectra. A similar trend is observed for the following sample, most carbon and oxygen. The metal proportion follows the label, 40% of copper and 60% of titanium.

Table 21- Atomic composition for Mixed Oxide (80/20)

| Atomic Composition (%) | Carbon | Oxygen | Copper | Titanium |
|---|---|---|---|---|
| CuOx-TiO2 (80/20) | 63.62 | 26.78 | 7.37 | 2.23 |
| Metals Only | - | - | 76.74 | 23.26 |

Table 22- Atomic composition for Mixed Oxide (60/40)

| Atomic Composition (%) | Carbon | Oxygen | Copper | Titanium |
|---|---|---|---|---|
| TiO2-CuOx 60/40 | 44.67 | 34.13 | 8.75 | 12.45 |
| Metals Only | - | - | 41.27 | 58.73 |

Figure 55 contains the high-resolution spectra for the (80/20) mixed sample. Carbon distribution shows three contributions, likely from the PET substrate in the form of C-C bonding. C-O/C=O are also present, linking substrate to the oxides and coming from possible contaminations. Oxygen high-resolution (figure 55) shows two contributions attributed to metal bonds and carbon. Similar to the previous samples, copper 2p indicates two distinct oxidation states. Most of the copper is found in a Cu (II) state, with minor traces of copper (I).

Titanium could be fitted with a single band (2p1/2 not fitted), indicating a single oxidation state for the atom. Multiple copper oxidation states suggest that the post-treatments influence the sample, similar to the previous sample. Unlike the other copper sample, most of the sample is comprised of CuO. Once again, Titanium III appear as minor contamination.

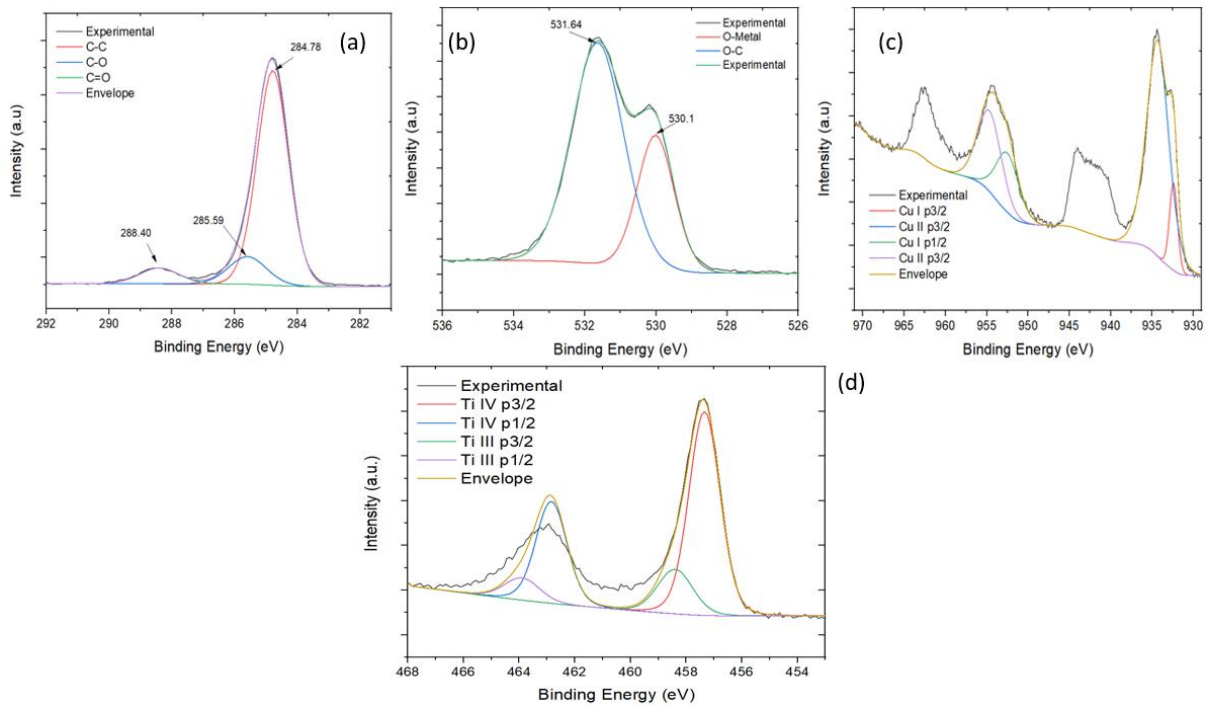


Figure 55- High-resolution spectra for CuOx-TiOx (80/20) a) C 1s, b) O 1s, c) Cu 2p, d) Ti2p

The (40/60) sample has similar carbon and oxygen high-resolution spectra, with the only significant difference being the band size in the oxygen spectra. Sample (20/80) has more O-C contribution, whereas this sample contains a more considerable O-Metal contribution. Copper II appears as a majority of the copper atoms, and copper I as minor traces. Titanium shows little difference from the first amalgam.

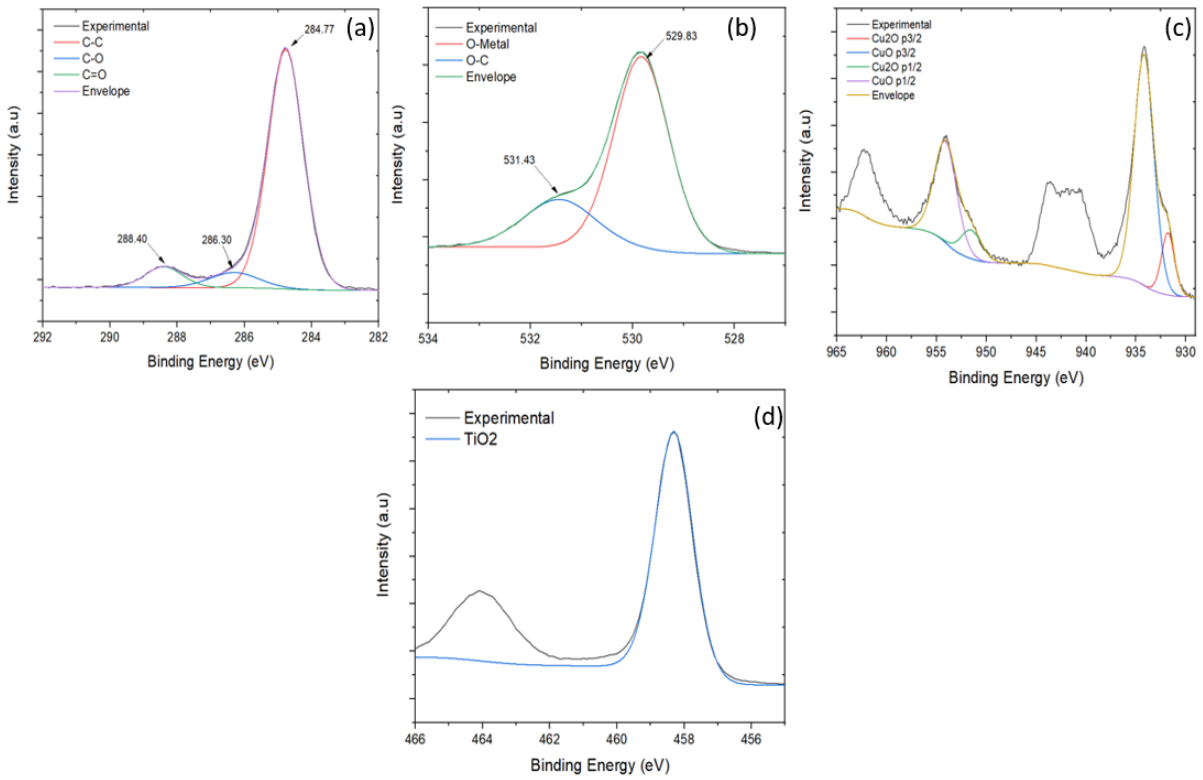


Figure 56- High-resolution spectra for CuOx-TiOx (40/60). a) C 1s, b) O 1s, c) Cu 2p, d) Ti 2p

## Steady State Absorption for Copper oxide/Titanium oxide samples (Chloe B. Powell - data acquisition and analysis)

The absorption profiles were acquired by reflectance and are plotted in figure 57. Metal oxides have a few absorption spectra contributions, such as d-d transitions and charge transfer from oxygen to metal.

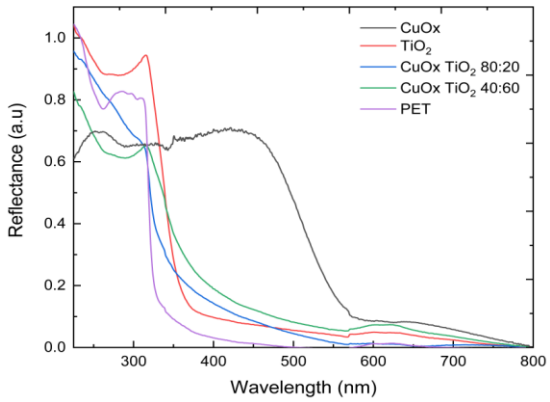


Figure 57- Reflectance of the films. Adopted from [55]

The copper oxide shows broad and robust absorption across the visible region, with Cu (I) and Cu (II) contributions (valence to unoccupied conduction band)[109]. All other samples have PET as the main signal, with minor shifts and variations due to the presence of the metal oxides (more pronounced in the 320nm-500nm region). PET signal around 350nm comes from the single electron from HOMO to LUMO[110,111]. The small shift is closely related to the bandgap value; in this case, copper-titanium films possess higher absorption in the visible region when compared to pure titanium oxide films. Including the narrow bandgap of copper oxide heavily affects the system overall properties, tuning the absorption profile[112]. According to Zuo et al. [113], the number of oxygen vacancies increases as the ratio Cu: Ti increases, resulting in the redshift. As shown by the XPS (figures 53,55, and 56), both oxides presence interfered with the individual oxides' properties, now displayed as bands shift on the absorption spectra.

### Time-Resolved Spectroscopy (performed by Chloe Powell and Dr Sayantan B. )

Transient absorption spectroscopy tracks the excited state dynamics upon excitation of the films using 350 nm light. Figure 59 shows TA spectra for CuOx and TiO2; most signals arrive from HA and EA. The valence band of copper oxide is composed of 2p oxygen and 3d copper orbitals. Copper oxides spectra show strong transient at early times, between 475-615 nm, and bleaches around 400-475 nm and 615-700nm. Within 5ps, the transient decay forms a new state, as seen at a delay of 50.9 ps.

Titanium oxide at early times shows strong transient around 588 nm, which gradually decays to a different state but is not observed in the present timescale (up to a few nanoseconds). The

intensity of the positive signal overcomes negative signals, suggesting that HA and EA are more prominent than GSB and SE.

PET exhibit a similar trend with intense signal overcoming the negative bleaches across the whole spectral window. Table 23 contains the lifetime values used to fit the data.

Table 23- Lifetimevalule for the double oxide films

| Sample | τ1 (ps) | τ2 (ps) | τ3 (ps) | τ4 (ps) |
|---|---|---|---|---|
| Copper Oxide | 0.57 | 5.8 | 466 | long-lived |
| Titanium Oxide | >0.1 | 29.4 | 821 | long-lived |
| PET | >0.1 | 7.9 | 946 | long-lived |
| Copper-Titanium (80/20) | 0.42 | 20.8 | 671 | long-lived |
| Copper-Titanium (40/60) | 0.12 | 7.8 | 626 | long-lived |

The first kinetic component for all films are relatively close to each other, with copper oxide slightly slower than the other samples. The (40/60) composite on the second and third components shows a faster dynamic than the others, whereas titanium oxide is the slowest in the second and third components. None of the samples relaxed within an ns time range; thus, long-time TA was performed to analyse the long-range time window.

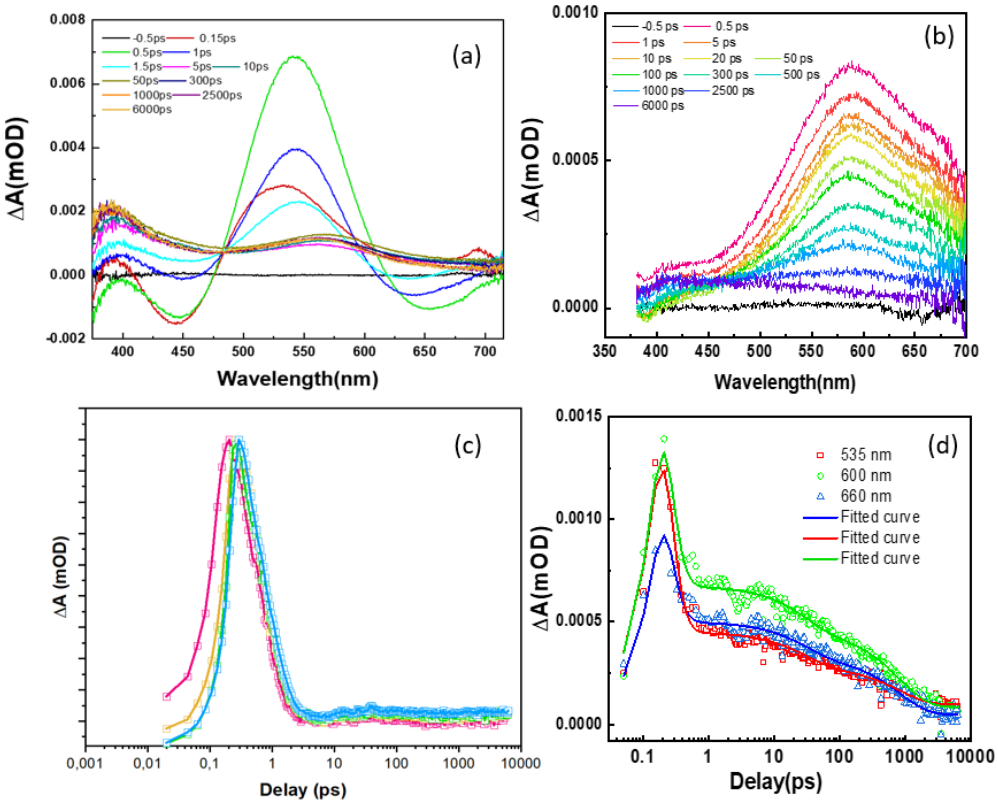


Figure 58- TA spectra for (a) $CuO_x$ and (b) $TiO_2$ and respective kinetics (c, d).

In figure 60, TA spectra for the mixed nanocomposites and PET. Upon titanium's addition, the spectra shape shown for (80/20) shifts to longer wavelengths compared to pure copper oxide. Not surprisingly, the spectra for (40/60) follow the same pattern. All negative features present on (80/20) are engulfed by the intensity of the positive absorption band. On the other hand (40/60) shows a bleach around 400 nm up to 450 nm. Kinetic spectra for both (20/80) and PET do not show many changes in shape and do not fully decay within the time window.

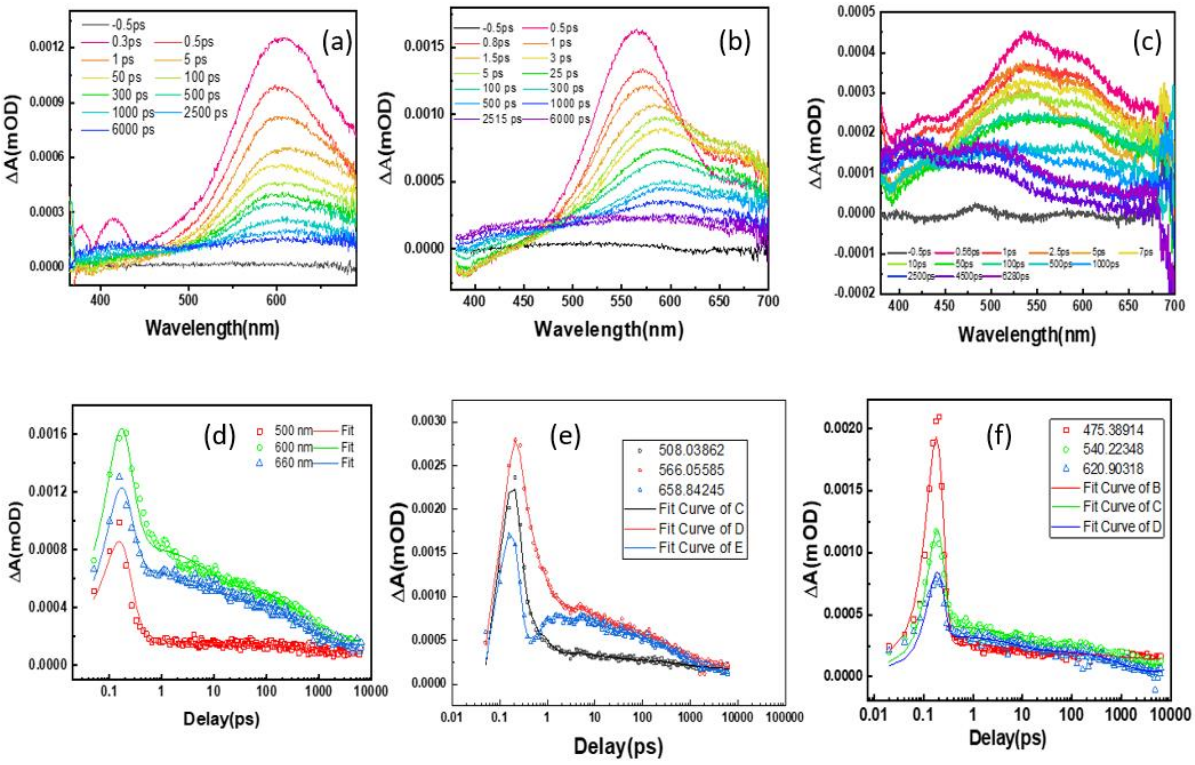


Figure 59- TA Spectra. a,b,c: Copper-Titanium (80/20), Copper-Titanium (40/60), PET. d,e,f: respective kinetic traces.

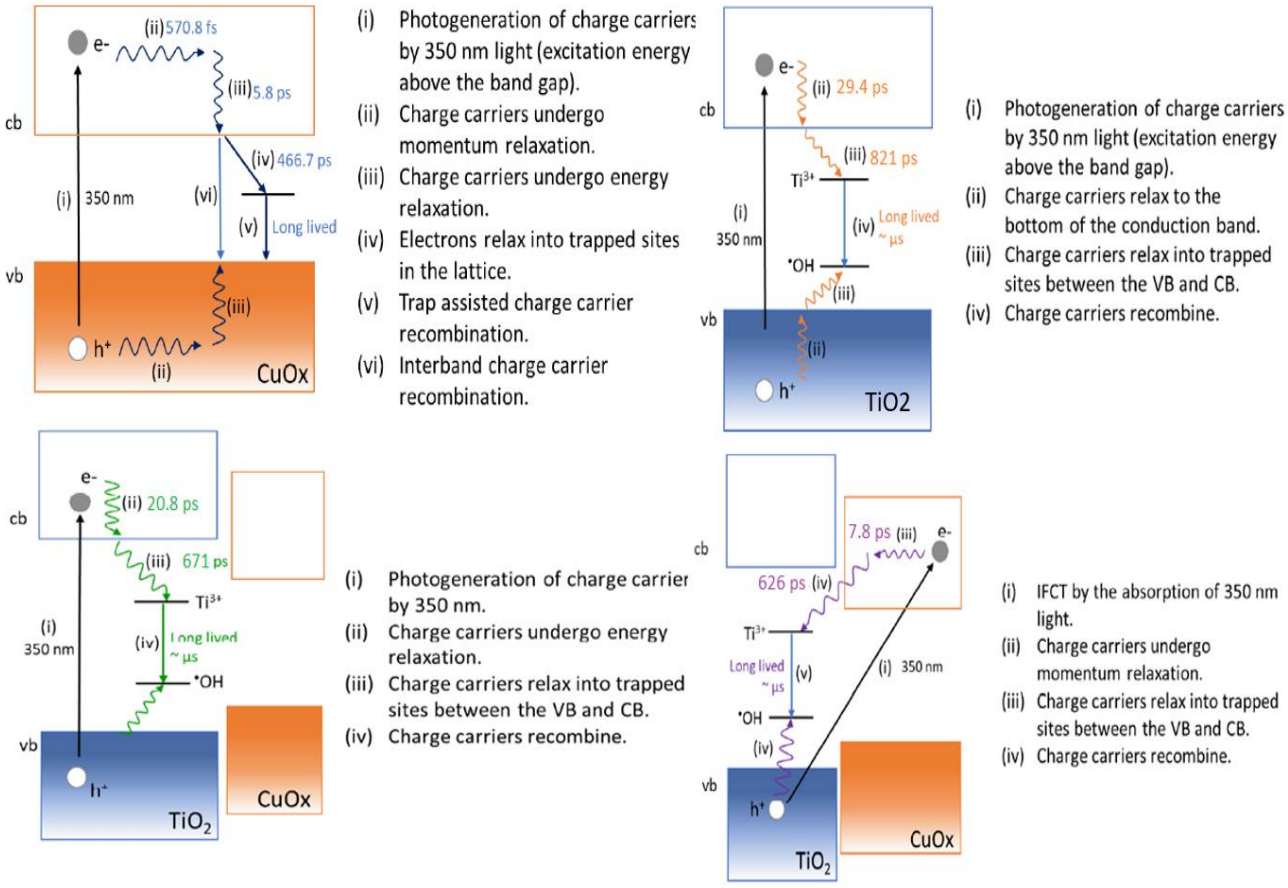


Figure 60- Proposed decay mechanism for the films. Lifetimes were taken from table 23. Taken from [55]

A decay mechanism is proposed and elucidated in figure 61. Exciting the films above the bandgap generates electrons and holes, which start decaying within the first few picoseconds. A rapid decrease in transient absorption can be attributed to carrier relaxation, similar to the previous samples. The case is the same for $CuO_x$ and $TiO_2$ but slightly different for the mixed composition sample. The movement of electrons and holes inside the bands, which happens within the first few fs, is represented by the first time constant, whereas the second should represent the electron-hole recombination as the charges move to the band's border. The (iii) step for copper oxide and titanium oxide films relates to the carrier trapping happening in the later ps timescale, and the final step should be the formation of ROS, which lies in a timescale bigger than the one shown.

Chloe et al.[64] suggested the mechanism based on the transient absorption spectra, which comprises absorption bands corresponding to ESA in CuOx and the HA of TiO2. In the case of CuOx: TiO2 (80/20), holes and electrons relax to the top of the valence band and the bottom

of the conduction band, respectively. Relaxation occurs within 671 ps, followed by another state change to a long-lived species. The (40/60) sample has titanium oxide transferring electrons to copper oxide, leaving holes on the titanium oxide valence band. Electrons on copper oxide relax and are transferred back to titanium oxide trapped states and then to the long-lived state.

## Long-time Transient Absorption

In most cases, the PET substrate exhibits an intense signal that overcomes the sample signal. To address the non-decaying species, a long-time TA (nano to microseconds timescale) was performed. Data is presented in figure 62. The AFM measurements imply that copper oxide is a thick film with dark-coloured particles reflected in the transient absorption spectra.

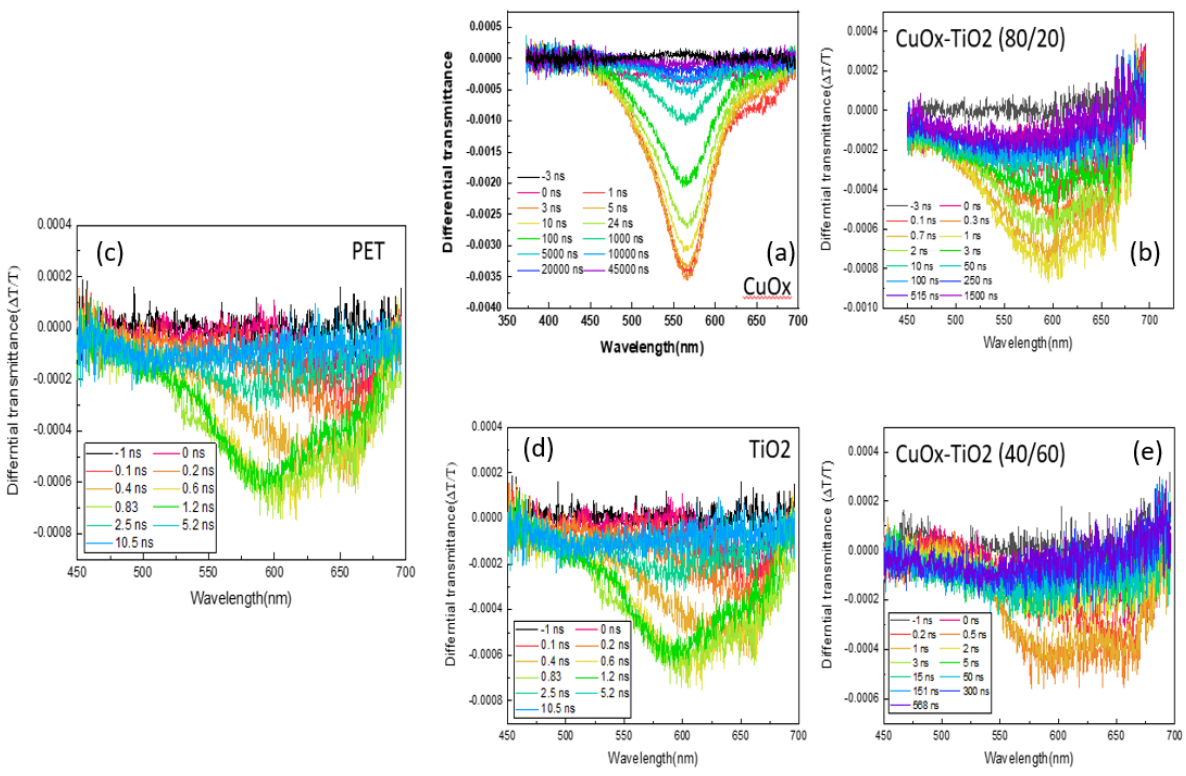


Figure 61- Long time TA for the films. a) Copper Oxide, b)Copper-Titanium 80/20, c) PET, d) Titanium Oxide, e) Copper-Titanium 40/60

## AFM and antibacterial inactivation

AFM images and compiled data are found in Figure 63 and Table 24. While $R_a$ values express the overall roughness of the sample, $R_q$ is more sensitive to microscopic peaks and valleys. $R_q/R_a$ can estimate the overall smoothness of films.

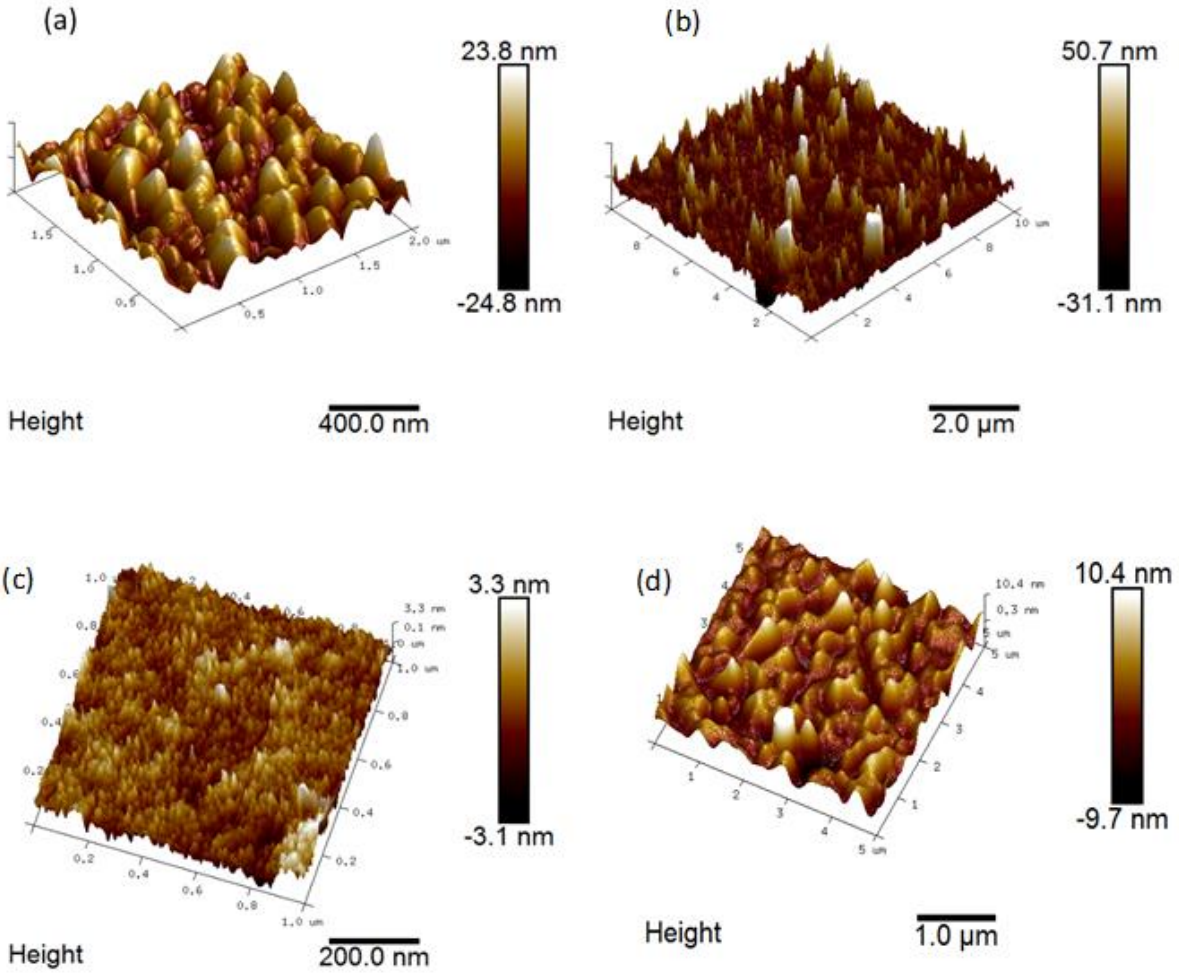


Figure 62- AFM for a) Copper Oxide, b) Titanium Oxide, c) Copper-Titanium (80/20), d) Copper-Titanium (40/60)

Table 24- AFM compiled data.

| | Thickness /nm | Contact angle Θ˚ | Average roughness (Ra) /nm | Root Mean Square (RMS/Rq) nm |
|---|---|---|---|---|
| $TiO_2$ | 24.31 ± 4.6 | 82.75 ± 1.71 | 2.6 | 3.2 |
| $TiO_2$-$CuO_x$(80/20) | 18.88 ± 1.1 | 110.25 ± 2.36 | 9.1 | 11.4 |
| TiO2-$CuO_x$(60/40) | 11 ± 2.1 | 96.89 ± 2.15 | 1.5 | 1.9 |
| CuOx | 8.78 ± 1.3 | 114.5 ± 1 | 9.6 | 11.3 |

The values above imply that the samples photophysical properties are not necessarily linked to the film's thickness. $R_q$ /$R_a$ values show no significant discrepancy, suggesting no apparent interference in film morphology and electronic properties.

Finally, the bacterial inactivation (done by Dr Rtimi) is presented in figure 64. The graph shows the efficiency of bacteria inactivation for each film. Both mixed oxides gave the best results, acting efficiently – 30 minutes or less, whereas the pure titanium oxide film took over an hour to produce a similar effect.

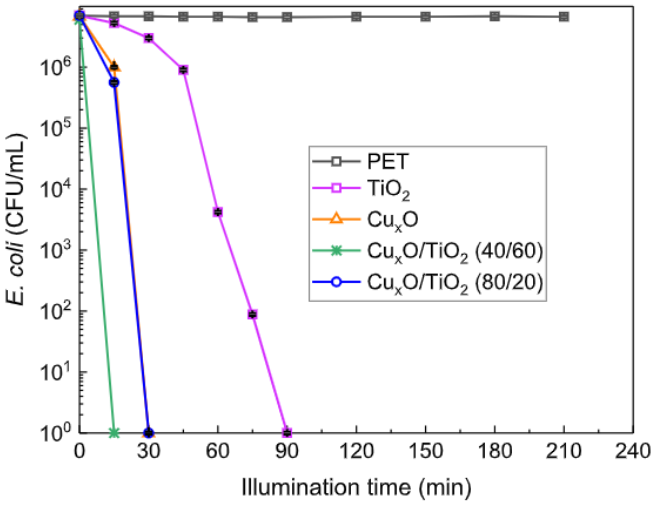


Figure 63- Bacteria inactivation (E.Coli) under indoor light

## Chapter Conclusion

We wanted to correlate ROS production to the photophysical properties of metal oxide films. In the first set of samples ($CuO_x$, $FeO_x$, $CuO_x$-$FeO_x$), XPS and UTAS map the electronic structure of the films. A clear trend is then observed as the mixed sample has a faster excited state decay overall when compared to the pure oxides. As XPS points out, the samples contained minor impurities, but they did not affect the efficiency of the films. The analysis of the oscillatory pattern of the films showed that copper oxide is the only sample that showed a strong oscillatory signal. Antibacterial tests prove that the mixed oxide is the most efficient of the three samples. Flow cytometry indicates that two mechanisms are in place, elucidating the role of the metal ions, which attacks the cell walls rapidly. The first-time constant might impact the overall dynamics, as data suggests. The non-decaying component should elucidate the relationship between trapped states in the overall dynamic, which serves as an idea for future work.

The second set of samples ($CuO_x$, $TiO_2$, $CuO_x$-$TiO_2$) received a post-adhesion plasma treatment. XPS data confirms that a higher level of oxidized metals is present for all samples and, in some cases, bonding between metal and substrate. Copper oxide contains higher Cu (I) quantities than Cu (II), which is not expected. This might reflect that the plasma treatment affected this sample more than the others. AFM is used to determine the superficial area and the thickness of the films. Titanium oxide is the thickest of the films, and according to figure 64, it is the least effective. The lifetime of the excited state decrease from the pure oxides to

the mixed oxides. When comparing the mixed oxide composition, higher concentrations of titanium lead to a better interplay between the metal atoms, as TA suggested. Based on all previous experiments, some assumptions can be made:

1) AFM shows that $TiO_2$ is the thicker sample, two times thicker than (40/60). So it is very likely that the deactivation mechanism is not influenced by thickness.
2) Morphology of the samples does not influence ROS production, as apparently there is no correlation between superficial area and the results in figure 64.
3) The lack of features (apart from PET) on the long-time TA suggests that bi-molecular recombination is not taking place.
4) XPS and TA data suggest that the concentration of the metal, specifically Titanium, is responsible for the decay mechanism and ROS formation.
5) As shown in figure 64, titanium oxide as a pure film is not efficient, so an ideal balance between titanium and copper is needed, suggesting a direct interplay between the atoms.

# References


1 United Kingdom Government, 2020.

2 United Kingdom Government, 2020.

3 C. Kuzemko, M. Bradshaw, G. Bridge, A. Goldthau, J. Jewell, I. Overland, D. Scholten, T. Van de Graaf and K. Westphal, *Energy Res. Soc. Sci.*, 2020, **68**, 101685.

4 S. E. Hosseini, *Energy Res. Soc. Sci.*, 2020, **68**, 101633.

5 T. K. With and T. H. E. Danish, .

6 M. R. Moore, T. Birth, M. J. Warren, A. G. Smith, T. Griffiths and O. Jones, 1–28.

7 Z. Valicsek and O. Horváth, *Microchem. J.*, 2013, **107**, 47–62.

8 J. H. Yoo, *Infect. Chemother.*, 2018, **50**, 101–109.

9 A. J. Jinia, N. B. Sunbul, C. A. Meert, C. A. Miller, S. D. Clarke, K. J. Kearfott, M. M. Matuszak, M. M. Matuszak and S. A. Pozzi, *IEEE Access*, 2020, **8**, 111347–111354.

10 P. Klan and K. Wirz, *Photochemistry of Organic Compounds*, Wiley Education, 1st edn., 2009.

11 C. Wayne and R. Wayne, *Photochemistry*, Oxford, 1996.

12 P. Ceroni, *The Exploration of Supramolecular Systems and Nanostructures by Photochemical Techniques*, Springer, 1st edn., 2012.

13 J.-P. Launay and M. Verdaguer, *Electrons in Molecules*, Oxford, 2016.

14 G. Lanzani, *The photophysics behind Photovoltaics and Photonics*, Wiley Education, 2012.

15 D. Harris and M. Bertolucci, *Symmetry and Spectroscopy: An Introduction to Vibrational and Electronic Spectroscopy*, Dover, 1948.

16 V. Balzani, P. Ceroni and A. Juris, *Photochemistry and Photophysics*, Wiley Education, 2014.

17 S. Addison, *Electrons, Atoms, And Molecules in Inorganic Chemistry*, 1st edn., 2017.

18 N. Turro, *Modern Molecular Photochemistry*, University Science Books, 1991.

19 T. Förster, *Ann. der Phys.*

20 T. Förster, *Radiat. Res. Suppl.*, , DOI:10.2307/3583604.

21 D. L. Dexter, *J. Chem. Phys.*, 1953, **21**, 836–850.

22 E. Abreu, S. N. Gilbert Corder, S. J. Yun, S. Wang, J. G. Ramírez, K. West, J. Zhang, S. Kittiwatanakul, I. K. Schuller, J. Lu, S. A. Wolf, H. T. Kim, M. Liu and R. D. Averitt, *Phys. Rev. B*, 2017, **96**, 1–10.

23 S. Rtimi, C. Pulgarin, V. A. Nadtochenko, F. E. Gostev and I. V Shelaev, *Nat. Publ. Gr.*, 2016, 2–11.

24 A. Bhattacharya, *Ultrafast Optics and Spectroscopy in Physical Chemistry*, World Scientific, Bangalore, 1st edn., 2018.

25 W. Shockley and W. T. Read, *Phys. Rev.*, 1952, **87**, 835–842.

26 D. Jos, A. S. Cavaleiro, P. D. Maria, P. Morgado, S. Neves, P. Associada and I. I. I. Q. Comunit, Universidade de Aveiro, 2011.

27 N. Lane, Born to the Purple: the Story of Porphyria, https://www.scientificamerican.com/article/born-to-the-purple-the-st/.

28 C. Brückner, *Acc. Chem. Res.*, 2016, **49**, 1080–1092.

29 A. N. Okhrimenko, M. A. J. Rodgers, S. L. Smith, M. Y. Ogawa and T. H. Kinstle, Bowling Green State University, 2005.

30 M. Aydin, *Molecules*, 2014, **19**, 20988–21021.

31 H. Khan, The University of Sheffield, 2017.

32 P. J. Spellane, M. Gouterman, A. Antipas, S. Kim and Y. C. Liu, *Inorg. Chem.*, 1980, **19**, 386–391.

33 M. Gouterman, *J. Mol. Spectrosc.*, 1961, **6**, 138–163.

34 M. Gouterman and G. Wagniere, *J. Mol. Spectrosc.*, 1963, **11**, 108–127.

35 R. Giovannetti, *Macro To Nano Spectrosc.*, , DOI:10.5772/38797.

36 H. Kano, T. Saito and T. Kobayashi, *J. Phys. Chem. A*, 2002, **106**, 3445–3453.

37 G. J. Small, , DOI:10.1063/1.1675343.

38 K. S. Suslick and R. A. Watson, 1992, 633–642.

39 A. Antipas, J. W. Buchler, M. Gouterman and P. D. Smithzb, , DOI:10.1021/ja00478a013.

40 J. R. Reimers, Z. L. Cai, R. Kobayashi, M. Rätsep, A. Freiberg and E. Krausz, *Sci. Rep.*, , DOI:10.1038/srep02761.

41 M. Kotani, *Ann. N. Y. Acad. Sci.*, 1969, **158**, 20–49.

42 A. S. Rury and R. J. Sension, *Chem. Phys.*, 2013, **422**, 220–228.

43 S. Sorgues, L. Poisson, K. Raffael, L. Krim, B. Soep, N. Shafizadeh and S. Sorgues, , DOI:10.1063/1.2176612.

44 Turro, *Modern Molecular Photochemistry*, University Science Books.

45 Y. Venkatesh, M. Venkatesan, B. Ramakrishna and P. R. Bangal, , DOI:10.1021/acs.jpcb.6b05767.

46 S. Akimoto, T. Yamazaki, I. Yamazaki and A. Osuka, *Chem. Phys. Lett.*, 1999, **309**, 177–182.

47 J. Petersson, , DOI:10.1021/jp5113119.

48 P. H. Kumar, Y. Venkatesh, D. Siva, B. Ramakrishna and P. R. Bangal, *J. Phys. Chem. A*, 2015, **119**, 1267–1278.

49 A. A. L. Haddad, .

50 S. Perun, J. Tatchen and C. M. Marian, 2008, 282–292.

51 E. I. Sagun, E. I. Zenkevich, V. N. Knyukshto, A. Y. Panarin, A. S. Semeikin and T. V. Lyubimova, *Opt. Spectrosc. (English Transl. Opt. i Spektrosk.*, 2012, **113**, 388–400.

52 T. J. Penfold, E. Gindensperger, C. Daniel and C. M. Marian, *Chem. Rev.*, 2018, **118**,

6975–7025.

53 P. B. Barna, .

54 N. G. Park, *Mater. Today*, 2015, **18**, 65–72.

55 R. Wang, M. Mujahid, Y. Duan, Z. K. Wang, J. Xue and Y. Yang, *Adv. Funct. Mater.*, 2019, **29**, 1–25.

56 J. Finkel, University of Sheffield, 2017.

57 A. Graf, J. Finkel, A. A. P. Chauvet and S. Rtimi, *ACS Appl. Mater. Interfaces*, 2019, **11**, 45319–45329.

58 A. Graf, Universidade Federal do Rio de Janeiro, 2017.

59 S. Giannakis, , DOI:10.3390/molecules22071074.

60 D. Wang, L. Zhao, H. Zhang and L. Guo, , DOI:10.1021/acs.est.7b00473.

61 T. J. Miao and J. Tang, *J. Chem. Phys.*, 2020, **152**, 194201.

62 Y. Li, W. Zhang, J. Niu and Y. Chen, *ACS Nano*, 2012, **6**, 5164–5173.

63 C. Britton-powell and C. Britton-powell, .

64 K. Krumova, G. Cosa, J. Aubry and J. R. Kanofsky, *Singlet Oxyg. Appl. Biosci. Nanosci.*, 2016, 1–4.

65 M. A. Hyland, M. D. Morton and C. Bru, .

66 A. Vogel, S. Dechert, C. Brückner and F. Meyer, *Inorg. Chem.*, 2017, **56**, 2221–2232.

67 S. Rtimi, C. Pulgarin and J. Kiwi, *Coatings*, , DOI:10.3390/coatings7020020.

68 J. Watts and J. Wolstenholme, *An Introduction to Surface Analysis by XPS and AES*, Wiley, 2005.

69 K. Yanagiuchi, *J. Surf. Anal.*, 2019, **25**, 192–201.

70 R. Berera, Æ. R. Van Grondelle and Æ. J. T. M. Kennis, 2009, 105–118.

71 H. Khan, University of Sheffield, 2018.

72 M. V. Appleby, P. G. Walker, D. Pritchard, S. van Meurs, C. M. Booth, C. Robertson, M. D. Ward, D. J. Kelly and J. A. Weinstein, *Mater. Adv.*, 2020, **1**, 3417–3427.

73 N. Chaudhri, M. Zeller and C. Brückner, *J. Org. Chem.*, 2020, **85**, 13951–13964.

74 S. Perun, J. Tatchen and C. M. Marian, *ChemPhysChem*, 2008, **9**, 282–292.

75 A. K. Mandal, M. Taniguchi, J. R. Diers, D. M. Niedzwiedzki, C. Kirmaier, J. S. Lindsey, D. F. Bocian and D. Holten, *J. Phys. Chem. A*, 2016, **120**, 9719–9731.

76 I. V Avilov, E. I. Zenkevich, E. I. Sagun and I. V Filatov, 2004, 5684–5691.

77 J. S. Baskin, H. Z. Yu and A. H. Zewail, *J. Phys. Chem. A*, 2002, **106**, 9837–9844.

78 P. Fita, A. Listkowski, M. Kijak, S. Nonell, D. Kuzuhara, H. Yamada and J. Waluk, *J. Phys. Chem. B*, 2015, **119**, 2292–2301.

79 B. Maren and M. O. Senge, 2010, 1152–1158.

80 R. Schmidt, C. Tanielian and C. Dunsbach, Ralf; Wolff, *J. Photochem. Photobiol. A Chem.*, 1994, **79**, 11–17.

81 M. Pelaez, N. T. Nolan, S. C. Pillai, M. K. Seery, P. Falaras, A. G. Kontos, P. S. M. Dunlop, J. W. J. Hamilton, J. A. Byrne, K. O'Shea, M. H. Entezari and D. D. Dionysiou, *Appl. Catal. B Environ.*, 2012, **125**, 331–349.

82 S. Rtimi, C. Pulgarin, V. A. Nadtochenko, F. E. Gostev, I. V. Shelaev and J. Kiwi, *Sci. Rep.*, 2016, **6**, 2–11.

83 S. Rtimi, *Coatings*, 2021, **11**, 1–3.

84 M. Abidi, A. A. Assadi, A. Bouzaza, A. Hajjaji, B. Bessais and S. Rtimi, *Appl. Catal. B Environ.*, 2019, **259**, 118074.

85 S. Mathews, M. Hans, F. Mücklich and M. Solioz, *Appl. Environ. Microbiol.*, 2013, **79**, 2605–2611.

86 H. A. Foster, I. B. Ditta, S. Varghese and A. Steele, *Appl. Microbiol. Biotechnol.*, 2011, **90**, 1847–1868.

87 W. Dröge, *Physiol. Rev.*, 2002, **82**, 47–95.

88 R. Gerschman, D. L. Gilbert, S. W. Nye, P. Dwyer and W. O. Fenn, *Science (80-. ).*, 1954, **119**, 623–626.

89 B. P. Payne, M. C. Biesinger and N. S. McIntyre, *J. Electron Spectros. Relat. Phenomena*, 2011, **184**, 29–37.

90 D. Beamson, G.; Briggs, *J. Chem. Educ.*, 1993, **73**, A92.

91 Thermo Scientific, XPS Simplified, https://xpssimplified.com/periodictable.php.

92 T. NAKAMURA, H. TOMIZUKA, M. TAKAHASHI and T. HOSHI, *Hyomen Kagaku*, 1995, **16**, 515–520.

93 J. C. Otamiri, S. L. T. Andersson and A. Andersson, *Appl. Catal.*, 1990, **65**, 159–174.

94 J. R. Monnier, M. J. Hanrahan and G. Apai, *J. Catal.*, 1985, **92**, 119–126.

95 D. A. Pawlak, M. Ito, M. Oku, K. Shimamura and T. Fukuda, *J. Phys. Chem. B*, 2002, **106**, 504–507.

96 V. I. Nefedov, M. N. Firsov and I. S. Shaplygin, *J. Electron Spectros. Relat. Phenomena*, 1982, **26**, 65–78.

97 M. C. Biesinger, B. P. Payne, A. P. Grosvenor, L. W. M. Lau, A. R. Gerson and R. S. C. Smart, *Appl. Surf. Sci.*, 2011, **257**, 2717–2730.

98 G. C. Allen and M. Paul, *J. Chem. Soc. Faraday Trans.*, 1995, **91**, 3717–3723.

99 E. Abreu, S. N. Gilbert Corder, S. J. Yun, S. Wang, J. G. Ramírez, K. West, J. Zhang, S. Kittiwatanakul, I. K. Schuller, J. Lu, S. A. Wolf, H. T. Kim, M. Liu and R. D. Averitt, *Phys. Rev. B*, , DOI:10.1103/PhysRevB.96.094309.

100 Y. D. Glinka, S. Babakiray, T. A. Johnson, M. B. Holcomb and D. Lederman, *J. Appl. Phys.*, , DOI:10.1063/1.4919274.

101 S. Sorenson, E. Driscoll, S. Haghighat and J. M. Dawlaty, *J. Phys. Chem. C*, 2014, **118**, 23621–23626.

102 A. Graf, J. Finkel, A. A. P. Chauvet and S. Rtimi, *ACS Appl. Mater. Interfaces*, 2019, **11**, 45319–45329.

103 A. G. Joly, J. R. Williams, S. A. Chambers, G. Xiong, W. P. Hess and D. M. Laman, *J. Appl. Phys.*, , DOI:10.1063/1.2177426.

104 World Health Organization, *Who/Sde/Wsh/03.04/08*, 2003, **2**, 4.

105 World Health Organization, *Ann. Public Coop. Econ.*, 1997, **68**, 39–64.

106 S. Rtimi, S. Konstantinidis, N. Britun, M. Bensimon, I. Khmel and V. Nadtochenko, *Appl. Catal. B Environ.*, 2018, **239**, 245–253.

107 V. Bukauskas, S. Kaciulis, A. Mezzi, G. Niaura, M. Rudzikas and Š. Irena, 2015, **585**, 5–12.

108 S. Saied, J. Sullivan, T. Choudhury and C. Pearce, *Vacuum*, 1988, **38**, 917–922.

109 C. Tio, C. Lee and J. Y. Park, 2019, 18371–18376.

110 J. P. Lafemina, P. O. Box, G. Arjavalingam, I. B. M. Thomas, P. O. Box, Y. Heights and N. York, 1991, **99352**, 984–988.

111 M. F. Sonnenschein and C. M. Roland, 1990, **31**, 2023–2026.

112 Q. Hu, J. Huang, G. Li, J. Chen, Z. Zhang, Z. Deng, Y. Jiang, W. Guo and Y. Cao, *Appl. Surf. Sci.*, 2016, **369**, 201–206.

113 F. Zuo, K. Bozhilov, R. J. Dillon, L. Wang, P. Smith, X. Zhao, C. Bardeen and P. Feng, *Angew. Chemie - Int. Ed.*, 2012, **51**, 6223–6226.

# Supplementary Information

## Deconvolution of UV-Vis Spectra for the second sets of films.

Adopted from [63]

Pseudo-Voight formula:

$$y = y_0 + A\left[m_u \frac{2}{\pi}\frac{w}{4(x-x_c)^2+w^2} + (1-m_u)\frac{\sqrt{4ln2}}{\sqrt{\pi}w}e^{-\frac{4ln2}{w^2}(x-x_c)^2}\right]$$

Sample curve:

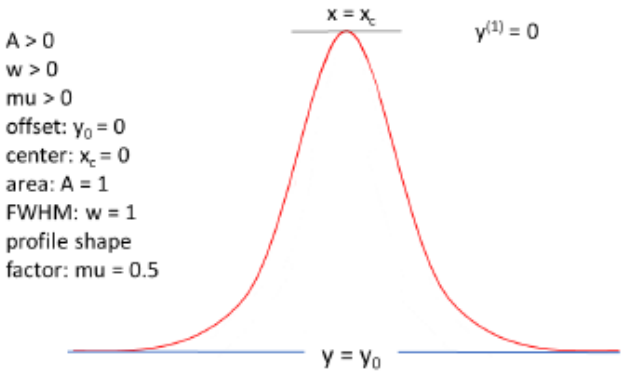


Tables of fit parameters for CuOx, $TiO_2$, PET, CuOx $TiO_2$ 80:20 and CuOx $TiO_2$ 40:60:

| CuOx | | | |
|---|---|---|---|
| Model | Pseudo-Voight 1 | | |
| xc | 240.74581 ± 2.382 | 372.27839 ± 8.96948 | 469.93543 ± 1.69054 |
| A | 83.82202 ± 40.04028 | 150.5321 ± 35.20567 | 37.0789 ± 12.09666 |
| w | 123.0638 ± 21.24998 | 203.37463 ± 20.95891 | 109.56755 ± 8.45253 |
| mu | 0.77664 ± 0.39473 | 0.50096 ± 0.11784 | 0 ± 0.15629 |
| Reduced Chi-Sqr | 2.80E-05 | | |
| R-Square (COD) | 0.99967 | | |
| Adj. R-square | 0.99967 | | |

| TiO2 | | | |
|---|---|---|---|
| Model | Pseudo-Voight 1 | | |
| xc | 312.83268 ± 0.08287 | 350.39622 ± 17.58513 | 631.93778 ± 1.9671 |
| A | 49.18665 ± 1.16311 | 28.86507 ± 6.22885 | 7.19385 ± 2.85109 |
| w | 49.9941 ± 0.24066 | 296.47832 ± 21.06569 | 140.78456 ± 16.10406 |
| mu | 0.2214 ± 0.03014 | 0 ± 0.58021 | 0.6801 ± 0.29203 |
| Reduced Chi-Sqr | 8.79E-06 | | |
| R-Square (COD) | 0.99979 | | |
| Adj. R-square | 0.99978 | | |

| PET | | | | | |
|---|---|---|---|---|---|
| Model | Pseudo-Voight 1 | | | | |
| xc | 217.07204 ± 1.05328 | 284.99501 ± 1.63769 | 304.43484 ± 1.63276 | 314.35081 ± 0.30231 | 620.31642 ± 2.41889 |
| A | 82.09628 ± 5.25969 | 53.39099 ± 5.74415 | 6.34306 ± 3.57678 | 3.51852 ± 0.90351 | 0.45227 ± 0.13781 |
| w | 78.97038 ± 3.28062 | 50.02939 ± 2.22676 | 18.88269 ± 1.83433 | 9.96185 ± 0.72468 | 41.31363 ± 6.66865 |
| mu | 0 ± 0.08998 | 0.97458 ± 0.07476 | 0 ± 0.95428 | 0 ± 0.21596 | 0 ± 0.91384 |
| Reduced Chi-Sqr | 3.07E-05 | | | | |
| R-Square (COD) | 0.9997 | | | | |
| Adj. R-square | 0.99969 | | | | |

| CuOx TiO2 80:20 | | | | |
|---|---|---|---|---|
| Model | Pseudo-Voight 1 | | | |
| xc | 271.27182 ± 2.34396 | 311.97052 ± 0.13545 | 359.59071 ± 17.36594 | 464.67766 ± 10.24099 |
| A | 66.85556 ± 17.27748 | 2.70609 ± 0.5746 | 36.37107 ± 15.17341 | 2.0534 ± 1.07409 |
| w | 88.74049 ± 6.22843 | 17.9234 ± 0.6857 | 144.27327 ± 28.50548 | 91.10221 ± 12.5384 |
| mu | 0 ± 0.47254 | 0 ± 0.32769 | 0.80937 ± 0.22854 | 0 ± 0.93285 |
| Reduced Chi-Sqr | 1.53E-05 | | | |
| R-Square (COD) | 0.99965 | | | |
| Adj. R-square | 0.99964 | | | |

| CuOx TiO2 40:60 | | | | | | |
|---|---|---|---|---|---|---|
| Model | Pseudo-Voight 1 | | | | | |
| xc | 208.37926 ± 58.69672 | 284.6973 ± 3.40209 | 320.08194 ± 2.44538 | 357.63746 ± 13.204 | 457.59892 ± 11.66765 | 621.24295 ± 1.16528 |
| A | 112.43318 ± 119.51026 | 36.96316 ± 208.43173 | 10.76939 ± 6.0833 | 26.71534 ± 81.36412 | 7.05825 ± 13.56037 | 8.73666 ± 1.7206 |
| w | 100 ± 61.28974 | 76.96877 ± 138.60555 | 40.5057 ± 4.94653 | 100 ± 65.81275 | 100 ± 46.86223 | 100 ± 7.20558 |
| mu | 0.75606 ± 2.38946 | 0.96824 ± 4.64003 | 0 ± 0.31499 | 1 ± 1.32816 | 0.89948 ± 0.26722 | 1 ± 0.13862 |
| Reduced Chi-Sqr | 1.84E-05 | | | | | |
| R-Square (COD) | 0.99966 | | | | | |
| Adj. R-square | 0.99965 | | | | | |

## Breathing Mode representation

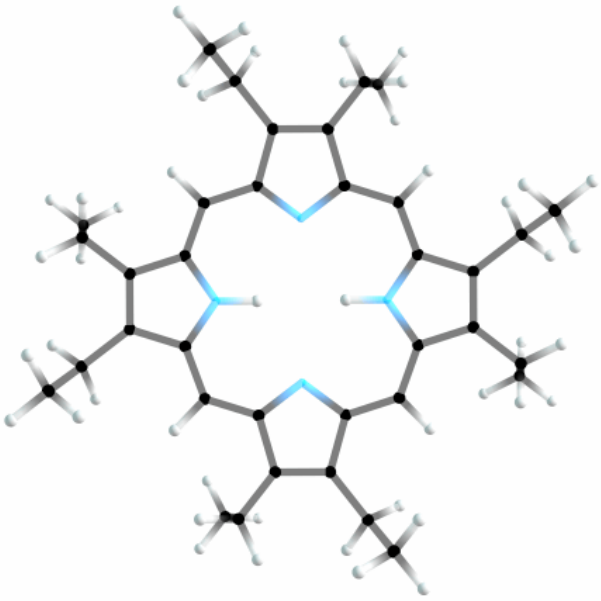

## Oscillator Strength values

| | OEP-RL | | RL-2-oxochlorin | | RL-2,13-dioxochlorin | | RL-2,18-dioxochlorin | |
|---|---|---|---|---|---|---|---|---|
| | **Excitation Energy (nm)** | **Oscillator Strength** | **Excitation Energy (nm)** | **Oscillator Strength** | **Excitation Energy (nm)** | **Oscillator Strength** | **Excitation Energy (nm)** | **Oscillator Strength** |
| **$S_1$** | 558,3 | 0,044 | 570,6 | 0,055 | 592,4 | 0,114 | 568,8 | 0,012 |
| **$S_2$** | 525,3 | 0,088 | 534 | 0,011 | 541,4 | 0,006 | 565 | 0,067 |
| **$S_3$** | 406,2 | 0,294 | 412,1 | 0,128 | 411 | 0,019 | 463 | 0,001 |
| **$S_4$** | 399,5 | 0,007 | 411,5 | 0,006 | 409,7 | 0,023 | 413,6 | 0,005 |
| **$S_5$** | 383,5 | 0,285 | **395,7** | **0,307** | **394,8** | **0,616** | 393,1 | 0,145 |
| **$S_6$** | 380,7 | 0,001 | **372,1** | **1,163** | **386,8** | **0,922** | **391** | **0,831** |
| **$S_7$** | **358,4** | **1,058** | 365,1 | 0,194 | 381 | 0,027 | **384,9** | **0,982** |
| **$S_8$** | **348,8** | **1,167** | 364,1 | 0,28 | 380,8 | 0,113 | 351,2 | 0,004 |
| **$S_9$** | 322,3 | 0,011 | 338,6 | 0,008 | 350,9 | 0,001 | 341,9 | 0,213 |
| **$S_{10}$** | 319,5 | 0 | 334,3 | 0,026 | 343,6 | 0,008 | 328,6 | 0,004 |

## AFM Thickness Calculation [63]

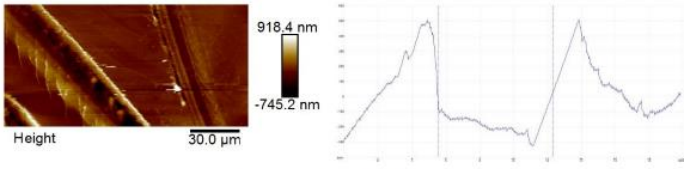


*Figure A1 - average thickness for CuOx thin film calculated as 22 nm*

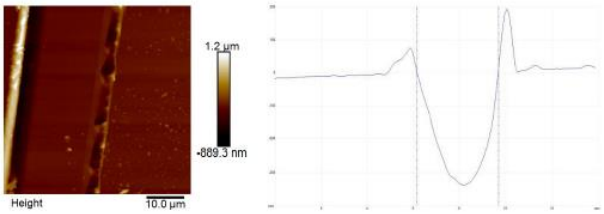


*Figure A2 - average thickness for CuOx $TiO_2$ 80:20 thin film calculated as 17 nm*

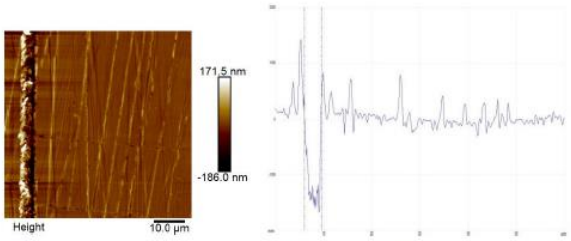


*Figure A3 - average thickness for CuOx $TiO_2$ thin film calculated as 30 nm*

## Linear Fit – Singlet Oxygen – Remaining Samples

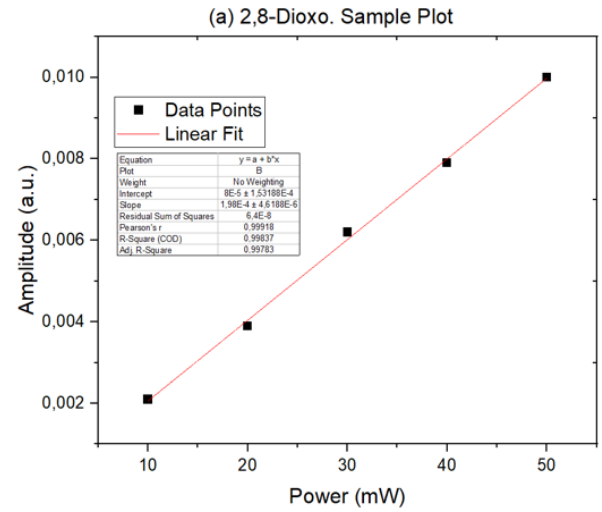


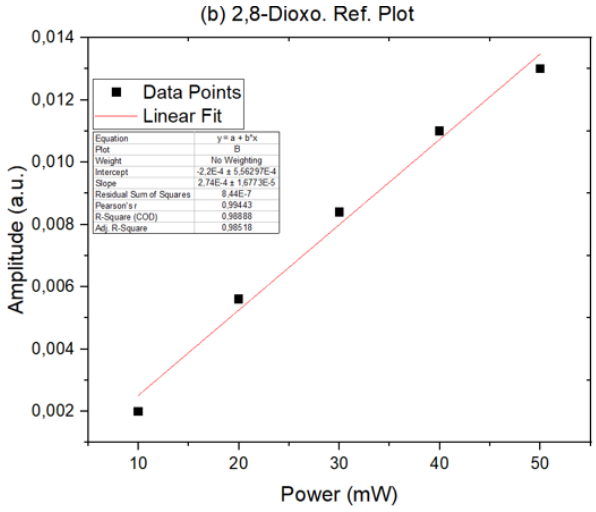


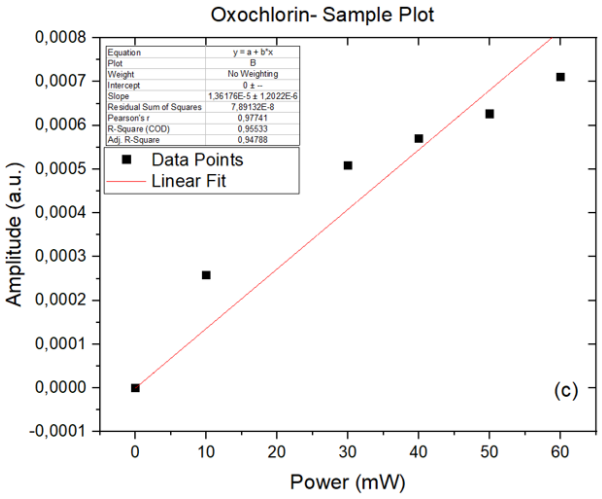


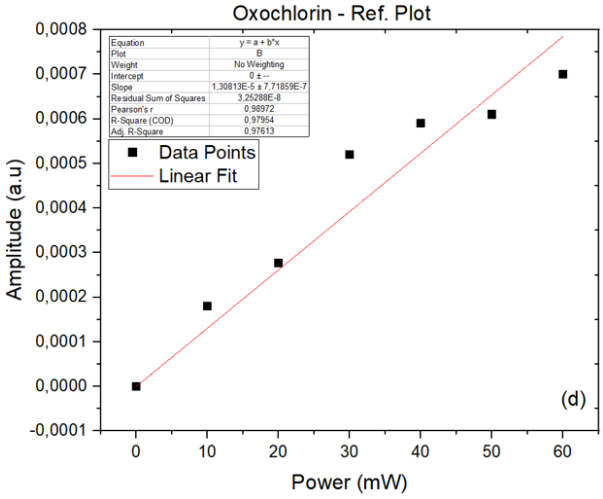


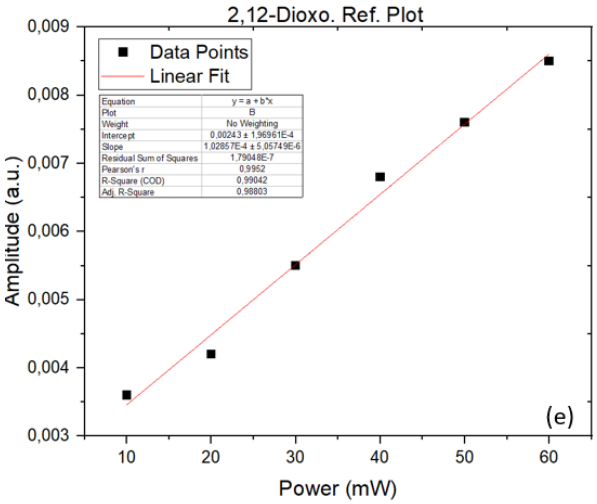


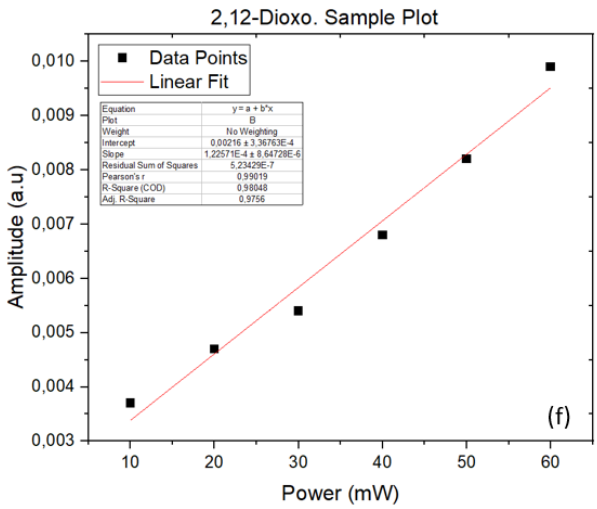

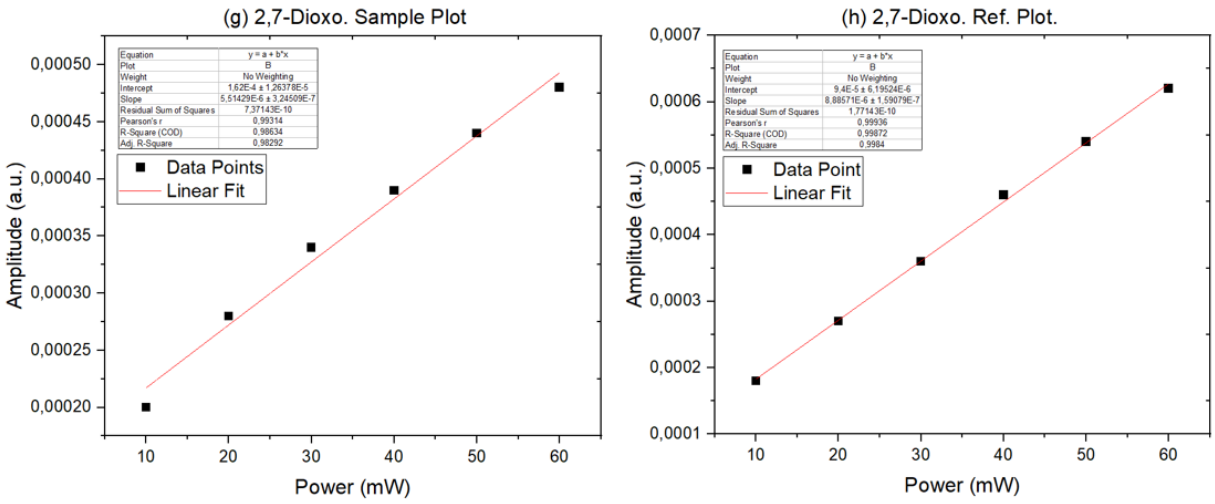


## Power Fit- Singlet Oxygen – All Samples

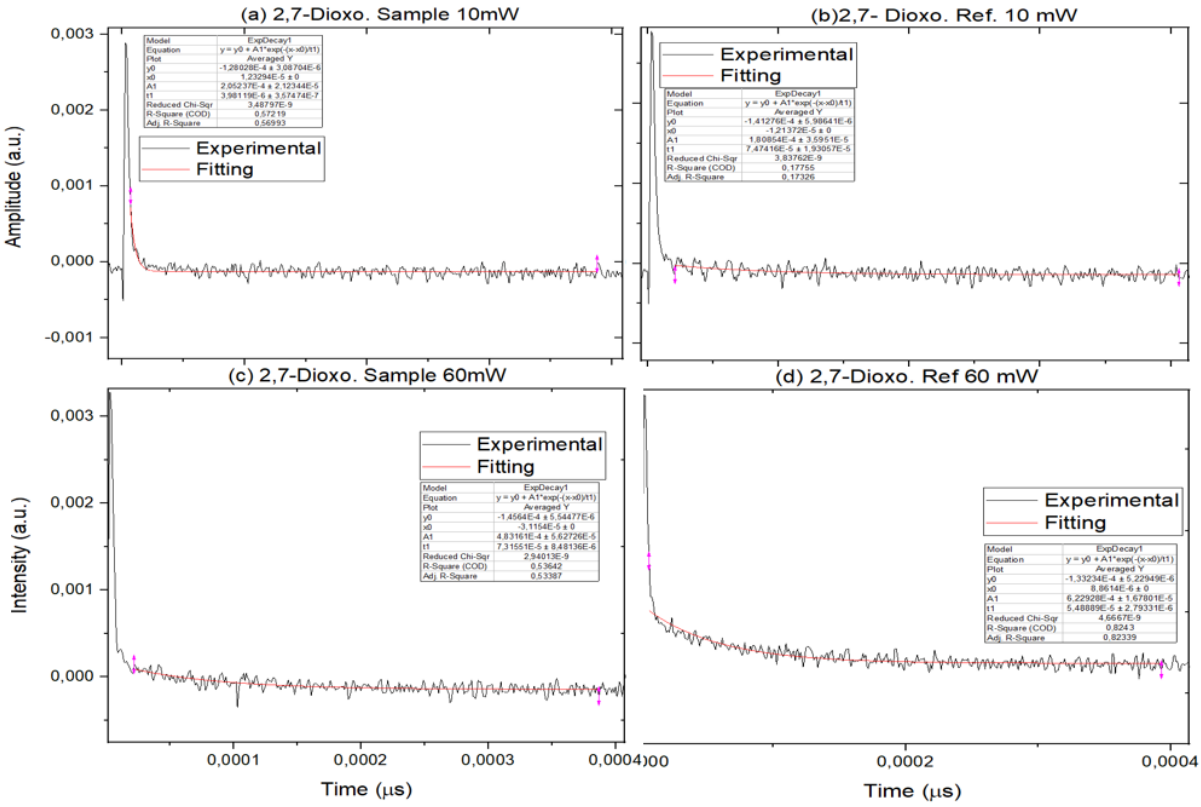

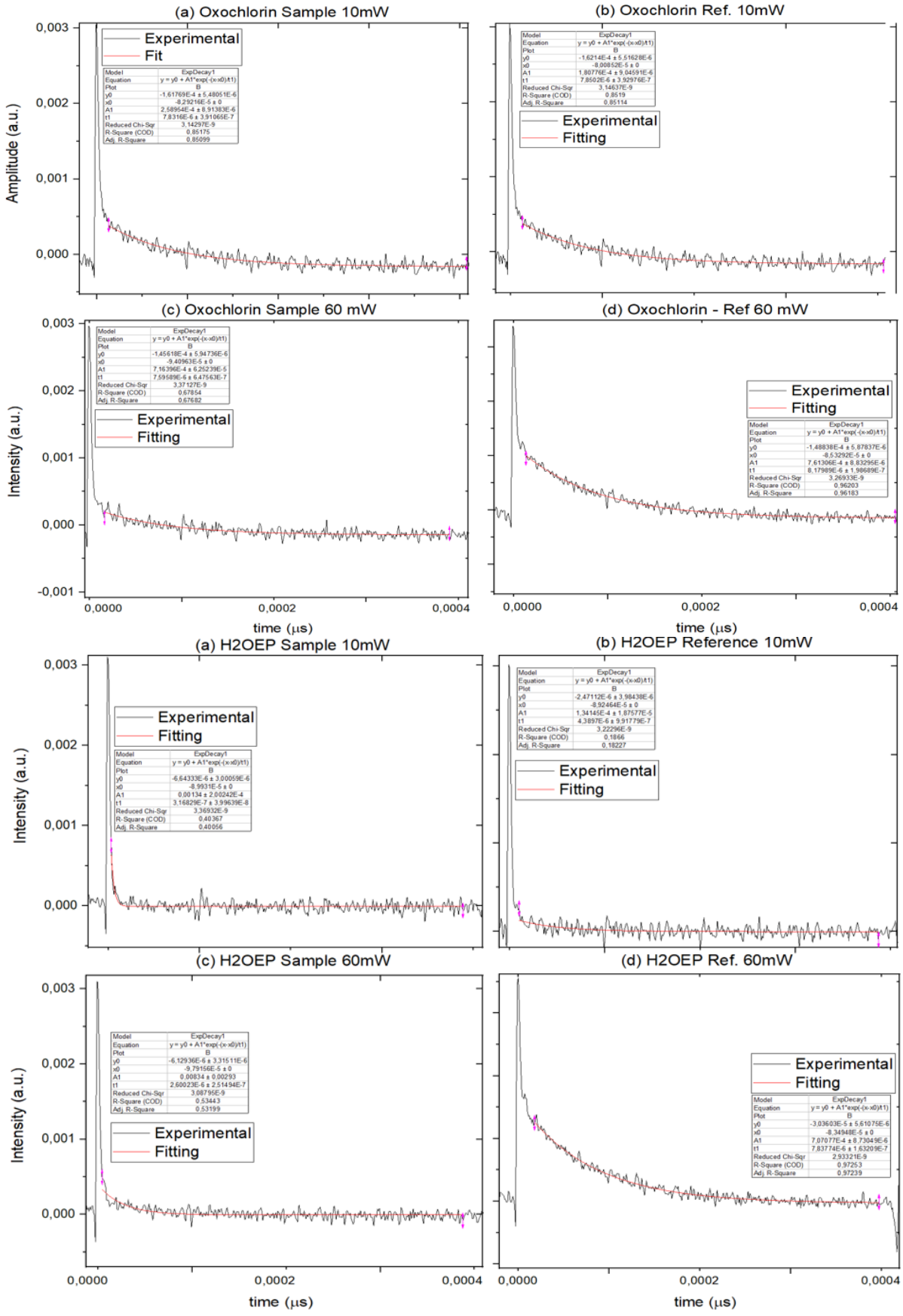
(a) Oxochlorin Sample 10mW
Experimental
Fit
Model ExpDecay1
Equation y = y0 + A1*exp(-(x-x0)/t1)
Plot B
y0 -1,61769E-4 ± 5,48051E-6
x0 -8,29216E-5 ± 0
A1 2,58954E-4 ± 8,91383E-6
t1 7,8316E-6 ± 3,91065E-7
Reduced Chi-Sqr 3,14297E-9
R-Square (COD) 0,85175
Adj. R-Square 0,85099
(b) Oxochlorin Ref. 10mW
Model ExpDecay1
Equation y = y0 + A1*exp(-(x-x0)/t1)
Plot B
y0 -1,6214E-4 ± 5,51628E-6
x0 -8,00852E-5 ± 0
A1 1,80776E-4 ± 9,04591E-6
t1 7,8502E-6 ± 3,92976E-7
Reduced Chi-Sqr 3,14637E-9
R-Square (COD) 0,8519
Adj. R-Square 0,85114
Experimental
Fitting
(c) Oxochlorin Sample 60 mW
Model ExpDecay1
Equation y = y0 + A1*exp(-(x-x0)/t1)
Plot B
y0 -1,45618E-4 ± 5,94736E-6
x0 -9,40963E-5 ± 0
A1 7,16396E-4 ± 6,25239E-5
t1 7,59589E-6 ± 6,47563E-7
Reduced Chi-Sqr 3,37127E-9
R-Square (COD) 0,67854
Adj. R-Square 0,67682
Experimental
Fitting
(d) Oxochlorin - Ref 60 mW
Experimental
Fitting
Model ExpDecay1
Equation y = y0 + A1*exp(-(x-x0)/t1)
Plot B
y0 -1,48838E-4 ± 5,87837E-6
x0 -8,53292E-5 ± 0
A1 7,61306E-4 ± 8,83295E-6
t1 8,17989E-6 ± 1,98689E-7
Reduced Chi-Sqr 3,26933E-9
R-Square (COD) 0,96203
Adj. R-Square 0,96183
Amplitude (a.u.)
Intensity (a.u.)
time (μs)
0,003
0,002
0,001
0,000
-0,001
0,0000
0,0002
0,0004
(a) H2OEP Sample 10mW
Experimental
Fitting
Model ExpDecay1
Equation y = y0 + A1*exp(-(x-x0)/t1)
Plot B
y0 -6,64333E-6 ± 3,00059E-6
x0 -8,9931E-5 ± 0
A1 0,00134 ± 2,00242E-4
t1 3,16829E-7 ± 3,99639E-8
Reduced Chi-Sqr 3,36932E-9
R-Square (COD) 0,40367
Adj. R-Square 0,40056
(b) H2OEP Reference 10mW
Model ExpDecay1
Equation y = y0 + A1*exp(-(x-x0)/t1)
Plot B
y0 -2,47112E-6 ± 3,98438E-6
x0 -8,92464E-5 ± 0
A1 1,34145E-4 ± 1,87577E-5
t1 4,3897E-6 ± 9,91779E-7
Reduced Chi-Sqr 3,22296E-9
R-Square (COD) 0,1866
Adj. R-Square 0,18227
Experimental
Fitting
(c) H2OEP Sample 60mW
Model ExpDecay1
Equation y = y0 + A1*exp(-(x-x0)/t1)
Plot B
y0 -6,12936E-6 ± 3,31511E-6
x0 -9,79156E-5 ± 0
A1 0,00834 ± 0,00293
t1 2,60023E-6 ± 2,51494E-7
Reduced Chi-Sqr 3,08795E-9
R-Square (COD) 0,53443
Adj. R-Square 0,53199
Experimental
Fitting
(d) H2OEP Ref. 60mW
Experimental
Fitting
Model ExpDecay1
Equation y = y0 + A1*exp(-(x-x0)/t1)
Plot B
y0 -3,03603E-5 ± 5,61075E-6
x0 -8,34948E-5 ± 0
A1 7,07077E-4 ± 8,73049E-6
t1 7,83774E-6 ± 1,63209E-7
Reduced Chi-Sqr 2,93321E-9
R-Square (COD) 0,97253
Adj. R-Square 0,97239
Intensity (a.u.)
time (μs)
0,003
0,002
0,001
0,000
0,0000
0,0002
0,0004

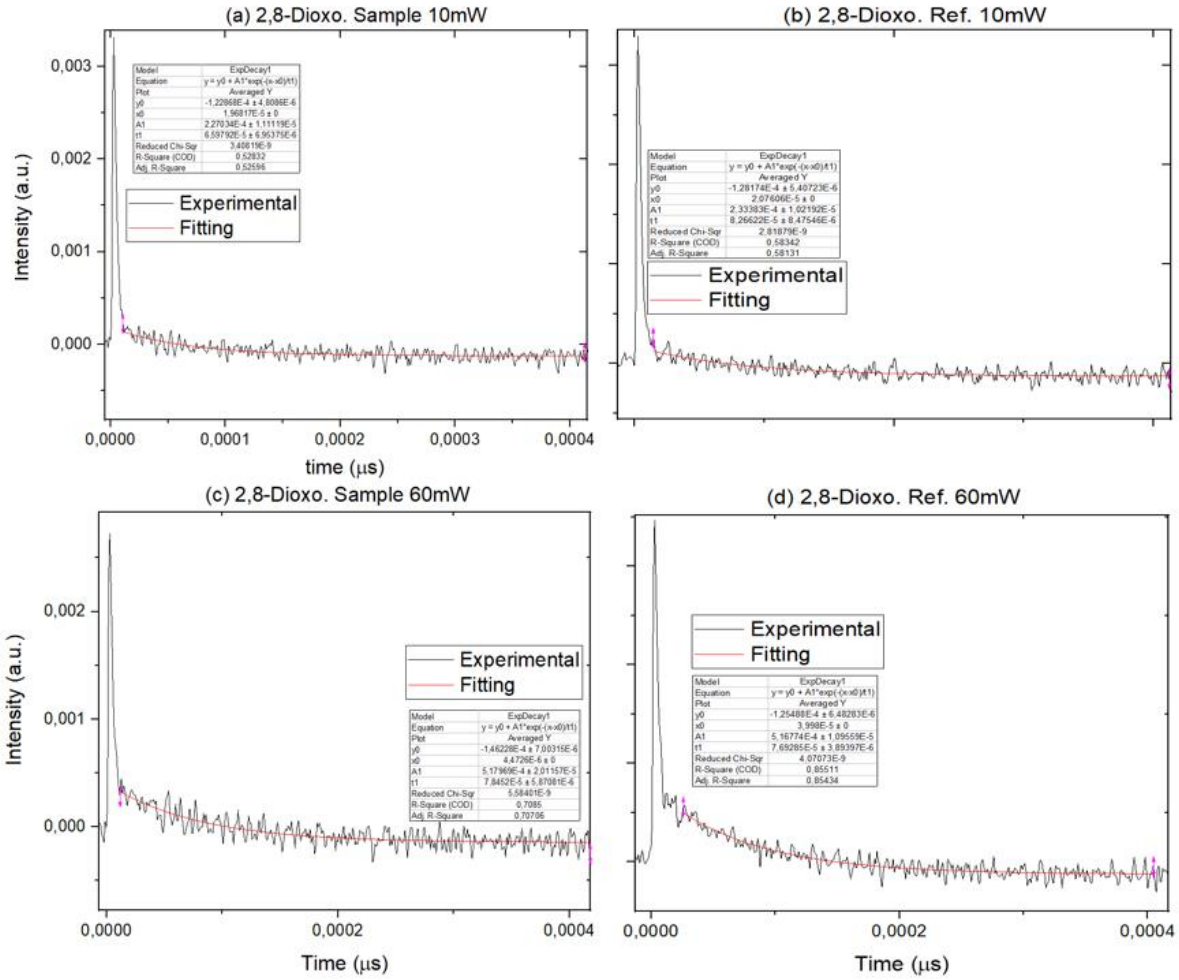
(a) 2,8-Dioxo. Sample 10mW
Model ExpDecay1
Equation y = y0 + A1*exp(-(x-x0)/t1)
Plot Averaged Y
y0 -1,22868E-4 ± 4,8086E-6
x0 1,96817E-5 ± 0
A1 2,27034E-4 ± 1,11119E-5
t1 6,59792E-5 ± 6,96375E-6
Reduced Chi-Sqr 3,40619E-9
R-Square (COD) 0,52832
Adj. R-Square 0,52596
Experimental
Fitting
Intensity (a.u.)
time (μs)
(b) 2,8-Dioxo. Ref. 10mW
Model ExpDecay1
Equation y = y0 + A1*exp(-(x-x0)/t1)
Plot Averaged Y
y0 -1,28174E-4 ± 6,48723E-6
x0 2,07606E-5 ± 0
A1 2,33383E-4 ± 1,02192E-5
t1 8,26622E-5 ± 8,47546E-6
Reduced Chi-Sqr 2,81879E-9
R-Square (COD) 0,58342
Adj. R-Square 0,58131
Experimental
Fitting
(c) 2,8-Dioxo. Sample 60mW
Model ExpDecay1
Equation y = y0 + A1*exp(-(x-x0)/t1)
Plot Averaged Y
y0 -1,46228E-4 ± 7,00315E-6
x0 4,4726E-6 ± 0
A1 5,17969E-4 ± 2,01157E-5
t1 7,8452E-5 ± 5,87081E-6
Reduced Chi-Sqr 5,58401E-9
R-Square (COD) 0,7085
Adj. R-Square 0,70706
Experimental
Fitting
Intensity (a.u.)
Time (μs)
(d) 2,8-Dioxo. Ref. 60mW
Model ExpDecay1
Equation y = y0 + A1*exp(-(x-x0)/t1)
Plot Averaged Y
y0 -1,25488E-4 ± 6,48283E-6
x0 3,998E-5 ± 0
A1 5,16774E-4 ± 1,09559E-5
t1 7,69285E-5 ± 3,89397E-6
Reduced Chi-Sqr 4,07073E-9
R-Square (COD) 0,85511
Adj. R-Square 0,85434
Experimental
Fitting
Time (μs)

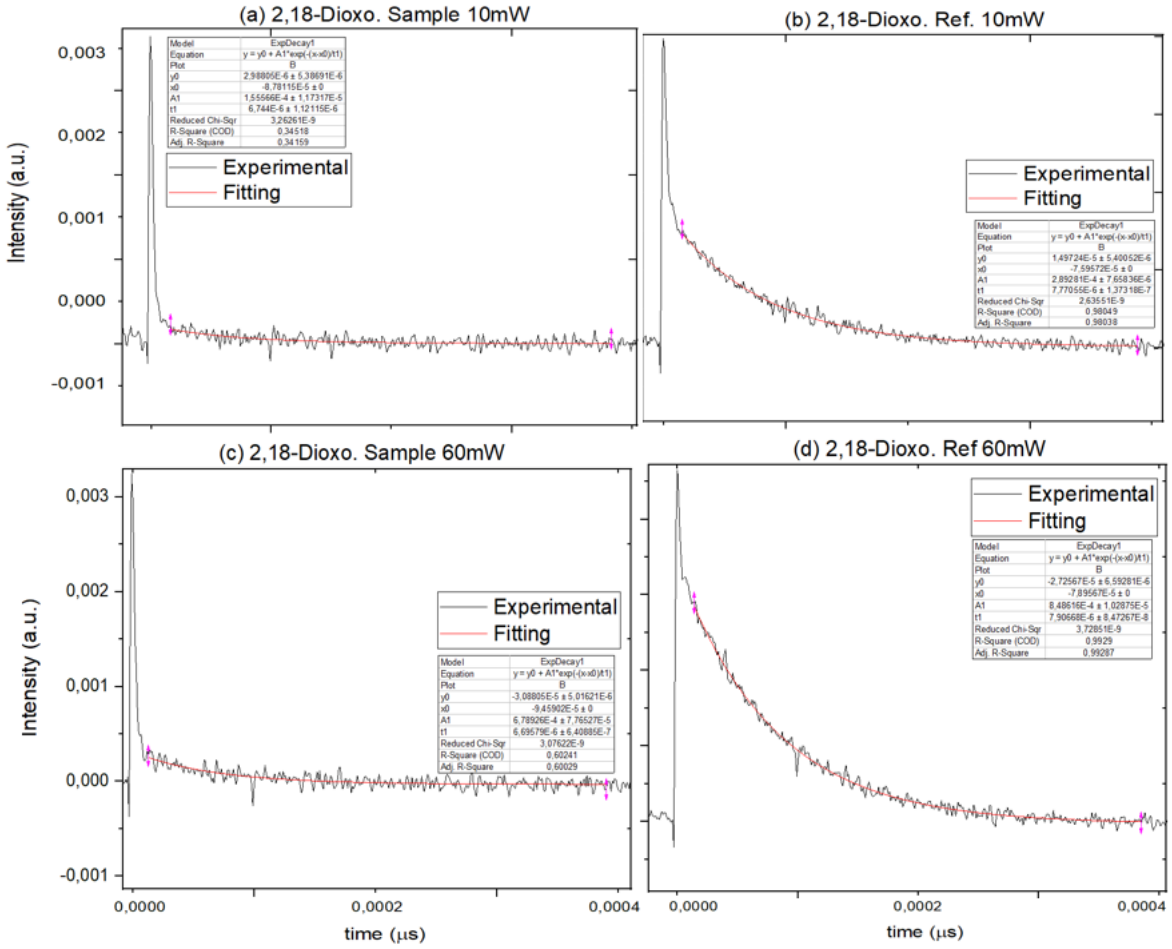
(a) 2,18-Dioxo. Sample 10mW
(b) 2,18-Dioxo. Ref. 10mW
(c) 2,18-Dioxo. Sample 60mW
(d) 2,18-Dioxo. Ref 60mW
Experimental
Fitting
Intensity (a.u.)
time (μs)
0,003
0,002
0,001
0,000
-0,001
0,0000
0,0002
0,0004

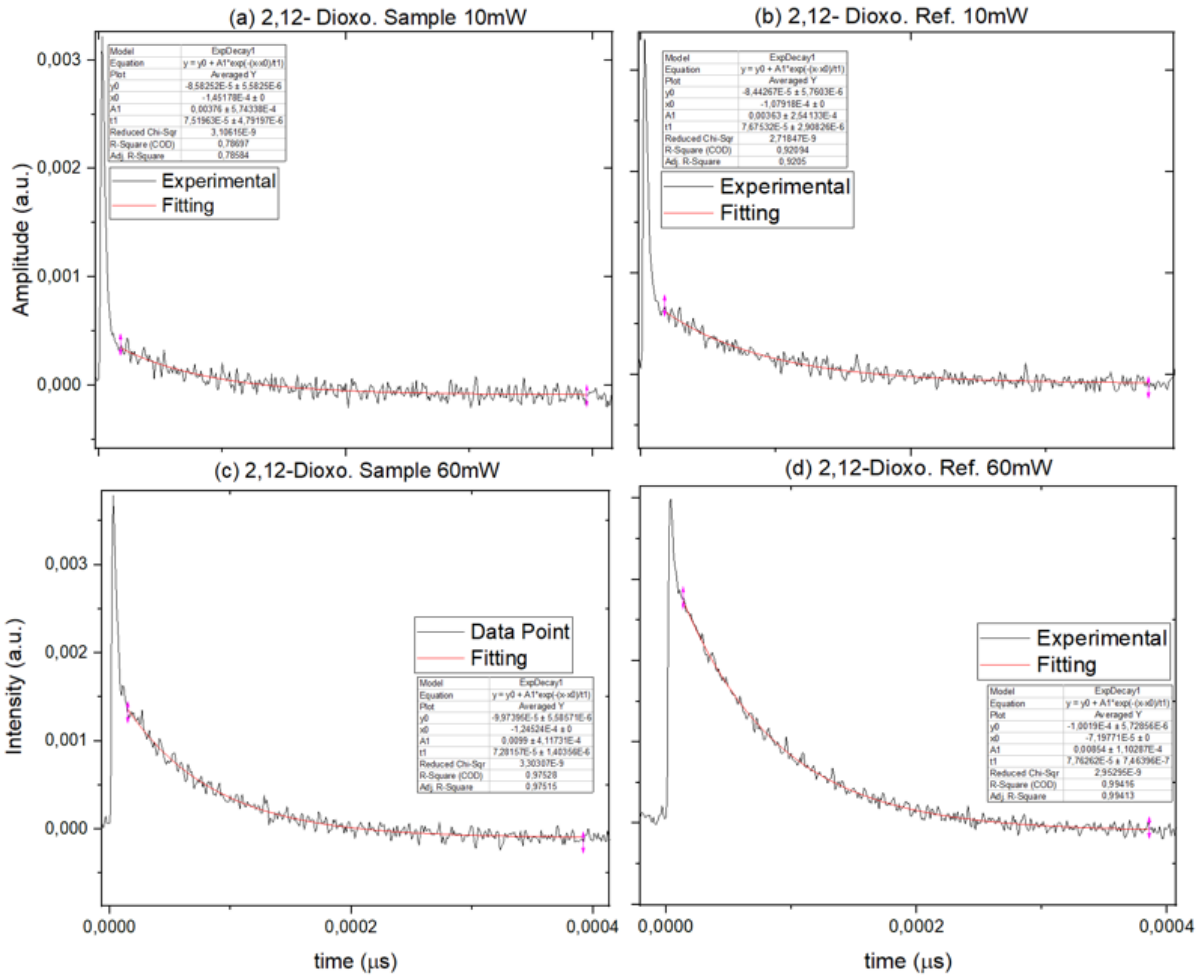
(a) 2,12- Dioxo. Sample 10mW
(b) 2,12- Dioxo. Ref. 10mW
(c) 2,12-Dioxo. Sample 60mW
(d) 2,12-Dioxo. Ref. 60mW
Amplitude (a.u.)
Intensity (a.u.)
time (μs)
Experimental
Fitting
Data Point
Fitting
0,000
0,001
0,002
0,003
0,0000
0,0002
0,0004

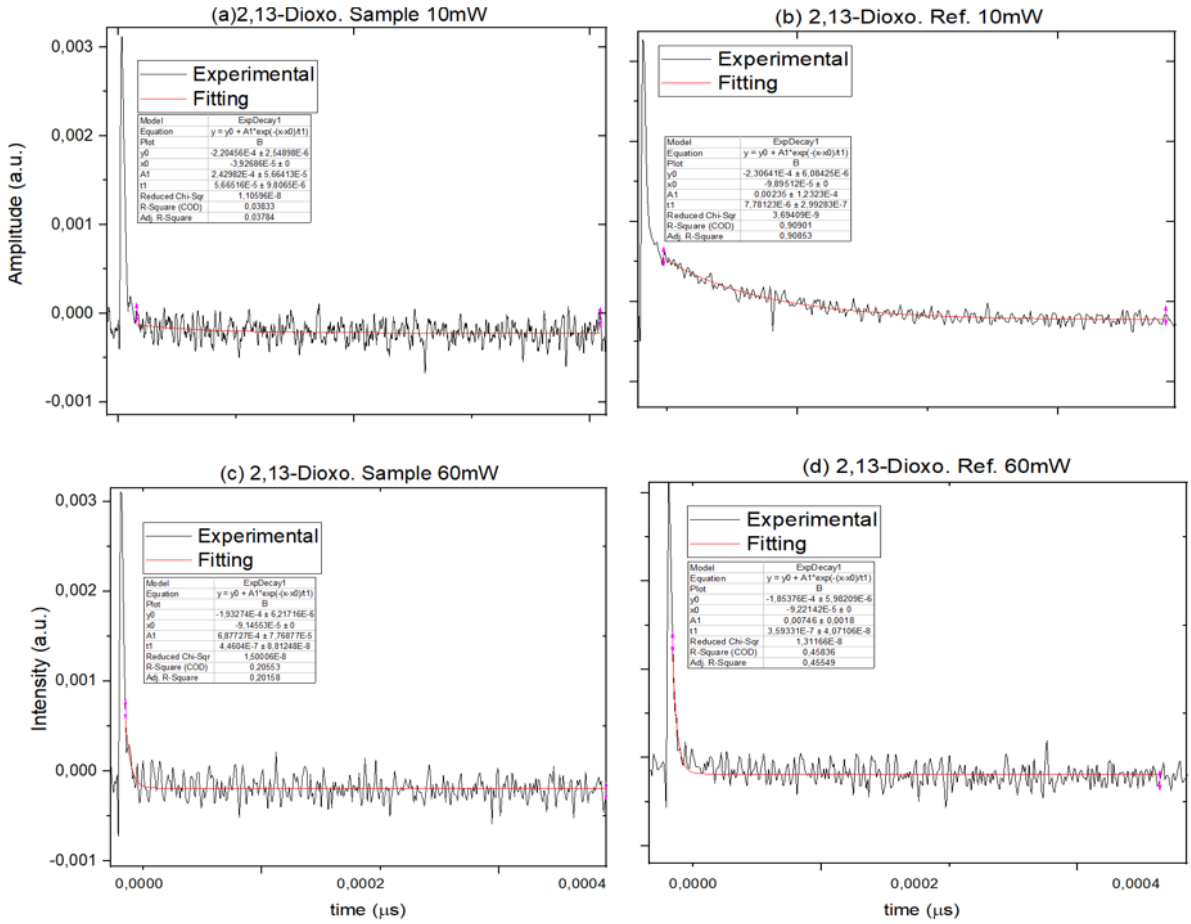
(a)2,13-Dioxo. Sample 10mW
Experimental
Fitting
Model ExpDecay1
Equation y = y0 + A1*exp(-(x-x0)/t1)
Plot B
y0 -2,28456E-4 ± 2,54898E-6
x0 -3,92688E-5 ± 0
A1 2,42982E-4 ± 5,66413E-5
t1 5,66516E-5 ± 9,8065E-6
Reduced Chi-Sqr 1,10596E-8
R-Square (COD) 0,03833
Adj. R-Square 0,03784
(b) 2,13-Dioxo. Ref. 10mW
Experimental
Fitting
Model ExpDecay1
Equation y = y0 + A1*exp(-(x-x0)/t1)
Plot B
y0 -2,30641E-4 ± 6,08425E-6
x0 -9,89512E-5 ± 0
A1 0,00235 ± 1,2323E-4
t1 7,78123E-6 ± 2,99283E-7
Reduced Chi-Sqr 3,69409E-9
R-Square (COD) 0,90901
Adj. R-Square 0,90853
(c) 2,13-Dioxo. Sample 60mW
Experimental
Fitting
Model ExpDecay1
Equation y = y0 + A1*exp(-(x-x0)/t1)
Plot B
y0 -1,93274E-4 ± 6,21716E-6
x0 -9,14553E-5 ± 0
A1 6,87727E-4 ± 7,76877E-5
t1 4,4684E-7 ± 8,81248E-8
Reduced Chi-Sqr 1,50006E-8
R-Square (COD) 0,20553
Adj. R-Square 0,20158
(d) 2,13-Dioxo. Ref. 60mW
Experimental
Fitting
Model ExpDecay1
Equation y = y0 + A1*exp(-(x-x0)/t1)
Plot B
y0 -1,85376E-4 ± 5,98209E-6
x0 -9,22142E-5 ± 0
A1 0,00746 ± 0,0018
t1 3,59331E-7 ± 4,07106E-8
Reduced Chi-Sqr 1,31166E-8
R-Square (COD) 0,45836
Adj. R-Square 0,45549
Amplitude (a.u.)
Intensity (a.u.)
0,003
0,002
0,001
0,000
-0,001
0,0000
0,0002
0,0004
time (μs)